European Association
of Remote Sensing Laboratories

ΠΑΝΕΠΙΣΤΗΜΙΟ ΠΑΤΡΩΝ
UNIVERSITY OF PATRAS

5th international workshop of the EARSeL Special Interest Group "Geological Applications"

Warsaw 19-20 June 2014

Workshop Proceedings

ISBN 978-83-63245-69-6

EDITOR

Konstantinos Nikolakopoulos
Department of Geology
University of Patras

European Association
of Remote Sensing Laboratories

ΠΑΝΕΠΙΣΤΗΜΙΟ ΠΑΤΡΩΝ
UNIVERSITY OF PATRAS

5th international workshop of the EARSeL

Special Interest Group "Geological Applications"

REMOTE SENSING & GEOLOGY

Workshop Proceedings

ISBN 978-83-63245-69-6

http://www.earsel.org/SIG/Geology

EDITOR

Konstantinos Nikolakopoulos
Department of Geology
University of Patras

REMOTE SENSING & GEOLOGY

SYMPOSIUM ORGANISATION

SYMPOSIUM CHAIRMAN

Dr. Konstantinos Nikolakopoulos, Assistant Professor

Scientific Committee:

Manfred Ehlers	University of Osnabrueck
Athanassios Ganas	National Observatory of Athens
Cornelia Gläßer	Martin-Luther-Universität Halle-Wittenberg
Diofantos Hadjimitsis	Cyprus University of Technology
Hermann Kaufmann	Helmholtz Centre Potsdam
Kaan Sevki Kavak	Cumhuriyet University
Ioannis Manakos	CERTH-ITI, Greece
Ulrich Michel	Univ. of Education Heidelberg
Antonios Mouratidis	Aristotle University of Thessaloniki
Konstantinos Nikolakopoulos	University of Patras
Dimitrios Oikonomidis	Aristotle University of Thessaloniki
Marinko Oluic	Scientific Council for Remote Sensing Croatian Academy of Sciences & Arts
Issaak Parcharidis	Harokopio University
Nilanchal Patel	Birla Institute of Technology Mesra
George Skianis	University of Athens
Ana Claudia Teodoro	University of Porto
Emmanuel Vassilakis	University of Athens

Organizing Committee:

Konstantinos Nikolakopoulos	University of Patras
Helga Braun	EARSeL Secretariat
Bogdan Zagajewski	University of Warsaw

EARSeL and the Organizing Committee acknowledge and thank the Sponsors of the Workshop for their support.

Preface

This volume contains the proceedings of the 5th international Workshop of the EARSeL SIG **Geological Applications** titled Remote Sensing and Geology that took place in Warsaw in June 19th and 20th in conjunction with the 34th EARSeL conference.

Scientists from many countries have presented twenty two papers. Fifteen oral presentations and seven poster presentations divided in 7 different topics were carried out. The topics covered were: Geohazards, Geology-Geomorphology, Hyperspectral, Geoarchaeology and Mine Monitoring. The first day of the Workshop was dedicated to the oral and poster presentations while during the second one a tutorial titled "3D Geological Mapping using ERGAS IMAGINE" took place.

The volume of the proceedings follows the general structure of the Workshop topics. For those who could not manage to attend all the sessions, this volume provides a brief overview of the research presented at the workshop in Warsaw.

I would like to thank Mrs. Helga Braun from the EARSeL Secretariat, and especially Prof. Bogdan Zagajewski from the University of Warsaw for their help to the preparation and organization of the Workshop. I would also like to express my sincere thanks Geosystems Hellas SA and Intergraph for providing the evaluation License of ERDAS IMAGINE 2014 that was necessary in order to perform the tutorial.

On behalf of the organizing committee I would like to thank all the participants for their presence in the Workshop, as well as all the authors for their contributions in the present volume. Their cooperation gives us the courage to look forward and plan the next Workshop.

The chairman of the EARSeL SIG “Geological Applications”

Dr. Konstantinos Nikolakopoulos
Assistant Professor
University of Patras
Department of Geology
Sector of Applied Geology & Geophysics
26504 University Campus
Rio Patras, Greece
Tel.: +30-2610-997592,
email: knikolakop@upatras.gr

Contents:

SEMI-AUTOMATED MAPPING OF LANDSLIDE CHANGES IN TAIWAN BY MEANS OF OBJECT-BASED IMAGE ANALYSIS

Daniel Hölbling[1], Barbara Friedl[1] and Clemens Eisank[1]

1. Interfaculty Department of Geoinformatics - Z_GIS, University of Salzburg, Salzburg, Austria; daniel.hoelbling@sbg.ac.at, barbara.friedl@sbg.ac.at, clemens.eisank@sbg.ac.at

ABSTRACT

Earth observation (EO) data are of great value for the detection of landslides after triggering events, especially if they occur in remote and hardly accessible terrain. To fully exploit the potential of the wide range of available remote sensing data, innovative and reliable landslide (change) detection methods are needed. To overcome the limitations of pixel-based methods object-based image analysis (OBIA) has recently been employed for EO-based landslide (change) mapping. The presented approach is developed for a sub-area of the Baichi catchment in northern Taiwan. The focus is on themapping oflandslides and debris flows/sediment transport areascaused by the Typhoons Aere in 2004 and Matsa in 2005. For both events, pre- and post-disaster optical satellite images (SPOT-5 with 2.5 m spatial resolution)were analysed. A digital elevation model (DEM)at 5 m spatial resolution and its derivatives, mainly slope and curvature, were integrated in the analysis to support the semi-automated object-based mapping.The changes were identified by comparing properties of segmentation-derived image objects between pre- and post-event images. To ensure a certain degree of transferability and robustness of the approach changes were mainly detected using relational features such as the Normalized Difference Vegetation Index (NDVI) and the Green Normalized Difference Vegetation Index (GNDVI).

INTRODUCTION

Traditionally, pixel-based approaches are predominantly used for mapping changes based on high resolution (HR) or very high resolution (VHR) satellite imagery (1,2). Yet, pixel-based methods only analyse the change in spectral values for the same pixel locations in multi-temporal images. The salt-and-pepper effect in the resulting (change) maps significantly reduces the ability of pixel-based techniques to adequately depict changes of natural phenomena such as landslides. To overcome these limitations object-based image analysis (OBIA) has recently been employed for EO-based change mapping (1). Apart from spectral characteristics, OBIA allows the utilisation of spatial, contextual and morphological properties. Due to the reduced relevance of spectral information, atmospheric and radiometric correction of images is less important for object-based change detection. However, only few studies have shown the potential of OBIA for landslide change mapping.A semi-automatic object-oriented change detection approach using VHRoptical satellite imagery for landslide rapid mapping was developed by Lu et al. (3).Anders et al. (4) used LiDAR digital terrain models for geomorphological change analysis. Martha et al. (5) suggested an approach based on brightness changes in pre- and post-event panchromatic images for the creation of historical landslide inventories.Park and Chi (6) used an object-based change detection approach to locate landslide-prone areas.

The main objective of this study is to semi-automatically detect and classify typhoon-induced landslide changes based on pre- and post-event satellite images.Mass movements were classified into “landslides” and “debris flows/sediment transport areas” to allow for theidentification of class-specific changes.

METHODS

Study area

The presented approach was developed for a sub-area of the Baichi catchment, which is located in the Shihmen Reservoir watershed in northern Taiwan (Figure 1). The island of Taiwan is situated in the tropical and sub-tropical climate zones. During summer and autumn, especially from July to October, Taiwan is regularly affected by typhoons. The heavy rainfalls associated with these tropical storms often cause numerous landslides and debris flows, leading to fatalities and severe damages of infrastructure. The study site covers an area of approximately 16 km² and is characterized by mountainous terrain with steep slopes that are highly susceptible to mass movements. The focus of this study is on the semi-automated (change) mapping of landslides and debris flows/sediment transport areas caused by the Typhoons Aere (August 23-26, 2004) and Matsa (August 3-6, 2005), respectively.Manual interpretation of post-event orthophotos showed that Typhoon Aere caused 703 landslides in the Shihmen Reservoir watershed (7), whereof 421 landslides occurred in the Baichi catchment(8,9).Typhoon Aere brought more than 1,600 mm and Typhoon Matsa over 1,200 mm of accumulated rainfall to the Shihmen Reservoir watershed, whereby especially the Baichi and Yufeng catchments were heavily affected (10). Statistically, such a heavy rainfall event occurs in Baichi only once every 100 years (10).

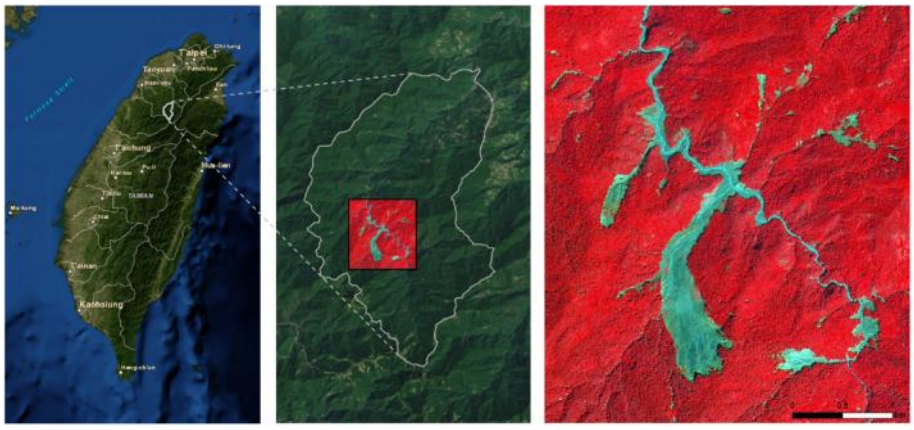

Figure 1: Study area: overview of Taiwan with the Baichi catchment (grey polygon; left); Baichi catchment and location of the study site(centre); SPOT-5 image (acquisition date: 09/09/2005; after Typhoon Matsa) showing the study area (right).

Data

Pre- and post-event SPOT-5 images with three spectral bands (green, red, near infrared) and a spatial resolution of 2.5 m were used for the mapping of landslides and landslide changes. The SPOT-5 images represent the status quo before and after the Typhoons Aere and Matsa. Additionally, a digital elevation model (DEM) with 5 m spatial resolution and its derivativeswere integrated in the analysis to support the semi-automated (change) mapping of landslides and debris flows/sediment transport areas (see Table 1).

Table 1: Remote sensing data for the sub-area of the Baichi catchment.

Data	Description	Spatial resolution	Acquisition data
SPOT-5	Pre-event image: Typhoon Aere	2.5 m	10/02/2004
	Post-event image: Typhoon Aere	2.5 m	02/11/2004
	Pre-event image: Typhoon Matsa	2.5 m	16/03/2005
	Post-event image: Typhoon Matsa	2.5 m	09/09/2005
DEM	Pre-event data;	5 m	Derived from orthophotos

	Including DEM derivatives: slope, curvature, plan curvature, profile curvature		taken in 2002 and 2003

Object-based classification on post-event optical data

The semi-automated object-based classification of landslides and debris flows/sediment transport areas was based on the post-event SPOT-5 image from 2005 and the 5 m DEM including its derivatives. Image analysis was conducted in eCognition (Trimble) software. First, additional layers (brightness, Normalized Difference Vegetation Index - NDVI, Green Normalized Difference Vegetation Index - GNDVI) were calculated. The selection of an appropriate scale parameter for multiresolution segmentation was supported by using the Estimation of Scale Parameter 2 (ESP 2) tool. ESP 2 identifies statistically relevant image object levels for a set of input layers(11).A scale parameter of 32 was finally selected for multiresolution segmentation of SPOT-5 bands, the NDVI and brightness layers. Subsequently,the NDVI and brightness were used for the recognition of areas affected by mass movements. The absence of vegetation,and thus, the presence of bare ground wereassumed to be an evidence for the occurrence of mass movements.As debris flows/sediment transport areas showed non-uniform spectral features, they were mainly differentiated from landslidesbymorphological characteristics.Sincedebris flows/sediment transporttake placemost likely along stream channels, anindependent segmentation of plan curvature and slope was performed.Objects with low curvature values were then classified as concave terrain. Additional object features(e.g. slope, relative border to neighbouring objects) were used to enhance the extraction of stream channels.Results were synchronized with the potential mass movement areas previously classified, and addressed as debris flows/sediment transport areas from now on.Noteworthy, this class includes also the larger river beds where the downstream transportation of debris and sedimentsoccurs. The remaining areas affected by mass movements were treated as landslides. The two classes were further refined by using spatial (e.g. area, shape) and contextual parameters (e.g. relative border to neighbouring objects) to eliminatefalse positives with spectral properties similar to mass movement areas (e.g. paths, harvested agricultural fields, cleared bamboo forest). The boundaries of the classified image objects werefinally smoothed by growing and shrinking operations.

The described approach was transferred to the post-event SPOT-5 image from 2004, which shows radiometric differences compared to the one from 2005. The vegetation appears to be darker and more shadows are present. Nevertheless, the developed ruleset could be transferred with only minor adaptations. The obtained classification results served as input for the class-specific object-based change detection.

Class-specific change detection

The class-specific object-based change detection was first accomplishedfor theTyphoon Matsa event (2005) and then transferred to the images available for the Typhoon Aere (2004). The typhoon-triggered landslides and debris flows/sediment transport areas were identified by comparing the properties of segmentation-derived image objects between the respective pre- and post-event images. The loss of vegetation served as proxy for the occurrence of mass movements. Vegetation loss wasidentified by a negative change of the NDVI and the GNDVI. As the quality and radiometric characteristics of the pre- and post-event images differ (mainly because of different acquisition dates during the year), normalization factors were calculated to normalize thevegetation indices across the two images.This was done by dividing the value of the post-eventNDVI and GNDVI, respectively, by the value of the corresponding pre-event index. As next step, a joint multiresolution segmentation on both images from 2005 was carried out using the bands of the SPOT-5 imagesand the NDVI layers. Again, the selection of an appropriate scale parameter, in this case 31, was supported by the statistical evaluation with the ESP 2 tool. Each of the resulting objects was then investigated in respect of its transformation between the two points in time. By multiplying theoriginalpre-event NDVI and GNDVIwith the corresponding normalization factor theywere adapted to the post-event indices to enable an objective comparison of values.Next, the

post-event NDVI and GNDVI were subtracted from the corresponding adapted pre-event index. If the resulting value was higher than adefined threshold,the objects were classified as affected by a change. The introduction of such a threshold was necessary to prevent the classification of objects which showed only minor value changes. A second condition was applied to detect only those objects with a relatively low NDVI value in the post-event image. As a result, areas which had been affected by a change in vegetation, but which were still vegetated, could be excluded. Finally, the objects affected by change were synchronized with the prior established classification of landslides and debris flow/sediment transport areas to assess class-specific changes.

RESULTS

Landslides and debris flows/sediment transport areas could be accurately classified and changes were efficiently detected. Taiwanese landslide experts confirmed the validity of the results during recent workshops and personnel discussions. Figure 2 shows the results of the semi-automated object-based classification of landslides and debris flows/sediment transport areas for the post-event images from 2004 and 2005.

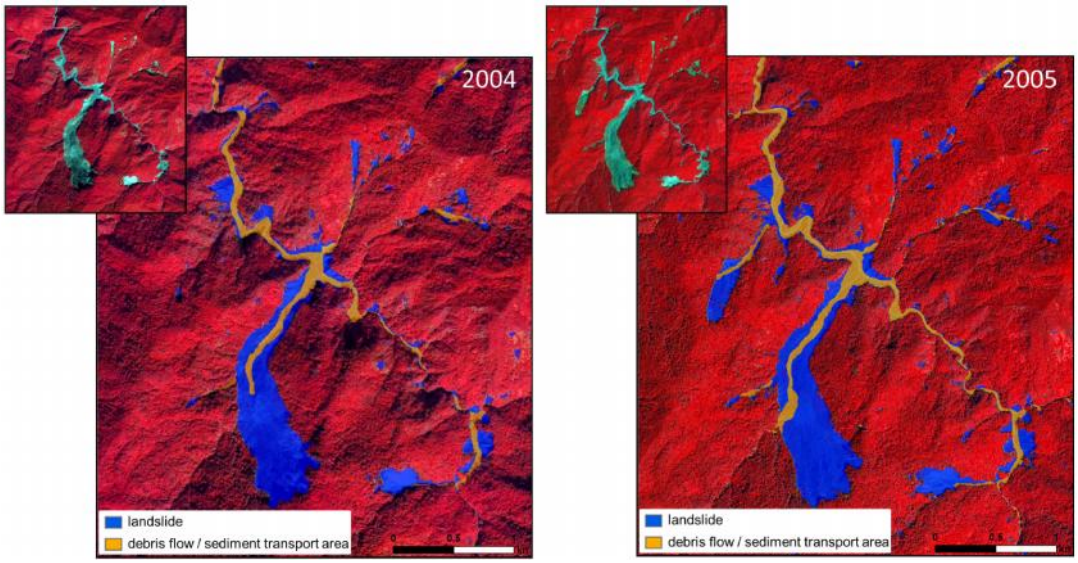

Figure 2: Classification result showing the detected landslides and debris flows/sediment transport areas after Typhoon Aere (2004; left) and after Typhoon Matsa (2005; right).

For quantitatively assessing the accuracy, the classification results were compared to a landslide inventory that was produced by local landslide experts through manual interpretation of orthophotos (see Table 2).As the reference data set does not include debris flows or other sediment transport areas, only the accuracy of the detected landslides was assessed.In general, the semi-automated classification overestimates the reference; the deviationbetween the semi-automatically classified landslides and the reference accounts to approximately 20 % for 2004 and about 24 % for 2005.

Table 2: Classification results (in hectare) for the post-event images from 2004 and 2005 and producer's and user's accuracy for the class "landslide".

	Class	*Classification (in ha)*	*Reference (in ha)*	*Correctly classified areas(in ha)*	*Producer's accuracy (in %)*	*User's accuracy (in %)*
Area (2004)	Landslide	96.42	80.08	68.04	84.97	70.57
	Debris flows/ sediment	34.67	n/a	n/a	n/a	n/a

	transport area					
Matsa (2005)	Landslide	112.57	90.6	76.28	84.19	67.76
	Debris flows/ sediment transport area	49.01	n/a	n/a	n/a	n/a

The results of the class-specific change detection (see Figure 3) revealed thatapproximately 58.5 % of areas affected by landslides and 36.5 % of the debris flows/sediment transport areas detected in the post-event image of 2004 were caused by Typhoon Aere. About 10 % of areas affected by landslidesand 5.5 % of the debris flows/sediment transport areas detected in the post-event image of 2005 were caused by Typhoon Matsa.

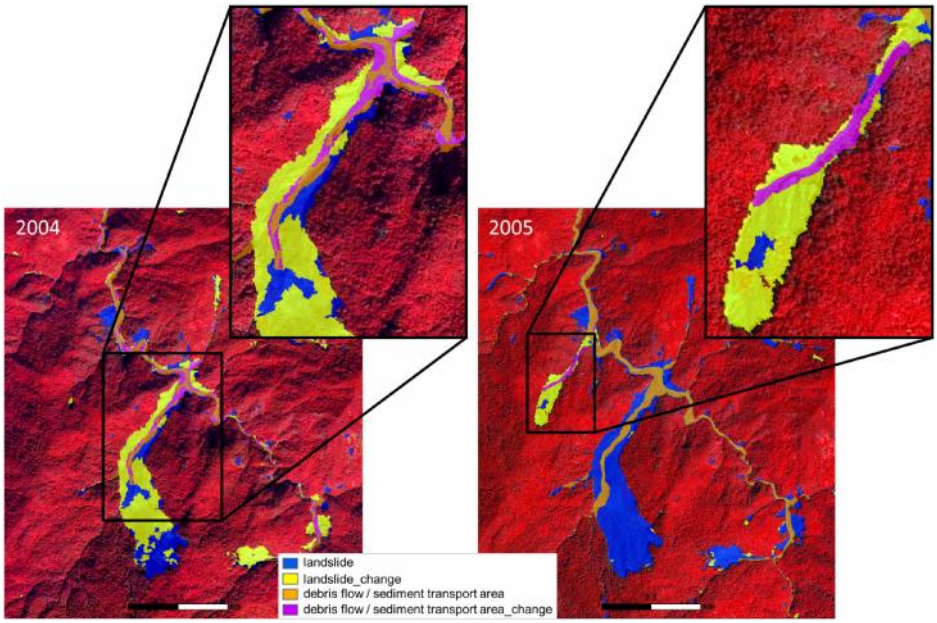

Figure 3: Result of the class-specific object-based change detection for 2004 (left) and 2005 (right).New landslides are displayed in yellow colour, new debris flows/sediment transport areas in purple.

CONCLUSIONS

The presented method for mapping landslide changes based on remote sensing data aims at a high level of automation and transferability. Changes were mainly recognized based on the relative difference of spectral indices (NDVI, GNDVI). The use of absolute spectral thresholds was minimized.However, further research is needed, especially to improve the differentiation of landslides and debris flows/sediment transport areas. Although debris flows pose a severe threat in Taiwan - they often cause more serious damages than landslides - a comprehensive data base comprising debris flows is still missing. The reason for this may lie in the fact that it is hardly possible to find generally valid properties to describe this mass movement type. For tackling this problem we developed a method to classify debris flows and otherareas where sediment transport happens, which mainly relies on morphological features. To further improve the objectivity, transferability and robustness of the method the common knowledge of a numberof expertscould be transformed into computer-based rules and integrated in the analysis. Such aknowledge-based landslide mapping system was recently proposed by Eisank et al. (12).

The detected landslides in the post-event images from 2004 and 2005 were validated by comparing them to manually derivedlandslide maps. Such data setsare often the only reference available, but cannot constitute a completely true reference (13) as their generation depends on

the skills of the interpreter, the underlying data, on which scale the reference was obtained and on the purpose of the manual mapping.

Semi-automated object-based change detectionapproaches can, for example, be used for the regular update of landslide inventory maps. Furthermore, areas potentially susceptible to landslides may be identified by retrospective analyses of past landslide events. Results might be of interest for local stakeholders and decision makers, as information on the location and spatial distribution of both new and re-activated landslides can be valuable for disaster prevention and risk management.

ACKNOWLEDGEMENTS

This research is supported by the Austrian Science Fundthrough the project “'iSLIDE - Integrated Semi-Automated Landslide Delineation, Classification and Evaluation” (FWF-P25446-N29). The authors would like to thank Antonia Osberger for fruitful discussions and valuable comments as well as Yi-Chin Chen and Kang-Tsung Chang for providing the reference data.

REFERENCES

1 Chen G, G J Hay, L Carvalho & M A Wulder, 2012. Object-based change detection. International Journal of Remote Sensing, 33: 4434-4457.

2 Hussain M, D Chen, A Cheng, H Wei & D Stanley, 2013. Change detection from remotely sensed images: From pixel-based to object-based approaches. ISPRS Journal of Photogrammetry and Remote Sensing, 80: 91-106.

3 Lu P, A Stumpf, N Kerle & N Casagli, 2011. Object-oriented change detection for landslide rapid mapping. IEEE Geoscience and Remote Sensing Letters, 8: 701-705.

4 Anders N, A Seijmonsbergen & W. Bouten, 2013. Geomorphological Change Detection Using Object-Based Feature Extraction From Multi-Temporal LiDAR Data. IEEE Geoscience and Remote Sensing Letters, 10: 1587-1591.

5 Martha T R, N Kerle, C J van Westen, V Jetten & K V Kumar, 2012. Object-oriented analysis of multi-temporal panchromatic images for creation of historical landslide inventories. ISPRS Journal of Photogrammetry and Remote Sensing, 67: 105-119.

6 Park N W & K H Chi, 2008. Quantitative assessment of landslide susceptibility using high-resolution remote sensing data and a generalized additive model. International Journal of Remote Sensing, 29: 247-264.

7 Chang K-T, S H Chiang & F Lei, 2008. Analysing the Relationship Between Typhoon-Triggered Landslides and Critical Rainfall Conditions. Earth Surface Processes and Landforms, 33: 1261-1271.

8 Chang K-T & S H Chiang, 2009. An integrated model for predicting rainfall-induced landslides. Geomorphology, 105: 366-373.

9 Chiang S H & K-T Chang, 2009. Application of radar data to modeling rainfall-induced landslides. Geomorphology, 103: 299-309.

10 Chen C Y, L K Chen, F C Yu, S C Lin, Y C Lin, C L Lee & Y T Wang, 2010. Landslides affecting sedimentary characteristics of reservoir basin. Environmental Earth Sciences, 59: 1693-1702.

11 Drăguţ L, O Csillik, C Eisank & D Tiede, 2014. Automated parameterisation for multi-scale image segmentation on multiple layers. ISPRS Journal of Photogrammetry and Remote Sensing, 88: 119-127.

12 Eisank C, D Hölbling, B Friedl, Y-C Chen & K-T Chang, 2014. Expert knowledge for object-based landslide mapping in Taiwan. South-Eastern European Journal of Earth Observation and Geomatics, Special Thematic Issue: GEOBIA 2014 - Advancements, trends and challenges, 5th Geographic Object-Based Image Analysis Conference, 3: 347-350.

13 Hölbling D, P Füreder, F Antolini, F Cigna, N Casagli & S Lang, 2012. A Semi-Automated Object-Based Approach for Landslide Detection Validated by Persistent Scatterer Interferometry Measures and Landslide Inventories. Remote Sensing, 4: 1310-1336.

TERRAIN MOTION OF SELECTED ABANDONED HARD COAL MINES IN THE NORTH – EASTERN PART OF THE UPPER SILESIAN COAL BASIN (SOUTHERN POLAND) IN VIEW OF SAR INTERFEROMETRIC DATA

Marek Graniczny[1], Zbigniew Kowalski[1], Maria Przyłucka[1], Albin Zdanowski[1], Karsten Zimmermann[2]

1. Polish Geological Institute – National Research Institute, Warsaw, Poland, marek.graniczny@pgi.gov.pl, zbigniew.kowalski@pgi.gov.pl, maria.przylucka@pgi.gov.pl, albin.zdanowski@pgi.gov.pl
2. DMT GmbH & Co. KG, Essen, Germany, Karsten.Zimmermann@dmt.de

ABSTRACT

Application of PSInSAR satellite interferometric method for observations of ground deformations in the north-eastern part of the USCB is presented in this paper. As test sites four hard coal mines located in Upper Silesian Coal Basin were selected. Water inflow in the mine may also cause different phenomena like surface instability (subsidence, uplift), induced seismicity and chemical degradation of the water. The paper presents the relationship between dewatering process in closed mines and surface changes indicated on the satellite interferometric data. The first "Terrafirma Sosnowiec" PSInSAR dataset from 1992 to 2003 shows active mines and indicates values of ground motions from -9.4 to +2.1 mm per year. It is estimated that 97 % of PS points show subsidence. On the other hand second PSInSAR database (Terrafirma "Bedzin") from 2003 to 2010, in the period of abandoned mines shows values from - 7.6 to +9.8. Almost 97 % of PS points indicating uplift of the terrain. In common opinion after period of 5 years from mine closure the area is considered as safe. The obtained results show that it is not true, and the ground motions still exist at these area. This may lead to generating potential hazard to people, buildings and infrastructure.

INTRODUCTION

The Upper Silesian Coal Basin (USCB) is located in the southern Poland and in the region of Ostrava-Karvina in the Czech Republic. It covers an area of 7,250 km^2. This is the major coal basin in Poland, and also one of the largest in Europe.

Many centuries of mining activity in the Upper Silesia has caused irreversible changes in the earth's surface over large areas. Extraction of minerals and their processing is accompanied by the transformation of the terrain as:

- Subsidence (basins, bowls and depressions).
- Flooding and inundations.
- Overburden drainage of exploiting deposits.
- Seismic shocks.
- Storage of waste rocks at heaps.

In the last years the method of coal mining is mainly longwall with caving. It is estimated that in some areas of the USCB – central, north and north – west, coal seems with a total thickness about 50 – 60 m. were exploited. The subsidence on these area locally exceed 30 m and usually reach values from a dozen to 20 m. On the other parts of USCB, where exploitation is carried out from at least 25 years, values of subsidence are ranging from 5 to 10 m.

Presently in northern and north – eastern part of USCB, despite the operation of underground dewatering systems the aquifers in abandoned mines have steady tendency to rise up. As the result, in areas where until recently subsidence occur in the surface, the terrain uplift is observed. This phenomena could be excellently monitored using SAR interferometry technology. Examples of ground motion changes above abandoned Coal Mines ”Grodziec”, “Paryż”, “Saturn” and “Sosnowiec” were presented in this paper.

DESCRIPTION OF THE INTERFEROMETRIC TECHNIQUES AND DATA

Synthetic Aperture Radar Interferometry (InSAR) from satellite radar images has revolutionized the field of ground deformation research since its first geological applications about a two decades ago. This past 20 years allowed for significant development of the processing techniques as well as for increased use of InSAR data to study displacement associated with, as an example, active faults, volcanoes, landslides, aquifers, oil fields, glaciers or mining, at a spatial resolution of less than 100 m and centimetre precision. The method is based on the principle of wave interference. As a result of a combination of two radar images of the same area, acquired before and after the occurrence of ground displacement, an interferogram is created. Changes in ground surface are visible in the form of the interferometric fringes. InSAR is particularly sensitive to vertical deformation (1). To improve the ability to determine millimetre-level displacement, more than 10 years ago a new approach, Permanent Scatterer SAR Interferometry (PSInSAR) has been introduced (2)(3). The processing is made on a basis of more than 15 SAR images, acquired for the same area in long period . As a result of the processing of the stack, set of thousands of permanent scatterers (PS) is identified. PS are objects, which are characterized by stable reflection of the radar beam. For each point displacement time series and velocity of movement for whole period of acquisition can be calculated (4). PSInSAR allows to identify motion at a level of 1 mm per year (1).

InSAR has been world-wide successfully used for monitoring mining-inducted ground movements as well as movements indirectly related to the activity or closure of the mine. The possibility to study deformation over mining areas have been widely presented for example by (5). Also, Upper Silesia Coal Basin in Poland has been subject of many studies conducted by several research institutions in Poland, examples can be found in (6),(7),(8). For this study several stacks of ERS and ENVISAT C-band satellite data from 1992 to 2010 were analyzed to investigate terrain motion over four (“Grodziec”, “Paryz”, Sosnowiec” and “Saturn”) abandoned hard coal mines.

GEOLOGICAL SETTING AND HYDROGEOLOGICAL CHARACTERISTICS

The region of the Upper Silesian Coal Basin can be divided into two hydrogeological subregions: the north-eastern subregion (I) and the south-western subregion (II) (Fig. 1). Subregion I is described as a hydrogeologically "open" area. Quaternary, Jurassic and Triassic aquifer formations are present in the overburden. These formations are hydraulically connected to the Carboniferous formations. Sandstones of high porosity and permeability are present in the Carboniferous profile. The research area comprising the abandoned mines of: Grodziec, Paryż, Saturn and Sosnowiec is located in the north-eastern part of the USCB, being a part of the uncovered subregion I. Three lithostratigraphic series are present in the profile of Carboniferous strata: the Upper Silesian Sandstone Series, the Paralic Series and the Mudstone series. The Carboniferous outcrops are located within the area of the “Paryż” and “Grodziec” mines, with the Carboniferous being covered by not very thick Triassic or Quaternary deposits in the remaining areas. The research area is characterised by complex tectonics and it is intersected by numerous faults. The main fault is the Będzin-Wojkowice fault extending NWN-ESE with a slip of 200-250 m towards the SW. Another characteristic fault is the meridional Grodziec fault with a 260 m slip in the western direction.

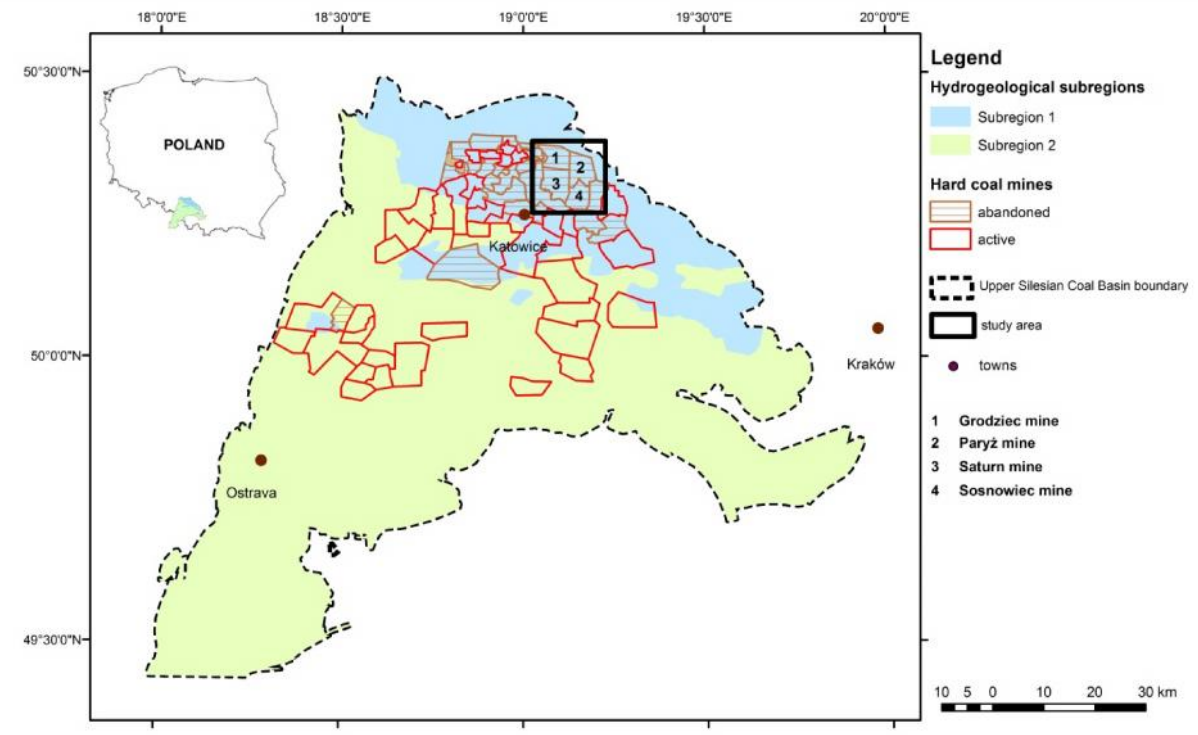

Fig. 1 Simplified hydrogeological map of the Upper Silesian Coal Basin

MINE FLOODING WITHIN THE RESEARCH AREA

The restructuring process of Polish hard coal mining began in 1989. About 70 coal mines were functioning in the Upper Silesian Coal Basin near the end of the 1980s, with just 30 of them left today. Among others, the following unprofitable mines of the Dąbrowa Basin have been liquidated: "Paryż" (December of 1996), "Saturn" (December of 1996), "Sosnowiec" (December of 1998) and "Grodziec" (June of 2000). Mine shutdown processes are associated with water risks related to flooding of mine workings. Submersible or stationary dewatering systems are used in order to minimise these risks. A controlled mine workings flooding process was conducted for the regions of the above mentioned mines. According to the data from monitoring for the period between 2001 and 2008, underground water reservoirs were created inside the flooded mines, their respective volumes being 10.1, 8.1, 7.4 and 4.5 mln m^3 (9). Continuous dewatering was conducted in the Paryż, Saturn and Sosnowiec mines, with the natural inflow of water into the mine workings and goafs being controlled simultaneously. The stationary dewatering system was deactivated in the Grodziec mine between October of 2000 and December of 2005, implementing the mine flooding process. Having reached the water table level of 57 m a.s.l. the submersible pumps were activated, maintaining that level till February of 2007. After that period water damming process was initiated again in the mining workings and goafs, reaching the level of 88 m a.s.l. in May of 2008.

RADAR INTERFEROMETRY DATA AND RESULTS

Three sets of radar data were available for the research area:

- 54 ERS satellite images, C band, descending mode, 1992 – 2003 period;

- 31 Envisat satellite images, C band, track 222, descending mode, 2003 – 2010 period;
- 26 Envisat satellite images, C band, track 484, descending mode, 2002 – 2010 period.

The maximum displacements between 1992 and 2010 ranged from – 19.39 to +12.15 mm per year. This data indicates that the land uplift process began during a period of several years after the liquidation of mines near the end of the 1990s and the initiation of the flooding of mine headings. Particularly interesting information is presented in the data from the flooding of the Grodziec mine between 2000 and 2009. An underground reservoir was created during that time with the volume of 11.6 mln m^3 and the water table level raised by as many as 279 metres. The analysed interferometric data from the time series (TS) for this period indicate a surface uplift process. In this case the magnitude of uplift amount to about a dozen mm/year. There is a direct correlation between flooding of mine workings in abandoned mines and the land surface uplifting process. Discontinuation or temporary suspension of dewatering of an abandoned mine leads to shrinkage of the depression cone, creation of massive underground reservoirs and reconstruction of previous groundwater regime. The oldest data originating from the ERS satellite for the 1992-2003 period proves that minor land subsidence is a predominant process taking place within the research area (Fig. 2).

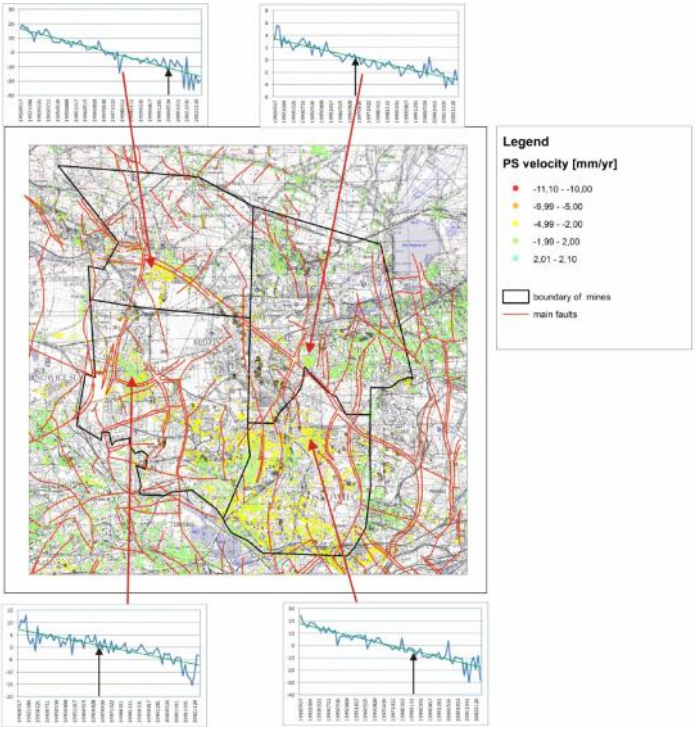

Fig. 2 ERS (1992-2003) Permanent Scatterer velocity and Time Series of selected points within abandoned mines (black arrows – the date of liquidation of mine)

The greatest subsidence of about a dozen millimetres per year occurs within the area of the Grodziec and Sosnowiec mines, which were closed in June of 2000 and December of 1998 respectively. Within the mining areas of the Paryż and Saturn mines shut down in December of 1996 the predominance of PS points which may be considered stable is visible. The liquidation date of each mine has been marked by a vertical black arrow on the time series plots for individual mining areas.

A different picture is presented by the data from the Envisat satellite: 2002-2010 (track 494)- Fig. 3. During this time period an uplifting process is predominant (Fig. and Fig.). The highest values of uplift for the PS points exceed 10 mm per year. The main causes of vertical upward movement of points are flooding of mine workings and discontinuation or temporary suspension of dewatering of liquidated mines. As an effect, reconstruction of previously drained aquifers takes place along with an increase in pressure in the aquifer and with creation of huge groundwater reservoirs. The volume of water in flooded goafs exceeds about a dozen million m^3. The data from radar interferometry indicates that the areas of highest uplift are located in the proximity of fault zones. The fissures in overburden layers, especially the Triassic limestones contribute to the change in groundwater circulation regime. The presence of greatest displacements in the area surrounding the Będzin-Wojkowice and Grodziec faults probably evidences the process of unsealing the fault zones.

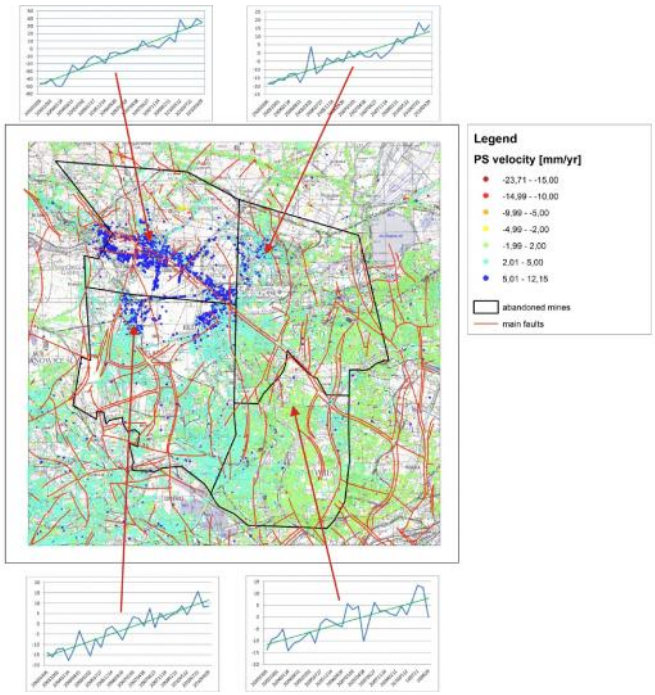

Fig. 3 Envisat – track 494 (2002-2010) Permanent Scatterer velocity and Time Series of selected points within abandoned mines.

CONCLUSIONS

During mine liquidation the presence of water in the rock mass, resulting from the reconstruction of hydrogeological conditions in a past mining area dewatered during extraction, and the pressure of groundwater associated with it may cause slight uplift of the surface, especially in the vicinity of fault zones. In turn, the reascension of water table after discontinuation of mine dewatering causes land uplift. Based on the observation of the data from radar interferometry it can be concluded that ascending movements are usually small and in reality amount to approximately 10 % of the value of subsidence from the period of mine activity. The existing regulations demand that the area of a liquidated mine be monitored for 5 years after the extraction is over. Based on the radar interferometry data it appears that land movements within a past mining area are maintained even for over 10

years after mine shutdown. From the experience of the authors it can be concluded that the application of radar imagery and radar interferometry technique provides a more detailed picture of surface movements than geodesic methods. It is particularly important considering the fact that no continuous geodetic monitoring takes place within the areas of abandoned mines.

REFERENCES

1 Ferretti A., Novali F., Bürgmann R., Hilley G., Prati C., (2004). InSAR Permanent Scatterer Analysis Reveals Ups and Downs in San Francisco Bay Area, Eos, Vol. 85, No. 34, pp. 317, 324.

2 Ferretti A., Prati C., Rocca F., (2000). Nonlinear subsidence rate estimation using permanent scatteres in differential SAR interferometry. IEEE Transactions on Geoscience and Remote Sensing 38, pp.2202-2212.

3 Ferreti A., Prati C., Rocca F., (2001). Permanent Scatterers in SAR Interferometry, IEEE Transactions on Geoscience and Remote Sensing, vol. 39: 8-20.

4 Colesanti C., Ferretti A., Novali F., Prati C., and Rocca F.,(2003). SAR monitoring of progressive and seasonal ground deformation using the permanent scatterers technique, IEEE Trans. Geosci. Remote Sens.,4 (7), pp.1685–1701.

5 Benecke N., Bateson L., Browitt C., Declercq P., Graniczny M., Marsh S., Zimmermann K. (2012). Perspectives concerning Satellite EO and geohazard risk management: the way forward - Community paper concerning inactive mines hazards, in book: Ph. Bally (Ed.) (2012), The InternatIonal Forum on Satellite EO and Geohazardas, Forum on Satellite EO and Geohazards, (2012), Santorini Greece., doi:10.5270/esa-geo-hzrd-2012, pp.81-90.

6 Perski Z., Jura D., 1999, ERS SAR interferometry for land subsidence detection in coal mining areas, Erth observation quartarly, vol. 63, pp. 25-29.

7 Graniczny M., (2009). Sosnowiec, Poland. [In]: The Terrafirma Atlas – The terrain-motion information service for Europe (ed. Capes R., Marsh S.), GMES – ESA, June 2009. TerraFirma project, ESA publication, p. 34.

8 Graniczny M., Kowalski Z., Leśniak A., Czarnogórska M., Piątkowska A., (2007). Analysis of the PSI data from the Upper Silesia – SW Poland. The International Geohazard Week 5–9 November 2007 ESA-ESRIN Frascati Rome, Italy. The International Forum on Satellite EO and Geohazards: 17

9 Czapnik A., Janson E., Jasińska A., (2009a). Selected problems with monitoring in anandoned hard coal mines in The Upper Silesian Coal Basin – Biuletyn Państwowego Instytutu Geologicznego. Hydrogeologia, 436, pp. 55-60

SEISMIC PRECURSORS AND CLIMATE FLUCTUATIONS ASSESSMENT THROUGH TIME SERIES GEOSPATIAL AND IN-SITU MONITORING DATA

Maria Zoran, Roxana Savastru, Dan Savastru,

National Institute of R&D for Optoelectronics, Bucharest -Magurele, Romania, maria@dnt.ro

ABSTRACT

Recent investigations suggest that climate change tends to exacerbate geo-disasters like as earthquake events. Earthquake science has entered a new era with the development of space-based technologies to measure surface geophysical parameters and deformation at the boundaries of tectonic plates and large faults. Different criteria can be used to select the remote sensed earthquake pre-signals for which there is an evidence for anomalies in the geophysical observables. Rock microfracturing in the Earth's crust preceding a seismic rupture may cause local surface deformation fields, rock dislocations, charged particle generation and motion, electrical conductivity changes, gas emission, fluid diffusion, electrokinetic, piezomagnetic and piezoelectric effects as well as climate fluctuations. Space-time anomalies of Earth's emitted radiation (thermal infrared radiation linked to air and land surface temperature variations recorded from satellite months to weeks before the occurrence of earthquakes, radon in underground water, soil and near the ground air, etc.), ionospheric and electromagnetic anomalies are considered as earthquake precursors. At land surface, energy fluxes interact instantaneously with each other in accordance with the prevailing meteorological conditions and the specific thermal and radiative characteristics of the soil surface. This paper aims to investigate seismic pre-signals variation (air and land surface temperature, and outgoing long-wave radiation) for some earthquakes recorded in Vranceaseismic active area in Romania. Based on local tectonic geology, hydrology and meteorology, such findings support lithosphere–ionosphere coupling theory.

INTRODUCTION

The geotectonic active areas like is Vrancea seismic zone in Romania are accompanied with crustal deformations and energy transfer, which must change the state of thermal radiation on the land surface. Thus it is possible to infer present-day geotectonic activities based on variations of the thermal radiation state on the land surface or near the ground derived from the satellite data. Earthquake preparation is a transient dynamic process which can be monitored in real time from geospatial data validated with in-situ monitoring. Due to new advanced satellite multispectral sensors and high temporal and spatial resolutions of satellite missions, their data can exhibit processes of spatio-temporal variation of geophysical parameters of seismic active regions.

Several studies performed in the last years suggested the existence of anomalous space-time transients, in the thermal infrared (TIR) radiation emitted by the Earth, possibly related to earthquake preparatory phenomena. Among different theories about their origin, the abrupt increase in radon gas (Rn^{222}), greenhouse gases (CO_2, CH_4, NO_2 etc) emission rates has been also proposed to explain the appearance of anomalous TIR precursory signals in some relation with the place and the time of earthquake occurrence in geotectonic active areas. Geospatial data, coupled with ground-based observations where available, enable scientists to survey pre-earthquake signals in areas of strong tectonic activity.

Natural radioactivity (in particular, radon Rn-222) is considered to be a possible trigger for atmospheric increased ionization and electrical conditions anomalies in the lower atmosphere (atmospheric conductivity and the electric field) and upper atmosphere (ionospheric TEC –Total Electron Content anomalies).

Different criteria can be used to select the remote sensed earthquake precursors for which there is an evidence of geophysical parameters anomalies. Rock microfracturing in the Earth's crust preceding a seismic rupture may cause local surface deformation fields, rock dislocations, charged particle generation and motion, electrical conductivity changes, gas emission, fluid diffusion, electrokinetic, piezomagnetic and piezoelectric effects as well as climate fluctuations. Space-time anomalies of Earth's emitted radiation (thermal infrared radiation linked to air and land surface temperature variations recorded from satellite months to weeks before the occurrence of earthquakes, radon in underground water, soil and near the ground air, etc.), ionospheric and electromagnetic anomalies are considered as earthquake precursors.The mosaic pattern of the strain field in the epicentral zones creates a specific obstacle to the detection of precursory events and determination of the spatial scale of the earthquake preparation zone. Obviously, the size of the zone largely depends on the earthquake magnitude.
A change in the thermal regime of the epicentral zoneand its surroundings is one of the most pronounced changes that can be detectedby space-borne sensors such as Advanced Very High Resolution Radiometer (NOAAAVHRR) and the Moderate Resolution Imaging Spectroradiometer(MODIS Terra/Aqua).In spite of some skepticism regarding earthquake prediction (1), early warning signs of earthquakes arediverse, fleeting and often subtle, and they can also be surprisingly strong, even formoderate earthquakes (2), (3).

VRANCEA SEISMIC REGION

Vrancea seismic region in Romania is structurally and seismically complex area, bounded by latitudes 45.6 °N and 46.0 °N and longitudes 26.5 °E and 27.5 ° E(Figure1).

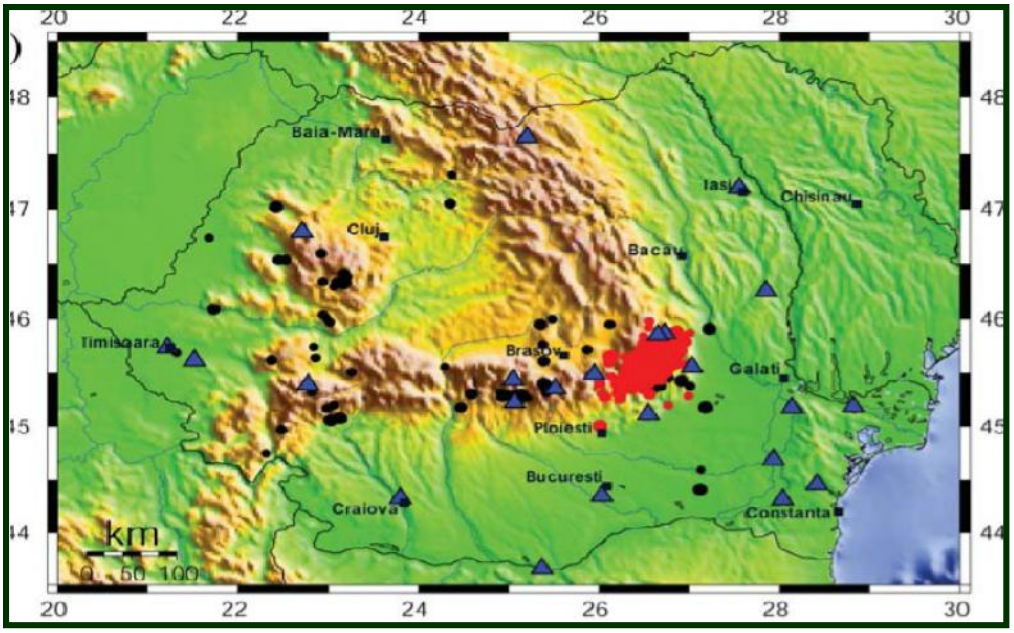

Figure 1. Vrancea active seismic region on Romania map(red zone)

Located at the sharp bend of the Southeastern Carpathians,is one of the most active intracontinental seismic areas in Europe, with high potential seismic hazard associated to a few strong intermediate depth earthquakes (1940, November, 10th, Mw = 7.7, *H* = 150 km; 1977, March, 4th, Mw = 7.4, *H* = 94 km; 1986, August, 30th, Mw = 7.1, *H* = 131 km; 1990, May, 30th, Mw = 6.9, *H* = 91 km; 1990, May, 31st, Mw = 6.4, *H* = 87 km; 2004, October 27th, Mw =5.9, *H* =96 km) (4). A narrow, near-vertical focal volume subducted at intermediate depths (60 - 220 km), supposed to be in a relic stage at present, is the site of an unusually intense seismicity (an average frequency of 3 shocks with moment magnitude Mw> 7 per century).

Surrounding Vrancea, the several seismic stations belonging to the Romanian Seismic Network are recording seismic and other geophysical, geoelectromagnetic, geodinamic and meteorological parameters. This study investigated: the March, 4th, with moment magnitude Mw = 7.4, *H* = 94 km earthquake, 1986, August, 30th, with moment magnitude Mw = 7.1, *H* = 131 km earthquake;andOctober 27th 2004 earthquake, with moment magnitude Mw =5.9 and epicenter depth of *H* =96 km. The strength of an earthquake is usually measured on different magnitude scales, but the moment magnitude (Mw) is regarded as the most representative value of the seismic source.

METHODS

Recent advances of information technology has allowed the development of tools and techniques to handle geological/geospatial data and/or derived. With differences in scales, datum, projections, formats, or resolution, the data are often difficult to handle and even more difficult to integrate.

During last decades the remote sensing data have been widely used for the assessment of prior and after strong earthquakes changes of several geophysical parameters as well as for the mapping of post earthquake damages (5).

As earthquakes (EQs) are large-scale fracture phenomena, associated fracture-induced physical fields allow a real-time monitoring of associated climate and geophysical variables anomalies in different spectral regions by satellite sensors.

These pre-signals suggest the existence of a strong coupling between the dynamics of lithospheric processes land atmospheric-ionospheric anomalies associated with seismic processes.

Based on multisensor satellite remote sensing continuous monitoring of land, ocean, atmosphere, and ionosphere parameters, have been strongly evidenced pre-earthquake changes in land, ocean, atmosphere, and ionosphere parameters (6), (7).
Through the analysis of different geophysical parameters and seismicity changestested over long periods of time, for earthquake prediction, scientists are continuing tosearch reliable precursory phenomena. Before a potential anomaly can be nominatedas a reliable precursor, it should pass or be proved by the following tests or analyses:whether it is an artificial anomaly, whether it correlates with an investigated event andwhether it is a random anomaly.
Satellite remote sensing applied for earthquake research can detect such phenomena, related with earthquakes, particularly the Earth's surface deformation, land and air surface temperatureand humidity, gas and aerosol content. Crustal deformations, both horizontal andvertical scaled from tens of centimeters to meters are recorded after the shock by the Interferometric Synthetic Aperture Radar (InSAR) technique withconfidence. Pre-earthquake deformations are rather small, on the order of centimeters. Some few cases ofdeformation mapping before the shock using satellite data in synergy with GPS data are known at present time. There are numerous observations of surface and near surface temperatureincreases of 3–5 °C prior to Earth crust earthquakes. Methods of earthquake prediction are developingusing thermal infrared (TIR) surveys. Have been reported also multiple evidence of gas and aerosol content changes before earthquakes are reported for in-situ observations. Satellite techniques allow also to measure the concentrations of gases in atmosphere: O_3, CH_4, CO_2, CO, H_2S, SO_2, HCl and aerosols. However thespatial resolution and sensitivity of modern systems restricts the application of satellite gas observationin seismology and the first promising results have been obtained only for ozone, aerosol andair humidity.
Natural phenomena and satellite data availability stimulated the analysis of the long time series of thermalimages in relation to earthquake hazard.
Climate oscillations have significantly contributed to the planet's evolution, including seismic and volcanic activity. Generally, geotectonic instability can be inferred from detailed geophysical, geological, andstructural studies of a seismic active area, but the triggering mechanism hasbeen always difficult to infer.

Data from satellite sensors, such as AVHRR on board the National Oceanic andAtmospheric Administration (NOAA) series satellites andMODIS Terra/Aqua on board the NASA Terra and AquaEarth Observation System satellitesprovide LST products retrieved for a specific area with a spatial resolution of about1 km, whereas the Spinning Enhanced Visible and Infrared Imager (SEVIRI) sensoron board the METEOSAT Second Generation (MSG) series geostationary satellitesretrieves LST at a lower spatial resolution (about 3 km).
This study used time series products of MODIS/Terra land surface temperature/emissivity(LST/E) 8-Day L3 Global 1 km SIN Grid MOD11A2 LST_Day_1 km data over different periods oftime provided by Oak RidgeNationalLaboratoryDistributedActiveArchiveCenter(ORNL DAAC) (http://daac.ornl.gov/MODIS/modis.html). MODIS/Terra LST/EDaily L3 Global 1 km SIN Grid satellite data were used for comparison of the results.
In addition, NOAA-AVHRR data-derived land surface temperature (LST), air temperature and outgoing longwave radiation (OLR) provided by the NOAA/ESRL Physical SciencesDivision, Boulder, CO, USA (http://www.esrl.noaa.gov/psd/) have been used.
Meteorological data around Vrancea region in Romania and anomaly were provided by the National Administration of Meteorology, in addition, in-situmeteorological data were compared with satellite data. Land surface temperature anomalies were obtained by subtracting the multi-year mean from the area-averaged values and dividing by multi-year mean values.

Outgoing Longwave Radiation (OLR) which is the emission to space of terrestrial radiation from the top of the Earth's atmosphere is controlled by the temperature of the earth and the atmosphere above it, the water vapor content in the atmosphere, and the clouds. OLR is a NOAA polar-orbiting satellite derived measurement of the radiative character of energy radiated from the warmer earth surface to cooler space in the 10–12 μm infrared windows.
The interpolated OLR data are continuous spatially as well as temporally. The estimates of interpolated OLR values (W/m^2) originally observed by polar orbiting NOAA are based on dedicated developed algorithms. Maximum and minimum OLR values ranges including other parameters were defined in the analyzed earthquake case

RESULTS

Space-time anomalies of Earth's emitted radiation (radon in underground water and soil, thermal infrared in spectral range measured from satellite months to weeks before the occurrence of earthquakes etc.), and electromagnetic anomalies are considered as pre-seismic signals. This energy transformation may result in enhanced transient thermal infrared (TIR) emission, which can be detected through satellites equipped with thermal sensors like AVHRR (NOAA), MODIS (Terra/Aqua) (8). This paper presents observations made using time series NOAA-AVHRR and MODIS satellite data–derived land surface temperature (LST) and outgoing long-wave radiation (OLR) as well as air temperature anomalies recorded for selected earthquakes to be analyzed in seismic Vrancea region, Romania, using anomalous TIR signals as reflected in LST rise and high OLR values which followed similar growth pattern spatially and temporally. In all analyzed cases, starting with almost one week prior to a moderate or strong earthquake a transient thermal infrared rise in LST of several Celsius degrees (^oC) and the increased OLR values higher than the normal have been recorded around epicentral areas, function of the magnitude and focal depth, which disappeared after the main shock. As Vrancea area has a significant regional tectonic activity in Romania and Europe, the joint analysis of geospatial and in-situ geophysical information is revealing new insights in the field of hazard assessment.

Land Surface Temperature

The ability to detect land surface temperatures from space is well developed, and there have been some reports of surface temperature changes prior to earthquakes. These may involve changes in the circulation patterns of groundwater bringing water of different temperature to the surface. This possible precursor is interesting from the remote-sensing viewpoint. TIR (thermal infrared) spectral bands of different satellites like MODIS, NOAA AVHRR, ASTER, Landsat TM/ETM can produce

such information. The analysis of the time series LST (Land Surface Temperature) maps for different seismic regions prior strong earthquakes, evidenced building up of thermal anomalies.

Based on time-series MODIS/Terra Land Surface Temperature/Emissivity (LST) 8-Day L3 Global 1km SIN Grid, MOD11A2/LST_Day_1km was represented land surface temperature variation during 2004 year over Vrancea region (Figure 2) centered on earthquake of 27th October 2004 epicenter (45.787 N, 26.622 E), 101 km x 101 km surface area .

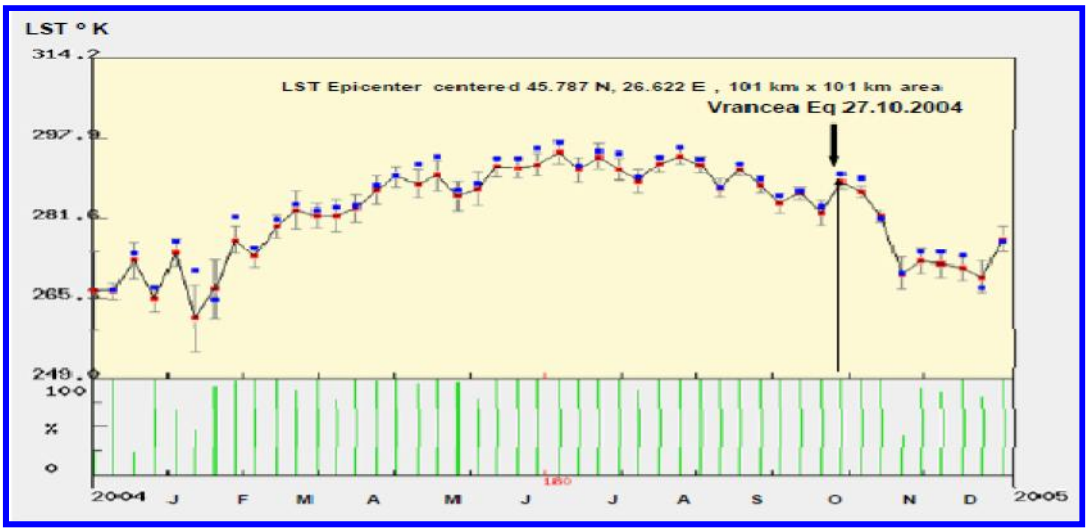

Figure 2. Land surface temperature (LST) variation during 2004 year over epicentral Vrancea region based on MODIS Terra time series data.

Time series satellite data analysis revealed increase of land surface temperatures LST around epicentral area ranging 5–10°C. MODIS classification considered Pixel Aggregation Method (PAM) and found that 3559 of 10201 pixels [34.89%] were belonging to the same class as the center pixel "(5) Mixed Forests". A clear rise of land surface temperature in epicentral area and surroundings was recorded by MODIS time series satellite data.For October 27th 2004, Mw =5.9, and epicenter depth of *H* =96 km in Vrancea area the thermal anomalies of land surface temperature have been developed with about 4–7 days or more prior to the main event depending upon the magnitude and focal depth and disappeared after the main shock.

Air Temperature

Thermal observations from NOAA AVHRR satellites, NCEP/NCAR Reanalysis, based on climate data 1981-2010 indicate a significant change of the air temperature and near-surface atmosphere layers for strong earthquake March, 4th, Mw = 7.4, *H* = 94 km earthquake in Vrancea region. Significant surface air temperature anomaly in South-Eastern Europe region centered on RomanianearbyVranceaepicenter prior to this earthquake was observed withonemonth before the main shock (Figure 3) and on Vrancea (Figure 4).

Immediately after the shock March, 4th, this anomaly continued more several days. Ground observations confirmed satellite data: air and land surface temperature changed simultaneously with thermal anomaly variation.

Ten years of Meteosat TIR observations have been analyzed in order to characterize the TIR signal behavior at each specific observation time and location. Space-time TIR signal transients have then been analyzed, both in the presence (validation) and in the absence of seismic events, looking for possible space-time relationships.

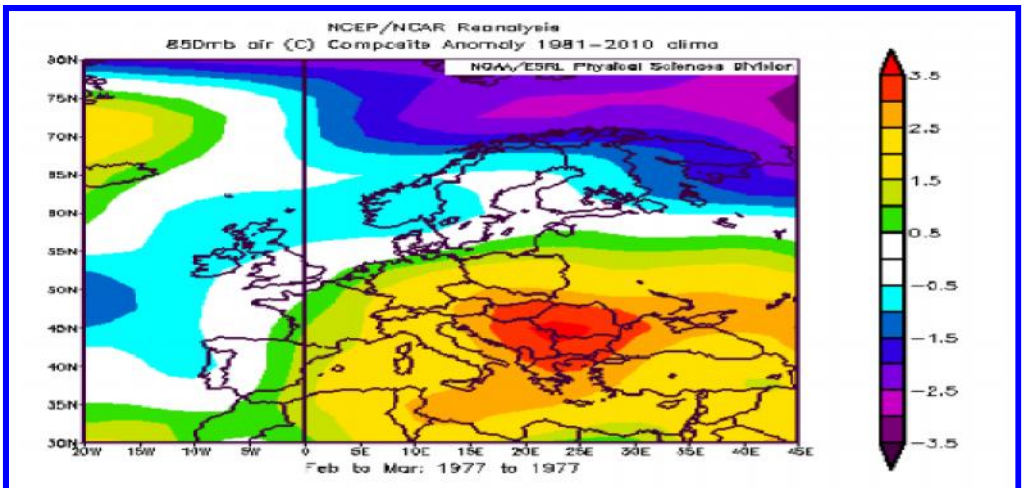

Figure3.Air temperature anomaly over large area in South-Eastern Europe around Vrancea seismic region prior one month before March, 4th, Mw = 7.4, H = 94 km earthquake

It is known that satellite thermal survey has a relatively long history of applications in seismology. Most of its advantages and limits are well known. Two main problems limit thermal data utilization: cloud penetration and geological situation. Surface conditions such as vegetation and climate conditions like as precipitations, wind, etc. also strongly influence thermal effects.

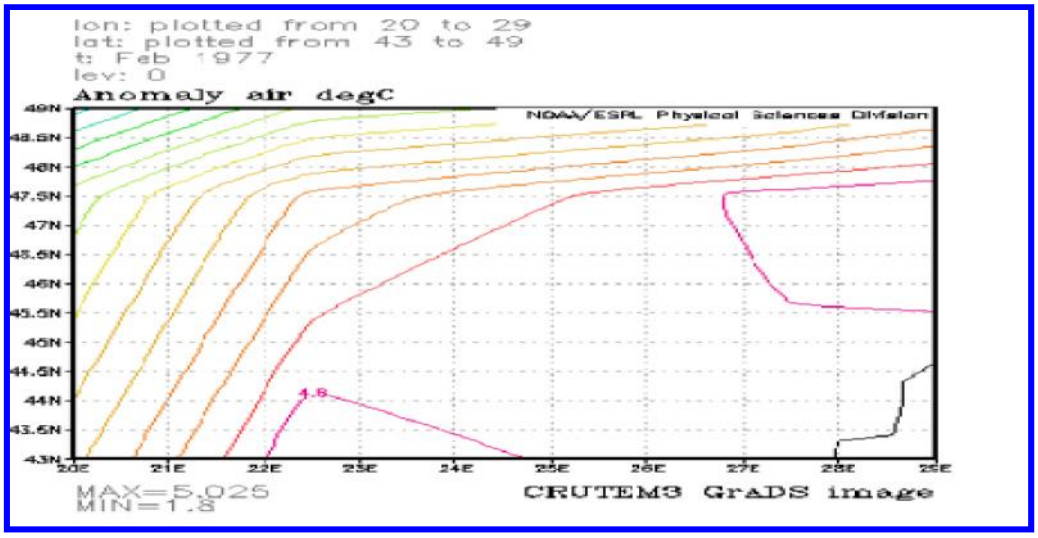

Figure4.Air temperature anomaly over Vrancea region one month before March, 4th, Mw = 7.4, H = 94 km earthquake

One month before ofVrancea1986, August, 30thearthquake, with moment magnitude Mw = 7.1, *H* = 131 kmearthquake have been recorded surface air temperature anomalies (Figure 5).

In order to study the relationship between the air temperature and 27th October 2004 earthquake, have been analyzed time-series of mean daily air temperature and anomaly data for period of 15 October -15 November 2004, on the base period of normals 1981-2010 around Vrancea region provided by NOAA satellites. The positive air temperature anomaly started developing to North West and South East of the epicentral area, air temperature showing a rise of around 4.8^{o} C- 8^{o} C

during 24-27 October 2004 (Figure 6), in good correlation with in-situ measurements, which revealed a pronounced increase of air temperature over Vrancea region. After the main shock of 27th October, during 27 October -3 November 2004, air temperature recorded a gradual increase with a maximum of 5°C degrees between 30 October and 3 November.

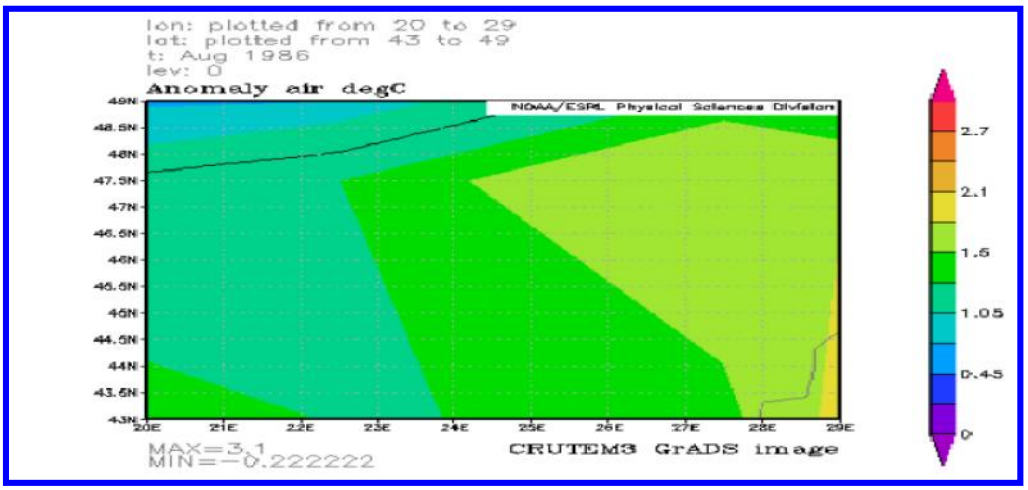

*Figure5.Air temperature anomaly over Romania one month before*Vrancea1986, August, 30th

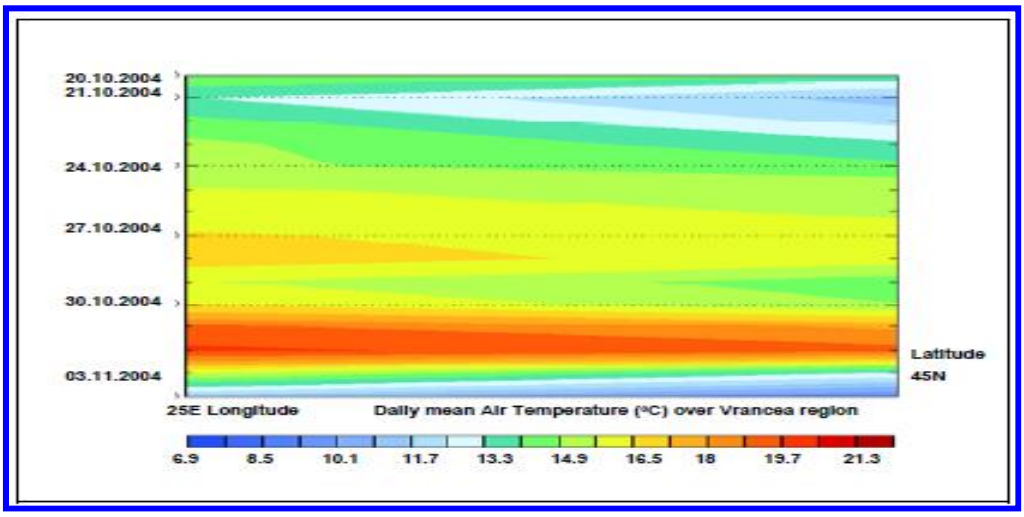

Figure6.Daily MEAN air temperature over Vrancea region before and after Vrancea 2004,Oktober 27th earthquake

Outgoing Longwave Radiation (OLR)

Thermal anomalies before strong earthquakes are observed at different levels, starting from the ground surface up to the top of clouds altitude. The most promising presignal is the Outgoing Longwave Radiation (OLR) anomaly measured at the top of clouds level. Its advantage is that it is measured within the infrared transparency window of 8–12 μ m and does not separate clouds.

For October 27th 2004, Mw =5.9, and epicenter depth of *H* =96 km in Vrancea area the thermal anomalies of OLR have been developed with about 4–7 days or more prior to the main event function of magnitude and focal depth and disappeared after the main shock. OLR registered

anomalies ranged 32–48 W/m^2 higher than the normal values for the same period of time and ten years of measurements.

Figure 7 presents daily means OLR variationbetween 20 October 2004 till 3November 2004, which evidenced gradually increase of the outgoing long-wave radiation OLR emitted by land surface in Vrancea epicentral area before 5.9 M_w earthquake registered on October 27th 2004.The magnitude of the recorded mean OLR anomalies increased firstly starting from 24 October 2004, with a maximum value between 25-26 Octobers and then decreased gradually till 27th October in the morning, after that increased again between middle of the day 27th October and 30th October. OLR anomalies covered an extended area described by latitudes 45N – 47N and longitudes 25E – 27E and were distributed along the fault zone system in the Vrancea region.

The interpolated OLR data are continuous spatially as well as temporally. The estimates of interpolated OLR values (W/m^2) originally observed by polar orbiting NOAA are based on dedicated developed algorithms. Maximum and minimum OLR values ranges including other parameters were defined in each analyzed earthquake case.

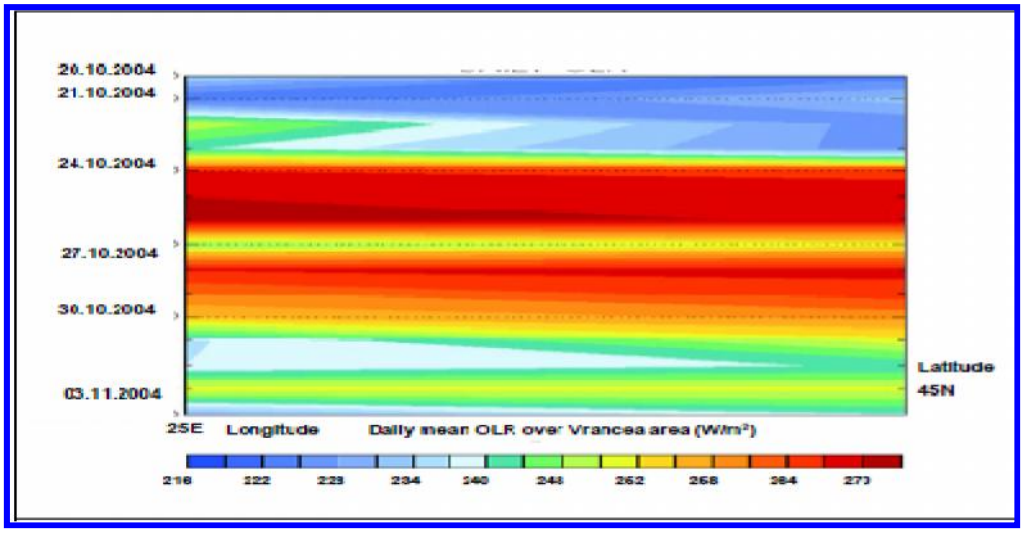

Figure7. Dailymean OLR over Vrancea region before and after Vrancea 2004, October 27th earthquake

The increase in air and land surface temperature as well as of OLR near epicentral areas can be attributed to enhanced greenhouse gas emission from the squeezed rock pore spaces and/or to the activation of p-holes in stressed rock volume and their further recombination at rock-air interface. OLR is dependent of local meteorological parameters temperature and humidity and changes in these variables may be responsible for anomalous OLR values.

CONCLUSIONS

Geo-hazards such as earthquakes, landslides, and weather related hazards are among the strongest sudden impacts on modern life and property in Romania. The assessment, surveillance and mitigation of geo-hazards in Romania are a mandatory task of the geosciences community. Seismic precursors assessment in the most active seismic area Vrancea in Romania are multifold and combine investigations of recurrence intervals or probability of occurrence of events together with their probable impact on life and property, and the investigation of deformation and rates within different time scales, including geological studies, paleoseismology, and the monitoring of seismicity and currently accumulating deformation. The present results show existence of coupling

between lithosphere-atmosphere associated with preparation and seismic event occurring. Such results of pre-earthquake signals are promising and can contribute significantly in the future towards forecasting the impending earthquakes in tectonically active region Vrancea, which represents a real seismic hazard for South-Eastern Europe. Thermal anomalies research in Vranceaseismic active area is developing in the direction of seismic activity monitoring and close integration with ground observations.The anomalies of air and land surface temperatures as well as of outgoing longwave radiation observed some days to weeks before main seismic shocksprovide early warning signals in all analyzed earthquake test cases.The present results show existence of coupling between lithosphere-atmosphere associated with preparation and seismic event occurring. Such observations demonstrate promising results, but new data accumulation is required. The nature of air and land surface temperature as well as outgoing longwave radiation anomalies still remains unclear. The joint analysis of geospatial and in-situ geophysical information will reveal new insights in the field of earthquake hazard assessment.

ACKNOWLEDGEMENTS

This work was supported by Romanian National Authority for Scientific Research, Program STAR Contract 73/2013 VRAFORECAST,and by grant CNDI– UEFISCDI PN-II-PT-PCCA-2011-3.2-1322 ALL-SKY.

REFERENCES

1 Geller, R., (2011). Shake-up time for Japanese seismology. Nature, 472:407–409.

2 Freund, F., (2011). Seeking out Earth's warning signals. Nature, 473: 452.

3 Zoran, M., (2012). MODIS and NOAA-AVHRR land surface temperature data detect a Thermalanomaly preceding the 11 March 2011Tohoku earthquake. International Journal of Remote Sensing, 33:21: 6805-6817.

4 Radulian, M., K.P.Bonjer, E.Popescu, M.Popa, C.Ionescu, B.Grecu, (2004). The October 27th, 2004 Vrancea (Romania) earthquake. ORFEUS Newsletter, 7: 1

5 Singh, R.P., S.Bhoi, A.K. Sahoo, (2001). Surface manifestations after the Gujarat earthquake. Current Science, 80:1376–1377

6 Okada, Y., S. Mukai, R.P. Singh, (2004). Changes In Atmospheric Aerosol Parameters After Gujarat Earthquake Of January 26, 2001. Advances In Space Research, 33: 254–258.

7 Ouzounov, D. ,F. Freund, (2004). Mid-Infrared Emission Prior to Strong Earthquakes Analyzed by Remote Sensing Data. Advances In Space Research. 33: 268–273

8 Tramutoli V., C.Aliano, R.Corrado, C.Filizzola, N.Genzano, M.Lisi, G.Martinelli, N.Pergola, (2013). On the possible origin of thermal infrared radiation (TIR) anomalies inearthquake-prone areas observed using robust satellite techniques (RST). Chemical Geology 339:157–168.

MULTI- AND HYPERSPECTRAL SATELLITE SENSORS FOR MINERAL EXPLORATION, NEW APPLICATIONS TO THE SENTINEL-2 AND ENMAP MISSION.

Christian Mielke[1], Nina Kristine Boesche[2], Christian Rogass[3] , Karl Segl[4] and Hermann Kaufmann[5]

1. HelmholtzZentrum, German Research Centre for Geoscience, GFZ, Potsdam, Germany; christian.mielke@gfz-potsdam.de
2. HelmholtzZentrum, German Research Centre for Geoscience, GFZ, Potsdam, Germany; nina.boesche@gfz-potsdam.de
3. HelmholtzZentrum, German Research Centre for Geoscience, GFZ, Potsdam, Germany; christian.rogass@gfz-potsdam.de
4. HelmholtzZentrum, German Research Centre for Geoscience, GFZ, Potsdam, Germany; karl.segl@gfz-potsdam.de
5. HelmholtzZentrum, German Research Centre for Geoscience, GFZ, Potsdam, Germany; hermann.kaufmann@gfz-potsdam.de

ABSTRACT

Imaging spectroscopy is a widely used tool in mineral exploration today where exploration companies offer the full service package to their clients: (data acquisition, preprocessing and product delivery). These exploration projects rely mainly on airborne imaging spectrometers such as Hymap, AISA or HySpex. This data is usually scarce and expensive and may not be available to academic research. The only operational spaceborne imaging spectrometer that covers the full spectral range from the visible to the shortwave infrared is Hyperion aboard EO-1, which has been providing data for over a decade now. New and advanced spaceborne imaging spectrometers such as the Environmental Mapping and analysis Program (EnMAP) will provide new data for research in the field of imaging spectroscopy for mineral exploration. This study presents a comparison of the mapping capabilities between the Hyperion and EnMAP sensors, on the basis of simulated EnMAP data. This is shown with an example from a porphyry copper complex in southern Namibia (Haib River). In addition to that results from multispectral sensors (Landsat-8 OLI, EO-1 ALI and simulated data from the next generation Sentinel-2) are shown to illustrate their potential to map the gossan-outcrops at the Haib River Complex using the Iron Feature Depth (IFD).

Keywords: EnMAP, Sentinel-2, EO-1, IFD, USGS MICA

INTRODUCTION

The use of airborne hyperspectral imaging spectrometers such asHymap[1] or HySpex[2] is a common approach in exploration campaigns today[3]. These airborne sensors combine a good signal-to-noise ratio and a good spectral and spatial resolution. However, the usage of these systems in large and remote areas involves high costs due to the difficult logistics that is involved in airborne hyperspectral campaigns. Therefore, the usage of multispectral imagers, such as the Operational Land Imager aboard Landsat-8 [4] and Sentinel-2[5] in combination with hyperspectral spaceborneinstruments such as Hyperion [6] andEnMAP[7], will increase in geological mapping and exploration campaigns to reduce airborne related costs to a minimum possible extent. This is due to the open data policy that accompanies these spaceborne missions as in case of the National Aeronautics and Space Administration's (NASA's) EO-1 satellite, or NASA's Landsat program. The future European Sentinel-2 and the future German EnMAP mission will supply data with a similar data usage policy

to the geoscientific community worldwide. The here presented study, therefore, aims at illustrating synergetic effects in mineral exploration that emerge from the usage of these spacebornemultispectral and hyperspectral instruments. This is done for the Haib River porphyry copper deposit in the lower Orange River area, shown in Figure 1, which has been identified as one of the oldest porphyry copper deposits in the world ([8],[9])situated in the Namaqua Mobile Belt [10]. Early exploration work up until the work of Minnit[9] is advocating for a classical succession of hydrothermal alteration zones, which indicate a porphyry copper deposit [9]. Therefore, this area represents a unique test site for the demonstration of new remote sensing techniques for mineral mapping and exploration [11].

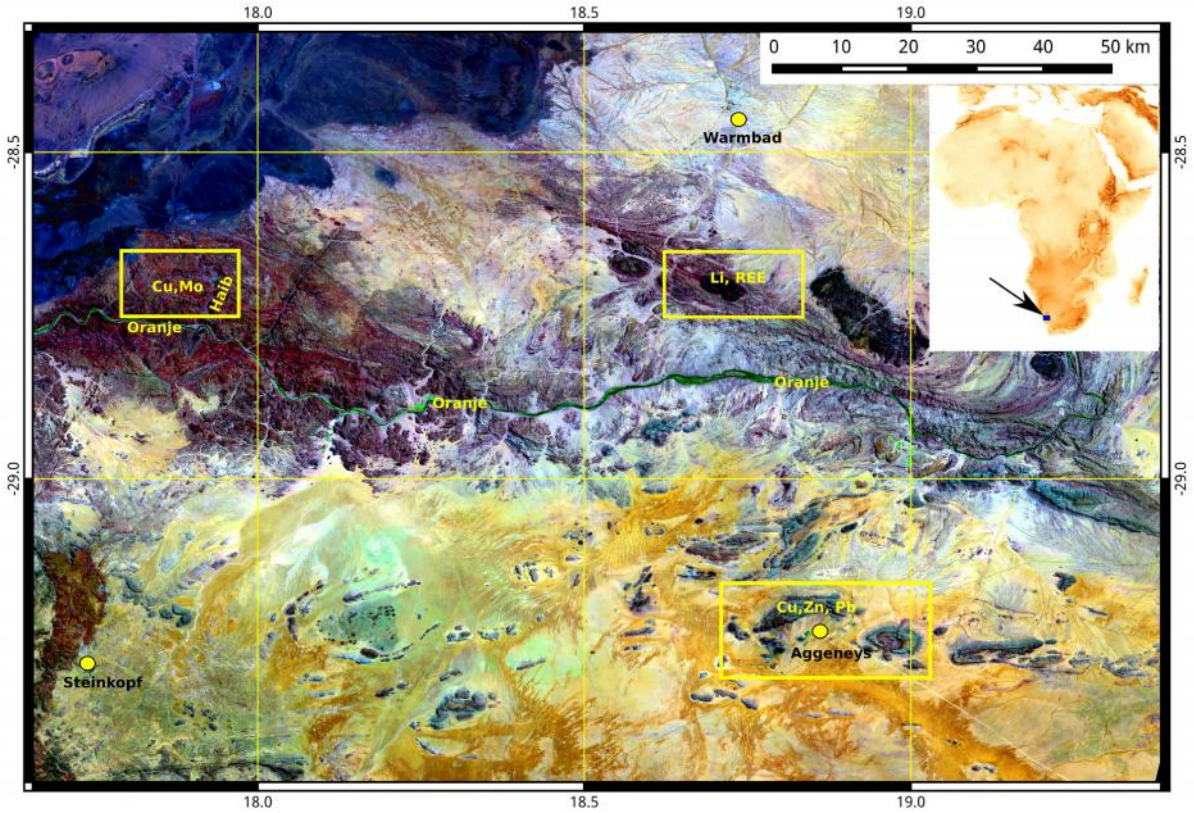

Figure 1: Landsat-8 OLI false color composite (OLI scene ID: LC81760802014026LGN00) (R: 2200 nm, G: 860 nm, B: 560 nm) showing the Orange River area with the three major mineral deposit sites in the border region of South Africa and Namibia. These are the Aggeneys lead-zinc deposit, the lithium pegmatites and rare earth element bearing site close to Tantalite Valley, south of Warmbad and the Haib River Complex with its copper deposit.

METHODS

For this study data was acquired from the EO-1 Hyperion and ALI sensors, as well as data from Landsat-8 OLI, shown in Figure 1. Airborne hyperspectral data (Hymap) from the Geological Survey of Namibia was used to simulate the future multispectral Sentinel-2 and the future hyperspectral EnMAP sensor using theEnMAP End-to-End simulation tool of Segl et al. [12]. This enables the demonstration of the full capacity of Sentinel-2 and EnMAP and facilitates algorithm development and validation prior to the launch of these sensors. Fieldwork was carried out for sample collection and field spectrometer measurements for verification purposes. In order to exploit the large spatial coverage of multispectral spaceborne instruments and the high spectral resolution and ability to characterize the surface mineralogy the Iron Feature Depth (IFD) [13] is used for mapping the spa-

tial distribution of secondary iron bearing minerals such as goethite, hematite and jarosite. These minerals are essential in the process of exploration, where the occurrence of gossans may show zones of sulfide oxidation and metal leaching, which can be indicative for copper exploration [14] and material transport from mine waste sites [13]. Figure 2 shows that the IFD, which exploits the 900 nm iron absorption feature in a three-point band-depth fashion, is able to highlight the abundance of secondary iron bearing minerals. Even OLI is able to map the iron related absorption feature at 900 nm, due to its band layout, as shown in Figure 2.Hyperspectral spaceborne data in combination with the USGS Mineral Identification and Characterization Algorithm (MICA) was used [15] for mapping the mineral distribution of the alteration minerals from the hyperspectral spaceborne data, which complements the IFD analysis of the multispectral spaceborne systems.

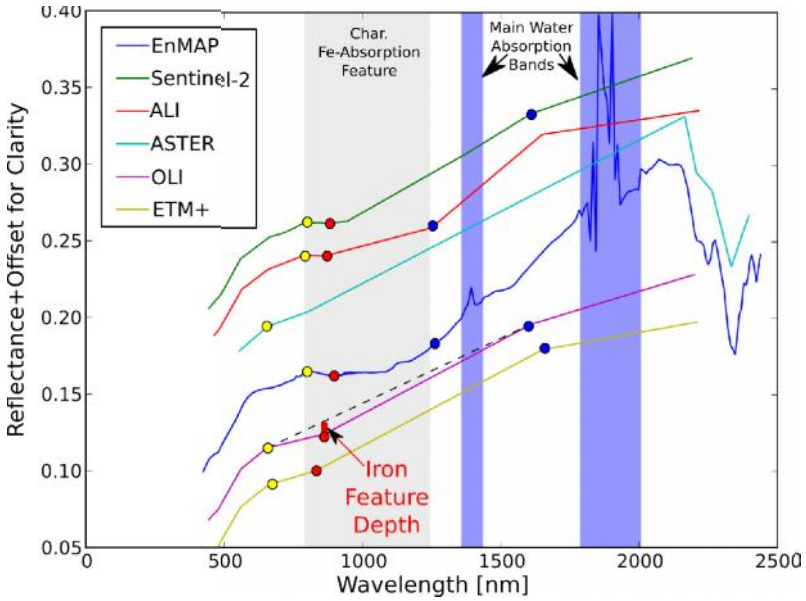

Figure 2: Definition of the Iron Feature Depth for selected multispectral sensors (hyperspectral EnMAP data for reference) to illustrate the capacity of the IFD for mapping the iron absorption feature in a spectrum from the Haib River Complex.

RESULTS

Figure 3 shows IFD results from the Haib River Complex calculated from simulated Sentinel-2 data, from data takes of EO-1 ALI and from Landsat-8 OLI.The data coverage differs between the three sensors due to a different swath width especially if the narrow coverage of ALI is considered. Therefore, the gossan occurrence the northwest outside the main mineralized zone is not shown on the ALI data due to a lack of ALI data coverage in this region. Sentinel-2 and OLI do however highlight this gossan occurrence, although the IFD values of OLI are much lower in this region than in the corresponding Sentinel-2 data. This is due to the different band layout and spectral coverage of the two multispectral spaceborne sensors, illustrated in Figure 2. The differences in the spatial pattern of the IFD in the main mineralized zone can be also explained by the differences in the band layout of the three sensors. Sentinel-2 and ALI are better equipped to map the 900 nm iron absorption feature, because of the number, position and bandwidth of their red, near-infrared and shortwave infrared 1 channels in comparison to Landsat-8 OLI.

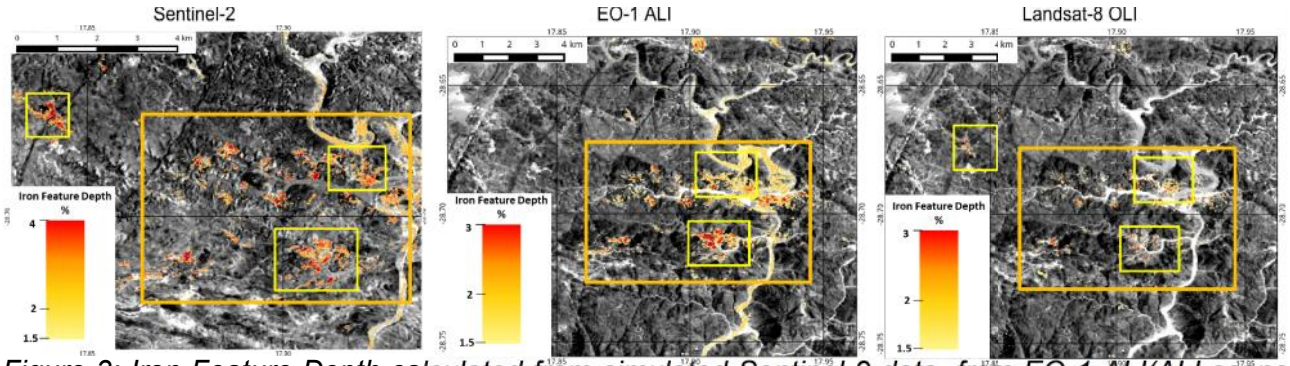

Figure 3: Iron Feature Depth calculated from simulated Sentinel-2 data, from EO-1 ALI(ALI scene IDs: EO1A1760802013267110K,EO1A1760802014013110PF) and from Landsat-8 OLI, (OLI scene ID: LC81760802014026LGN00) overlain over the Landsat-8 OLI near-infrared channel. Yellow boxes outline the occurrences of gossans, whilst the orange box outlines the main mineralized zone of the deposit.

Hyperspectral spaceborne data from EO-1 Hyperion and from simulated EnMAP data complements the analysis from the multispectral spaceborne sensors by showing the spatial distribution of minerals that highlight zone of alteration mineralogy. These zones are outlined by yellow and blue boxes in Figure 4, where typical alteration minerals such as alunite, kaolinite and montmorillonite have been detected via the USGS MICA analysis [15]. The spatial co-occurrence between the clay mineral anomaly in the blue boxes and the westernmost IFD area suggests a mineralogical exploration anomaly that needs to be evaluated by further exploration work in the field.

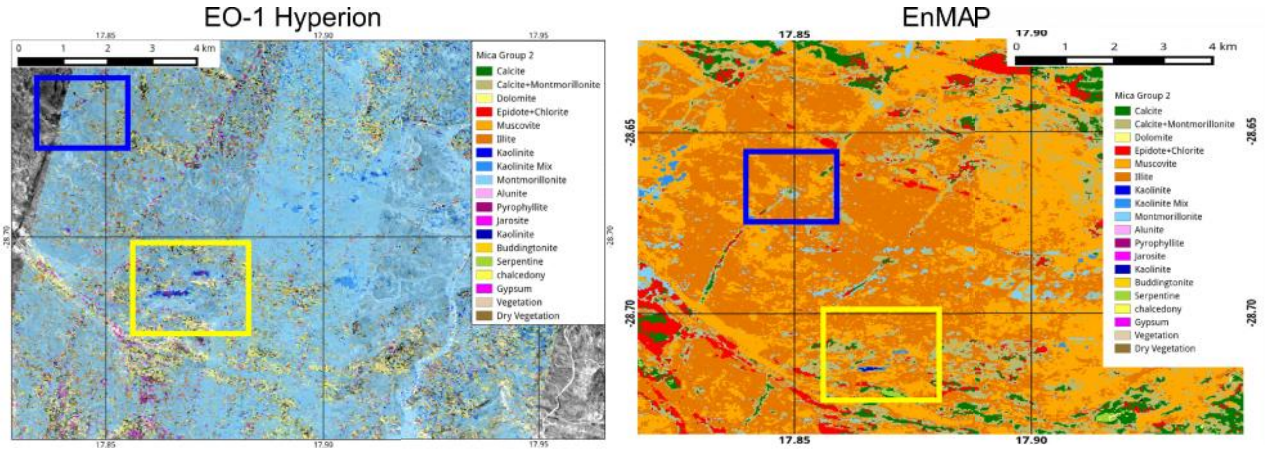

Figure 4: USGS MICA group 2 analysis results highlighting alteration zones within the Haib River Complex (yellow boxes). Analysis were carried out on EO-1 Hyperion data (Hyperion scene IDs: EO1H1760802013267110K,EO1H1760802014013110PF). Please note that the clay mineral occurrence in the Hyperion data and in the simulated EnMAP data (blue boxes)spatially coincides with the IFD anomaly in Figure 3 on the Sentinel-2 and OLI data on the westernmost dike structure.

CONCLUSIONS

This study showed that a combined, complementary use of multi- and hyperspectral spaceborne data yields high potential for mineral exploration. The spatial occurrence of gossans can be mapped from multispectral spaceborne data using the IFD [13] as shown in Figure 3. Hyperspectral spaceborne data is then able to further highlight zones of alteration mineralogy, if analyzed with expert systems, such as the USGS MICA [15]. This combination of potential gossan anomalies and alteration mineralogy then yields important target zones for further exploration work, which may include high spatial resolution hyperspectral airborne data takes and zones for further field investigation. This can then help to locate the zones of potential sulfide oxidation (zones of high secondary iron mineral abundance and hence zones with a strong positive IFD) and supergene copper enrichment [14]. Figure 3 also shows that next generation multispectral spaceborne sensors such as ESA's Sentinel-2 show a more detailed picture of potential gossan anomalies than state of the art sensors such as Landsat-8 OLI, due to their band layout and higher spectral resolution in the near-infrared. The differences in the MICA analysis between the simulated EnMAP data and Hyperion are due to the generally lower, unfavorable signal-to-noise ratio of Hyperion if compared to the high signal-to-noise ratio of EnMAP. However both sensors show the two elliptical alteration mineral anomalies outlined in the yellow boxes of Figure 4. This shows that a combination of next generation multispectral sensors, such as the Sentinel-2 for gossan detection via the IFD and next generation hyperspectral sensors, such as EnMAP for identification of alteration mineralogy and mapping will likely reduce costs in future exploration campaigns by further focusing expensive airborne hyperspectral campaigns and field work on potential target areas that have been highlighted and interpreted as mineralogical exploration anomalies of interest.

ACKNOWLEDGEMENTS

Thanks to the Geological Survey of Namibia, Gaby Schneider and Ivor Kahimise for providing the 2008 Haib River HyMAP survey as EnMAP simulation input. Thanks to Stuart Frye and the EO-1 science team for providing the data takes of EO-1 ALI and Hyperion. This work was funded by the German Federal Ministry of Economics and Technology (BMWI 506 50EE1012/EnMAP) within the framework of EnMAP (Environmental Mapping and Analysis Program).

REFERENCES

1. Cocks, T.; Jenssen, R.; Stewart, A.; Wilson, I.; Shields, T. The HyMapTM airborne hyperspectral sensor: the system, calibration and performance. In *1st EARSEL Workshop on Imaging Spectroscopy, Zurich, Switzerland*; 1998; pp. 37–42.

2. Baarstad, I.; Løke, T.; Kaspersen, P. ASI–A new airborne hyperspectral imager. In *Proceedings of the 4th EARSeL Workshop on Imaging Spectroscopy–New Quality in Environmental Studies. Warsaw, Poland*; 2005.

3. Van der Meer, F. D.; van der Werff, H.; van Ruitenbeek, F. J. A.; Hecker, C. A.; Bakker, W. H.; Noomen, M. F.; van der Meijde, M.; Carranza, E. J. M.; Smeth, J.; Woldai, T. Multi-and hyperspectral geologic remote sensing: A review. *Int. J. Appl. Earth Obs. Geoinformation***2012**, *14*, 112–128.

4. Irons, J. R.; Dwyer, J. L.; Barsi, J. A. The next Landsat satellite: The Landsat Data Continuity Mission. *Remote Sens. Environ.***2012**, *122*, 11–21.

5. Drusch, M.; Del Bello, U.; Carlier, S.; Colin, O.; Fernandez, V.; Gascon, F.; Hoersch, B.; Isola, C.; Laberinti, P.; Martimort, P.; Meygret, A.; Spoto, F.; Sy, O.; Marchese, F.; Bargellini, P. Sentinel-2: ESA's Optical High-Resolution Mission for GMES Operational Services. *Remote Sens. Environ.***2012**, *120*, 25–36.

6. Ungar, S. G.; Pearlman, J. S.; Mendenhall, J. A.; Reuter, D. Overview of the Earth Observing One (EO-1) mission. *IEEE Trans. Geosci. Remote Sens.***2003**, *41*, 1149–1159.

7. Kaufmann, H.; Segl, K.; Chabrillat, S.; Hofer, S.; Stuffler, T.; Mueller, A.; Richter, R.; Schreier, G.; Haydn, R.; Bach, H. EnMAP a hyperspectral sensor for environmental mapping and analysis. In *Geoscience and Remote Sensing Symposium, 2006. IGARSS 2006. IEEE International Conference on*; IEEE, 2006; pp. 1617–1619.

8. Pirajno, F. *Hydrothermal Processes and Mineral Systems*; Springer-Verlag, 2009.

9. Minnit, R. C. A. Porphyrry Copper-Molybdenium Mineralization at Haib River, South West Africa/Namibia. In *Mineral Deposits of Southern Africa Vol I&II*; Anhaeusser C.R.; Maske, S., Eds.; Geological Society of South Africa: Johannesburg, 1986; Vol. 2, pp. 1567–1585.

10. Blignault H.J. *Structural-Metamorphic Imprint on Part of the Namaqua Mobile Belt in South West Africa*; Chamber of Mines Precambrian Research Unit; University of Cape Town: Cape Town, 1977.

11. Oshigami, S.; Yamaguchi, Y.; Uezato, T.; Momose, A.; Arvelyna, Y.; Kawakami, Y.; Yajima, T.; Miyatake, S.; Nguno, A. Mineralogical mapping of southern Namibia by application of continuum-removal MSAM method to the HyMap data. *Int. J. Remote Sens.***2013**, *34*, 5282–5295.

12. Segl, K.; Guanter, L.; Rogass¸, C.; Kuester, T.; Roessner, S.; Kaufmann, H.; Sang, B.; Mogulsky, V.; Hofer, S. EeteS - The EnMAP End-to-End Simulation Tool. *IEEE J. Sel. Top. Appl. Earth Obs. Remote Sens.***2012**, *5*, 522–530.

13. Mielke, C.; Boesche, N. K.; Rogass, C.; Kaufmann, H.; Gauert, C.; de Wit, M. Spaceborne Mine Waste Mineralogy Monitoring in South Africa, Applications for Modern Push-Broom Missions: Hyperion/OLI and EnMAP/Sentinel-2. *Remote Sens.***2014**, *6*, 6790–6816.

14. William X. Chavez Supergene Oxidation of Copper Deposits: Zoning and Distribution of Copper Oxide Minerals. *Soc. Econ. Geol. Newsl.***2000**, 9–21.

15. Kokaly, R. F. Spectroscopic remote sensing for material identification, vegetation characterization, and mapping. In; Shen, S. S.; Lewis, P. E., Eds.; 2012; pp. 839014–839014–12.

HIGH RESOLUTION REMOTE SENSING STEREO-DATA AND GIS FOR OPEN PIT MINE MONITORING

Nikolaos G. Argyropoulos[1] Konstantinos G. Nikolakopoulos[1], *and* Konstantina Dimitropoulou[1]

1. University of Patras, Department of Geology, Patras, Greece;
knikolakop@upatras.gr, n.argiropgeo@gmail.com, kostantina_4@hotmail.com

ABSTRACT

The scope of this project is the periodic monitoring of the excavation volumes of open-pit mines, using high resolution satellite imagery stereopairs and photogrammetric methods. Two different mines located the first one at North Greece and the second one in Attiki Peninsula compose the study areas. Cartosat and ALOS Prism stereo pairs with 2.5m spatial resolution were used. The same ground control points were used for the creation of the DSMs from both CARTOSAT and ALOS PRISM stereopairs in order to eliminate horizontal and vertical discrepancies. Using LPS 3D models of the open mines were created. The head and the foot of every plane in the mine was digitized. The final step was the comparison of both 3D models' shapefiles using ArcMap 10.1® in order to calculate the excavation volumes. The excavation volumes were calculated taking into account the area of the planes and the height of every plane and the results are presented in this paper.

INTRODUCTION

A Cartosat-1 stereopair was used in order to evaluate the accuracy of ASTER and SRTM DEM (1). Although remote sensing technology has been available for many years, it has rarely been used for monitoring mining activity. Recent studies indicate that remote sensing is also a valuable tool for managing and planning certain aspects of the mining operation. On previous studies, images captured by ASTER Level 3A01 (3D Ortho Data Set), Landsat 5, and Landsat 7 satellites between 2001 and 2009 (2), and Landsat-TM and ERS-1 data sets acquired from 1989 to 1994 (3) were used to examine the areal expansion of quarries and the affect it has on vegetation. The differential interferometric synthetic aperture radar (SAR) (DInSAR) technique is used to derive the temporal land subsidence information in the Fengfeng coal mine area, Hebei province in China (5) and to depict the evolution of ground subsidence caused by repeated coal excavation (13). InSAR was used to monitor land subsidence in another mining city (12). The combination of InSAR and GPS technology is also used to monitor subsidence in coal mining areas (15, 16) In other similar studies, the researchers used a small number of GCPs derived from GPS Surveys to create stereo models from ALOS PRISM and Cartosat-1 data. (4, 6, 7, 8, 9, 10, 11, 14).
ERDAS Leica Photogrammetry Suite was also used by other researchers in order to create stereo models and Orthoimages (4, 9, 10, 11).

METHODS

The study was carried for two areas in Greece, one limestone open-pit mine in Markopoulo, Attiki peninsula and one in Polygyros, Chalkidiki peninsula. Two stereo-pairs, with 2.5m spatial resolution, were acquired for each study, one from the CARTOSAT-1 satellite and one from the ALOS satellite.

Cartosat and ALOS Prism stereo pairs with 2,5m spatial resolution were used. The CARTOSAT-1 spacecraft launched by the Indian Space Research Organization in May 2005 is dedicated to stereo viewing for large-scale mapping and terrain modeling applications. It is configured with two panchromatic cameras, AFT (Afterward looking) and FORE (Foreword looking) with a spatial resolution of 2.5 m, which facilitates along-track stereo vision of the imaging scene. It covers a swath of ≈30 km with a base-to-height ratio of 0.62. The time difference between the acquisitions of the same scene by two cameras is about 52 sec. The PRISM sensor onboard ALOS contains three independent optical systems (radiometers) that allow for viewing in the Nadir direction, as well as forward and backward directions. This allows for the production of a stereoscopic image along the satellite's track. Forward and backward radiometers are inclined + and – 23.8 degrees from nadir to realize a base-to-height ratio of one. PRISM data is collected in a single band (panchromatic) with a wavelength of 0.52 to 0.77 micrometers. The spatial resolution of PRISM is 2.5m (when viewing in the Nadir direction). Swath width of PRISM is 70km when viewing in the Nadir direction, and 35km when in triplet mode.
The objective of the project was to create 3D stereomodels –by generating DTMs and Orthoimages-, digitize each plane in the mines and then compare digitizations and calculate the excavated volumes for each mine. Using the ERDAS LPS software, GCPs were assigned to both pictures of each stereomodel. The XY coordinates of each GCP were obtained by the WMS Server of the Greek Cadastre and then the heights were exported from 5m accuracy DTMs created by the Greek Cadastre as well. The same GCPs were used for the two stereomodels of each area in order to eliminate horizontal and vertical discrepancies. The coordinate system used was the Greek Grid or EGSA 1987 which has a six-digit integral X and seven-digit Y.
Each Cartosat model consisted of one pair of scenes, whereas each ALOS model consisted of 3 pairs. For the ALOS models only one pair was used as the other two didn't depict the open pit mines. A block file was created with the ERDAS LPS for each model with the two scenes. The two scenes have an over 30% overlapped area which is the minimum for the creation of the stereomodels. About 30-40 GCPs were selected for the overlapping area and 10-20 points for the not overlapping area. The GCP cloud was denser around the mines to achieve a lower RMS Error on both horizontal and vertical axis.

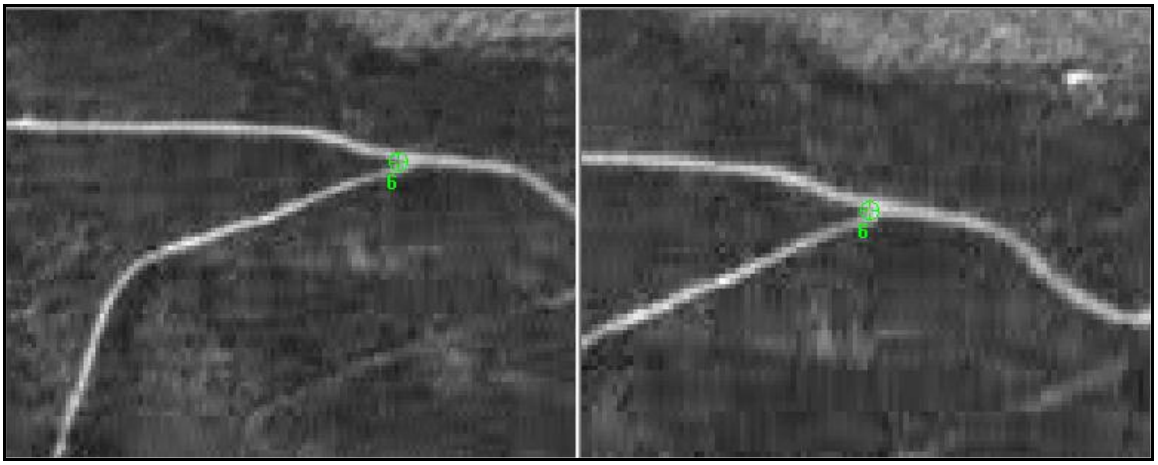

Figure 1: Example of a Ground Control Point from the ALOS stereo pair of the Markopoulo, Attiki Peninsula area.

After all the points were placed on the stereopairs, the next step was to perform Aerial Triangulation in order to calculate the RMS Error. A general rule is that the error should fluctuate in values less or equal to half the spatial resolution of the picture or half the pixel size. In this case

the errors should be less than 1.25m or 0.5 pixels. After some points were excluded from the triangulation and several corrections on the points' placement were done, the aerial triangulation error fell to under 1m or ≈0.4 pixels.
In order to lower the RMSE further, an ERDAS LPS feature was used, which automatically finds and places points on the scenes based on their visual similarity. It is called Automatic Tie Point Extraction. But even the fact that it is automatic, it doesn't mean that all the generated Tie Points are correct, so they all had to be checked one by one. So, the GCP cloud became denser, thus achieving better accuracy.
Continuing, after all the points were checked and was made sure that their placements and coordinates were correct, the DTMs were to be created. The DTMs were extracted using the Classic ATE method, and have 7.5m pixel size.
The next step was the Ortho Resampling and the accuracy test for each orthoimage. The orthoimages are created based on the DTMs and have, similarly to the satellite images, 2.5m pixel size. After they were created their accuracy was tested, using ArcMap, to assure that the geometric correction was performed properly. Several points with the best possible dispersion were selected, and their coordinates were compared to the coordinates from the Greek Cadastre WMS Server and it was proved that the orthoimages were very accurate inside a selected AOI which included the mines.
The final process was the digitization of the planes using ERDAS Stereo Analyst. It would be ideal to digitize the head and foot of each plane so as to assure that the plane height is the same for the two models and there is no digitization error. But for the Cartosat case it wasn't possible due to an almost vertical scene capturing of the mine area, so only the planes' head were digitized. The digitizations were saved to a shapefile which contained, amongst other attributes, the average height for each object. This attribute will help with the calculations for the excavated limestone volumes.

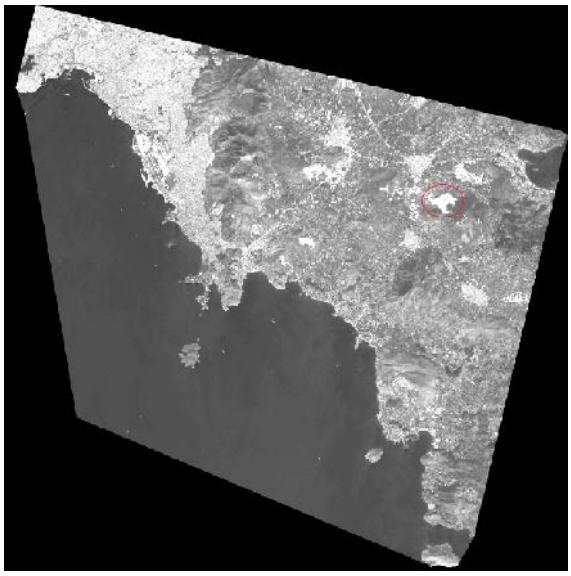

Figure 2: ALOS Orthoimage for the Markopoulo, Attiki case study. The red circle indicates the open-pit mine.

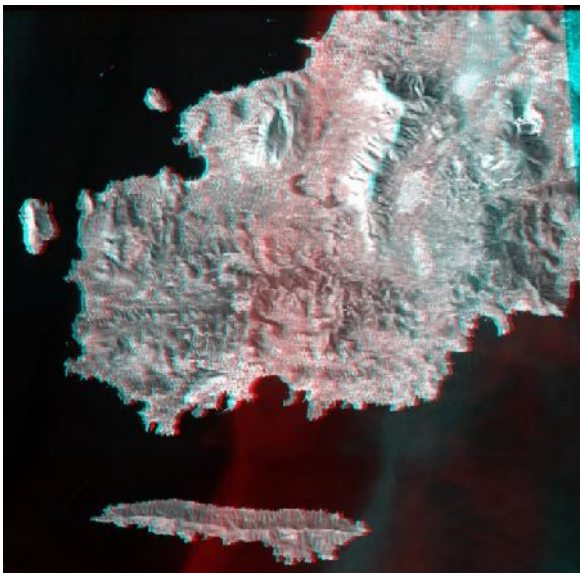

Figure 3: The Cartosat stereomodel for the Markopoulo open-pit limestone mine. The figure can be seen in 3D using Red & Green-Blue glasses.

After the two models of each case were digitized, they were loaded on ArcMap (Figure 5). Since the Cartosat imagery was captured on February 27th 2008 and the ALOS imagery on June 6th 2008, it is expected that some of the ALOS planes would subside horizontally, due to on-going excavation processes, compared to the Cartosat. The idea was to calculate the horizontal area between the Cartosat and the ALOS digitization and then multiply by the plane height to come up with the volume.

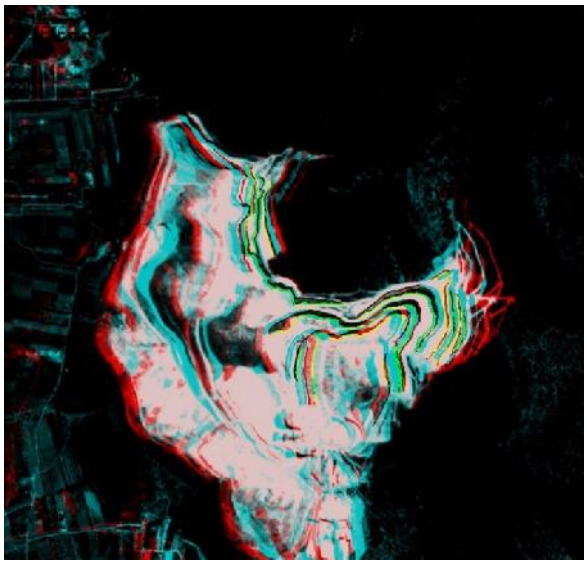

Figure 4: The ALOS stereomodel for the Markopoulo open-pit limestone mine. The black line shows the digitized head of the planes and the green shows the foot. The figure can be seen in 3D using Red & Green-Blue glasses.

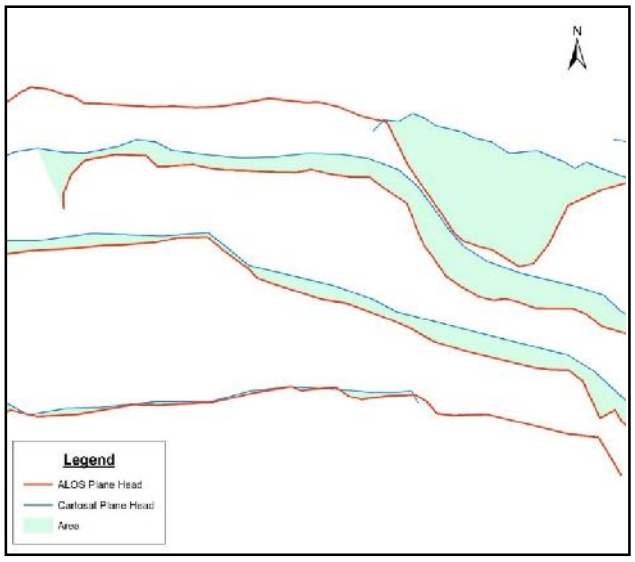

Figure 5: The comparison between the two digitizations for the Markopoulo, Attiki case study. The green polygons represent the excavated area.

CONCLUSIONS

Multitemporal and multisensor high resolution satellite stereo-data sets were used for quarry monitoring in two different location in Greece and the calculation of the excavation volumes for an almost 4 months period in one case. The satellite stereo-data can provide a very accurate, very cheap and very quick source of data for quarry monitoring.
Synergistic use of remote sensing data, photogrammetry and GIS seems to be the most appropriate solution for quarry monitoring and excavation volumes calculation.

REFERENCES

1) Rawat K.S., Mishra A.K., Sehgal V.K., Ahmed N., Tripathi V.K., “Comparative evaluation of horizontal accuracy of elevations of selected ground control points from ASTER and SRTM DEM with respect to CARTOSAT-1 DEM: a case study of Shahjahanpur district, Uttar Pradesh, India”, 2013, Geocarto International, 28 (5), pp. 439-452.

2) Koruyan K.,Deliormanli A.H., Karaca Z., Momayez M., Lu H., Yalçin E., “Remote sensing in management of mining land and proximate habitat”, 2012, Journal of the Southern African Institute of Mining and Metallurgy, 112 (7), pp. 667-672.

3) Schmidt H., Glaesser C., “Multitemporal analysis of satellite data and their use in the monitoring of the environmental impacts of open cast lignite mining areas in eastern Germany”, 1998, International Journal of Remote Sensing, 19 (12), pp. 2245-2260.

4) Chaminda S.P., Chen X., Kibe S., Lal S., “Assessment of DEM accuracy generated from ALOS PRISM high resolution stereo-optical imagery using LPS”, 2010, 31st Asian Conference on Remote Sensing 2010, ACRS 2010, 1, pp. 933-938.

5) Yue H., Liu G., Guo H., Li X., Kang Z., Wang R., Zhong X., “Coal mining induced land subsidence monitoring using multiband spaceborne differential interferometric synthetic aperture radar data”, 2011, Journal of Applied Remote Sensing, 5 (1), art. no. 053518.

6) Martha T., Kerle N., Jetten V., Westen C., Kumar K., “Landslide Volumetric Analysis Using Cartosat-1-Derived DEMs”, 2010, IEEE Geoscience and Remote Sensing Letters, 7 (3), pp. 1545-1549.

7) Tadono T., Takaku J., Shimada M., “Validation Study on ALOS PRISM DSM Mosaic and ASTER GDEM 2”, ISPRS Annals of the Photogrammetry, Remote Sensing and Spatial Information Sciences, Volume I-4, pp. 193-198.

8) Lehner M., Müller R., Reinartz P., “Stereo Evaluation of Cartosat-1 Data on Test Site 5 – First DLR Results”, 2008, CARTOSAT-1 Scientific Assessment Program – Commission IV

9) Pandey P., Venkataraman G., “Generation and Evaluation of Cartosat-1 DEM for Chhota Shigri Glacier, Himalaya”, 2012, International Journal of Geomatics and Geosciences, 2 (3), pp. 704-711.

10) Vivek K.S., Prashant K.C.R., Ayyeum P.T.J., “Orthorectification and Digital Elevation Model (DEM) Generation Using Cartosat-1 Satellite Stereo Pair in Himalayan Terrain”, 2010, Journal of Geographic Information System, 2010, 2, pp. 85-92.

11) Martha T.R., Kerle N., Jetten V., van Westen C.J., Kumar K.V., “Effect of Sun Elevation Angle on DSMs Derived from Cartosat-1 Data”, Photogrammetric Engineering & Remote Sensing, 76 (4), pp. 429-438.

12) Zhang X.-D., Ge D.-Q., Wu L.-X., Zhang L., Wang Y., Guo X.-F., Li M., Yu X.-H., “Study on monitoring land subsidence in mining city based on coherent target small-baseline InSAR”, 2012, Meitan Xuebao/Journal of the China Coal Society, 37 (10), pp. 1606-1611.

13) Liu Z.-G., Bian Z.-F., Lv F.-X., Dong B.-Q., “Subsidence monitoring caused by repeated excavation with time-series DInSAR”, 2013, Caikuang yu Anquan Gongcheng Xuebao/Journal of Mining and Safety Engineering, 30 (3), pp. 390-395.

14) Habib A., Labbasi K., Menenti M., Khoshelham K., “DEM Extraction from ALOS-PRISM data in the region of Sahel-Oualidia (Moroccan Atlantic coast)”, 2012, International Conference of GIS-Users, Taza GIS-Days, Proceeding Book, pp.96-99.

15) Tang F., Chen Z., Wu H., “Application of GPS/InSAR fusion technology in dynamic monitoring of mining subsidence in western mining areas”, 2012, 2nd International Conference on Consumer Electronics, Communications and Networks, CECNet 2012 - Proceedings, art. no. 6202159, pp. 2420-2423.

16) Wu H., Zhang Y., Zhong F., “Monitoring mine subsidence with time-series SAR interferometry”, 2012, Advanced Materials Research, 524-527, pp. 618-621.

HIGH RESOLUTION SPACE- AND AIR-BORNE IMAGERY PROVIDES INSIGHT INTOSLOPE HYDROLOGY AND INSTABILITY

Janusz Wasowski[1], Marina Dipalma Lagreca[2], Caterina Lamanna[3] and Guido Pasquariello[4]

1. National Research Council, CNR-IRPI, Bari, Italy; j.wasowski@ba.irpi.cnr.it
2. Dipartimento di Scienze della Terra e Geoambientali, Università degli Studi di Bari "Aldo Moro", Bari, Italy; m.dipalma@ba.irpi.cnr.it
3. c/o CNR-IRPI, Bari, Italy; cate.lama@tiscali.it
4. National Research Council, CNR-ISSIA, Bari, Italy; pasquariello@ba.issia.cnr.it

ABSTRACT

We usehigh resolution multispectral imagery focusing on water as a critical factor of the recurrent instability of poorly drained slopes in a 15.3 km^2 catchment area in the Apennine Mountains (Italy).The present work expands on our recent study that exploited IKONOS-2 imagery of April 2006 for mapping active landslides, investigating their association with seasonally wet zones (areas covered by free surface-water including ponds, migrating surface-water, seeps), and for inferring surface-subsurface water relationships in unstable slopes. We use 0.5 m resolution multispectral orthophotos acquired in March 2011 to map the distributions of active landslides and wet zones. While the former are mapped via visual interpretation of the imagery, the latter are first identified using supervised classification and two commercial remote sensing software, and then cross-checked via visual interpretation. The comparison of the results indicates that semi-automatic methods can assist in mapping wet areas, but controlsvia visual analysis along with a good knowledge of local slopeconditions are necessary to extract reliable information.A comparative analysis of 2011 and 2006 inventories demonstrates significant recurrence of active landslides and wet areas, as well as their close spatial associations. This represents important input for temporal and spatial landslide hazard assessments. Thus it is suggestedthat high resolution multispectral space- and air-borne imagery should be more often exploited in landslide investigations.

INTRODUCTION

Remotely sensed data are typically used for landslide detection and mapping, and ultimately for generating digital landslide inventories(1,2). Our review of recent literature on landslides (3 and references therein) indicates that only few slope instability investigations attempted to use high resolution multispectral imagery to estimate moisture or water content of ground surface materials. The main purpose of this work is to show that,if such imagery is acquiredtowards the end of the wet season (higher groundwater levels and susceptibility to landsliding), it can provide useful information about surface-water conditions on slopes and thus be better exploited in landslide studies. We also test the applicability of supervised classification methods, available through commercial software, for semi-automatic identification and mapping of wet areas on slopes.

This work builds up on our recent studies that exploited IKONOS-2 imagery of early spring 2006 for mapping active landslides, investigating their association with seasonally wet zones (areas covered by free surface-water including ponds, migrating surface-water, seeps), and for inferring surface-subsurface water relationships in unstable slopes (3,4). In particular, for comparative reasons we exploit another set of data, i.e. sub-meter resolution multispectral orthophotos acquired over the same study area in late winter of 2011 to map the distributions of active landslides and wet zones, and to investigate their associations.

The study area is located in the southern portion of the Apennine Mountains (southern Italy), called the Daunia Apennines and known for recurrent slope instability problems (3,4). We consider a 15.3 km^2 catchment area traversed by a mid-slope road, which is now closed to traffic because of

landslide damage (Fig. 1).The area has moderate relief topography, with elevations below 800 m and modest slope inclinations (~10° on average). The climate is Mediterranean subhumid (sub-Apennine) with annual rainfall values from 400 to nearly 1000 mm. The predominance of clays with weak geotechnical properties and poorly drained slopes are the main causes of landsliding (3,4).

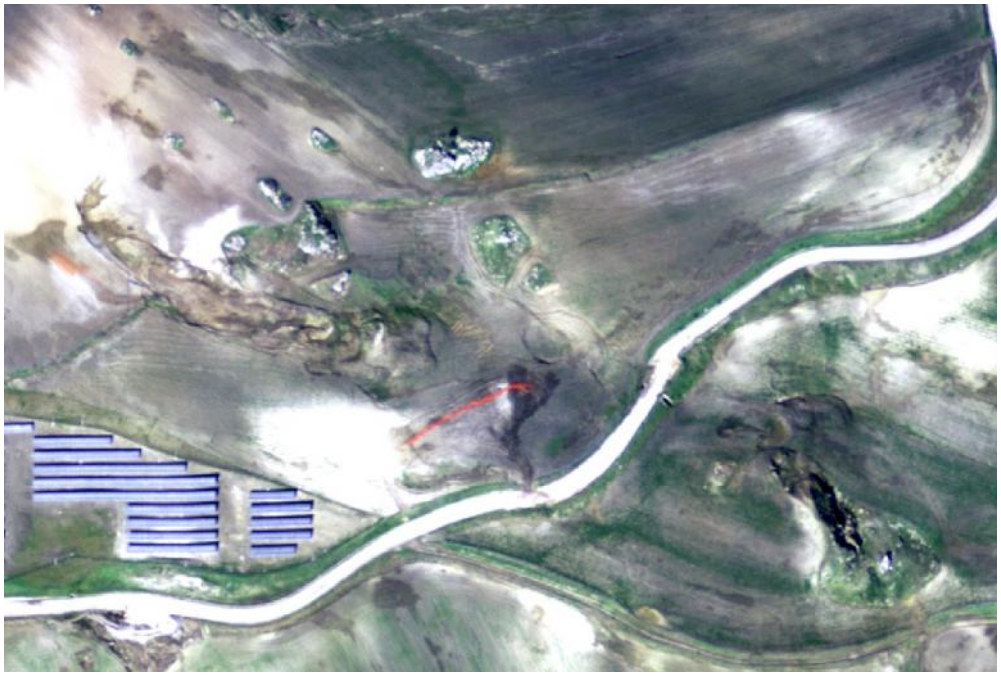

Figure 1 : Orthophoto from March 2011 showing an example of about 100 m wide and few hundred meters long road-damaging landslide that extends from upper left to lower right corner of the image; associated wet areas can be recognized through the tonal differences (darker tones).

MATERIALS AND METHODS

The imagery and spatial information used in the present work included:

- IKONOS-2 multispectral imagery acquired in April 2006

- 0.5 m resolution multispectral orthophotos acquired in March 2011

- Inventory maps of 30 landslides that in 2003-2005 damaged the road in the catchment and of landslides active in 2006 (from 3,4)

- Digital Elevation Model (DEM) derived from 1:5000 scale topographic map (from 2002)

- Inventory of wet areas in 2006 based on visual (on-screen) interpretation of IKONOS-2 imagery (from 3,4)

In addition, we compiled inventories of wet areas and active landslides (in March 2011)via visual interpretation of the orthophotos. Furthermore, using ERDAS7.09 and ENVI6.12 software and supervised classification methods, we compiled maps of wet areas in 2006 and 2011. The spatial datasets were collated and analyzed using ArcGIS10.1 software.

RESULTS

Figure 2shows the outcomes of supervised classifications of 2011 orthophotosaimed at detecting wet areas. The comparisonof the results obtained using ERDAS and ENVI indicates similar

distributions and percentages of wet areasin the catchment (respectively 7.1 and 6.1%). Figure 2 also shows close associations between some of the road-damaging landslides, identified in the field in 2005 and re-mapped using 2006 IKONOS-2 imagery, and the wet areas.

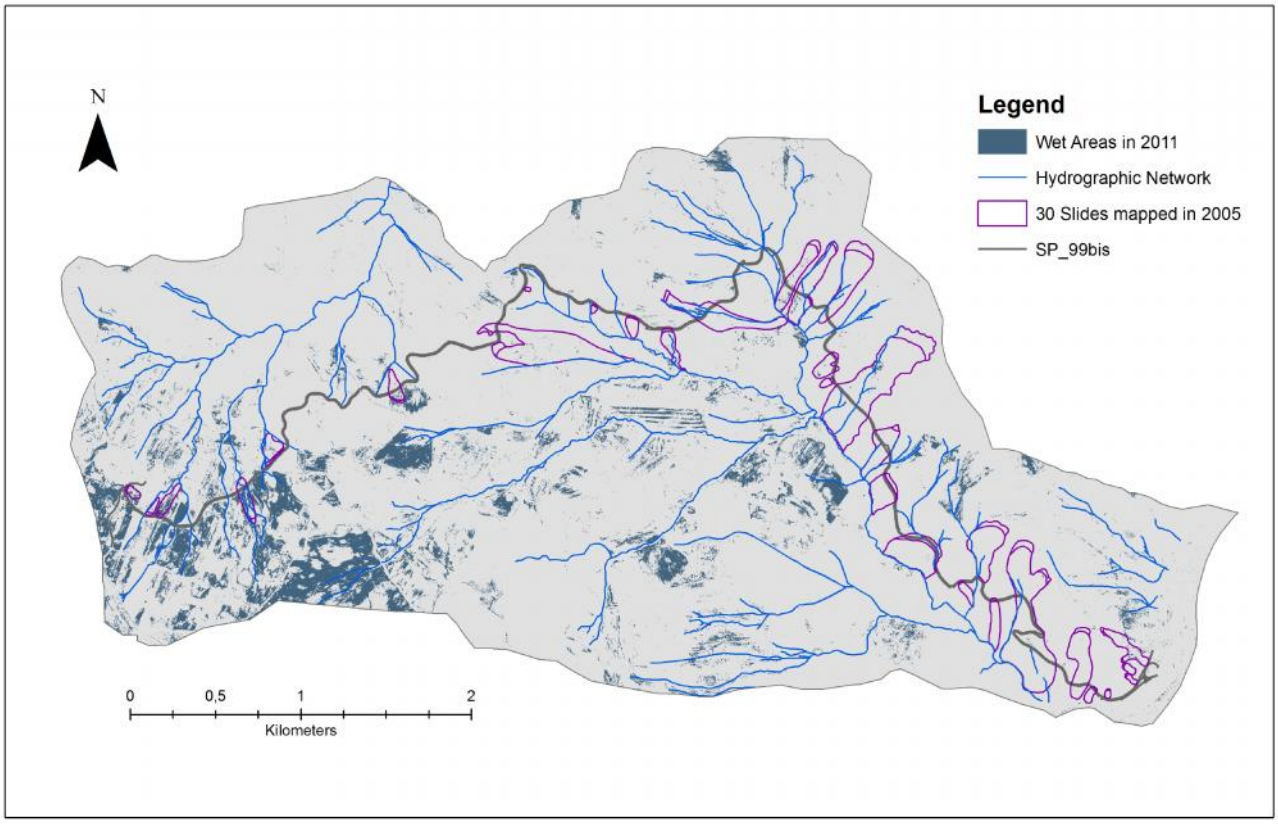

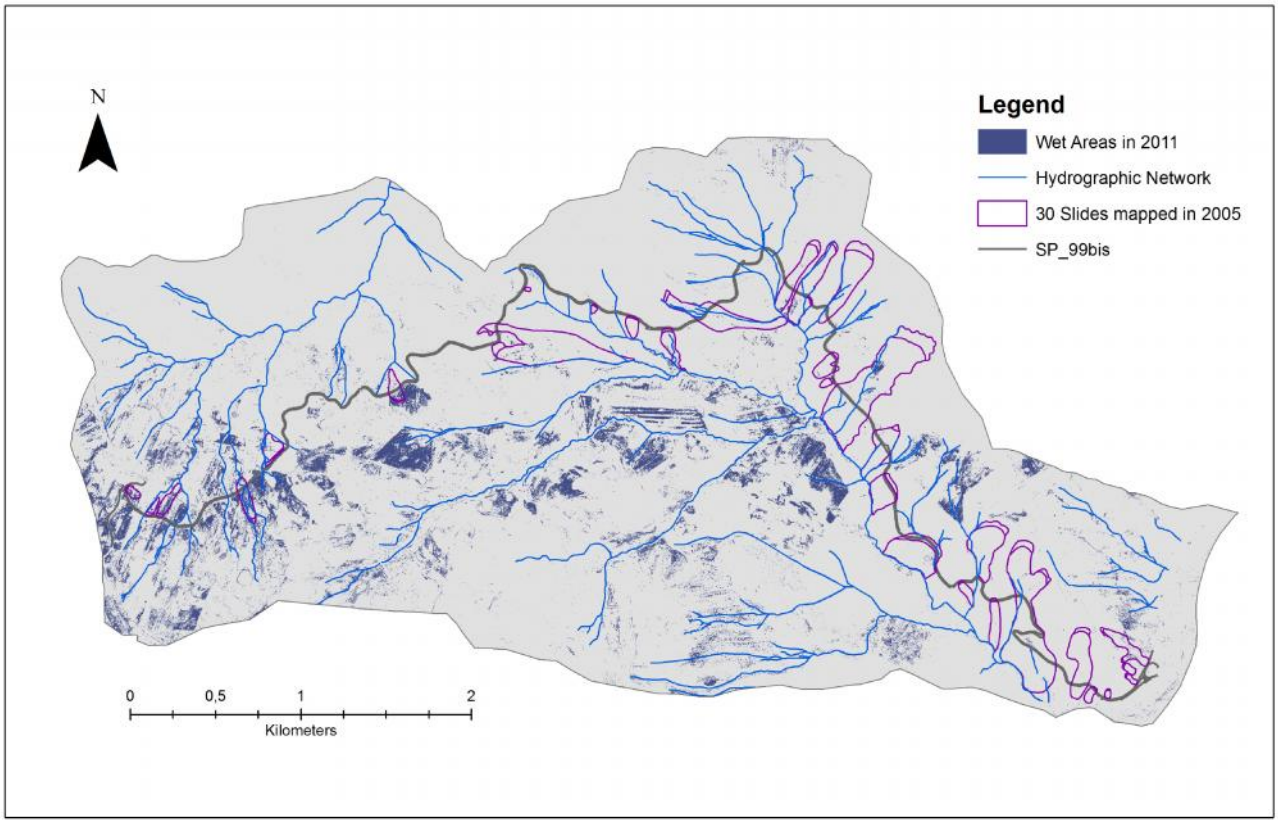

Figure 2: Distribution of wet areas on 11 March 2011 from supervised classification of 0.5 m resolution multispectral orthophoto using ERDAS (Upper figure) and ENVI (Lower figure) software. Note also 30 road-damaging landslides; SP_99bis = name of the road.

We also performed visual interpretation of 2011 orthophotos to compile a map of wet areas for a 5.6 km^2portion of the catchment centred around the road (Fig. 3). The intentionwas to provide an additional check of the results obtained via supervised classification (using ENVI software).

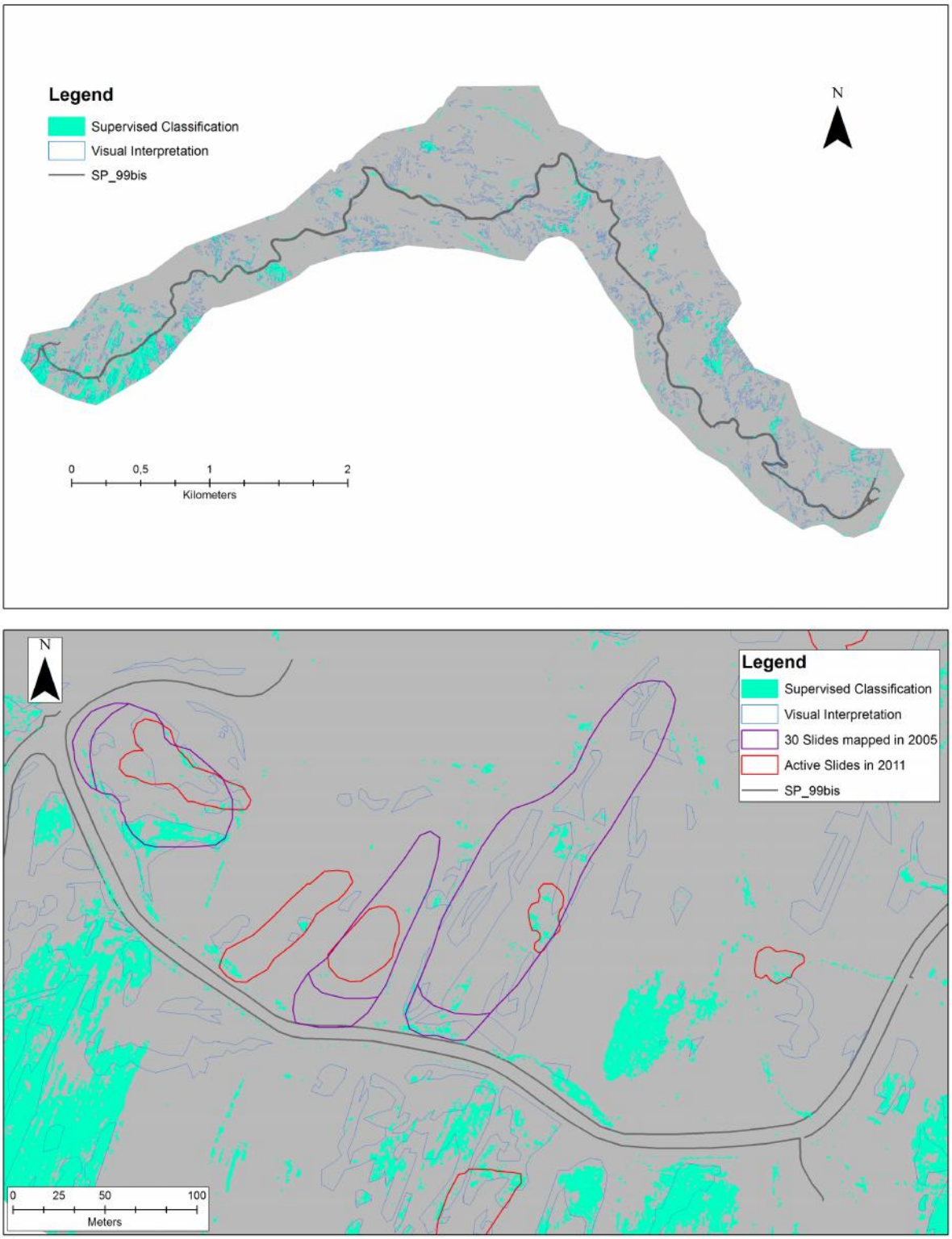

Figure 3:(Upper) Distributions of wet areas in March 2011 on slopes traversed by SP_99bis road,from supervised classification and from visual interpretation;(Lower) Close-up of the western-most part of the Upper figure showing also major 2005 landslides and landslides active in 2011.

The comparisonof the distributions of wet areas obtained from supervised classification and visual interpretation shows that there are significant differences, especially at a local scale (Fig. 3).

Nevertheless, in many cases there is considerable overlap of the wet areas. Furthermore, a persistent association of wet areas and unstable slope portions can be indicated by consideringthe distributions of 2005 landslides and landslides active in 2011.

We also attempted to quantify the degree of overlap between the wet areas identified via supervised classification and those obtained from visual interpretation. The results show that over 50% of the wet areas classified semi-automatically fall within the wet areas mapped via visual interpretation (Fig. 4). Furthermore, a close association can be indicated for an additional ~35% by considering a 10 m wide buffers around the visually interpreted wet zones.

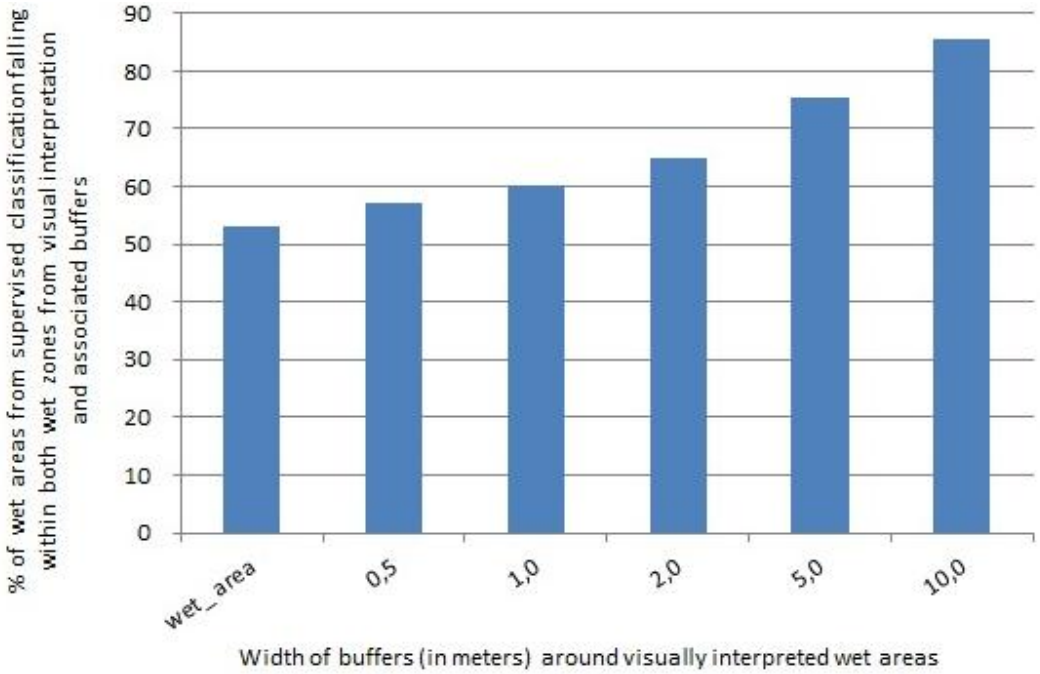

Figure 4: Diagram based on the intersection of wet areas obtained from supervised classification (using ENVI) and from visual interpretation of March 2011 orthophoto. Over 85% of classified wet areas can be associated with the visually recognized wet areas by adding10 m wide buffers.

Furthermore, we examined the spatial recurrence of wet slope conditions in late winter-early spring period using intersection of the results obtained from visual interpretation of 2006 IKONOS-2imagery and supervised classification of 2011 orthophoto. At the catchment scale it would appear that a spatio-temporal recurrence, i.e. the repeated presence of wet areas in the exactly the same locations, is limited (Fig. 5). Nevertheless, locally there is a considerable overlap of the wet areas, i.e. surface-water or wet ground conditions are recognized on the same slope portions on both 2006 and 2011 imagery.

Finally, a simple overlay of three temporally distinctive landslide inventories (from 2003-2005, 2006 and 2011) and the 2006-2011 wet area intersection shows once again that some slopes with recurrent landslide activity are closely associated with seasonally persistent wet ground conditions (Fig. 5). For example, this is evident in the western-most portion of the studied catchment, especially when examined on a local scale. Indeed, as previously shown through an extensive borehole piezometer investigation (2), a number of remotely sensed wet zones are indicative of sites with seasonally persistent very high groundwater levels within landslide-prone slopes and on intermittently active landslides.

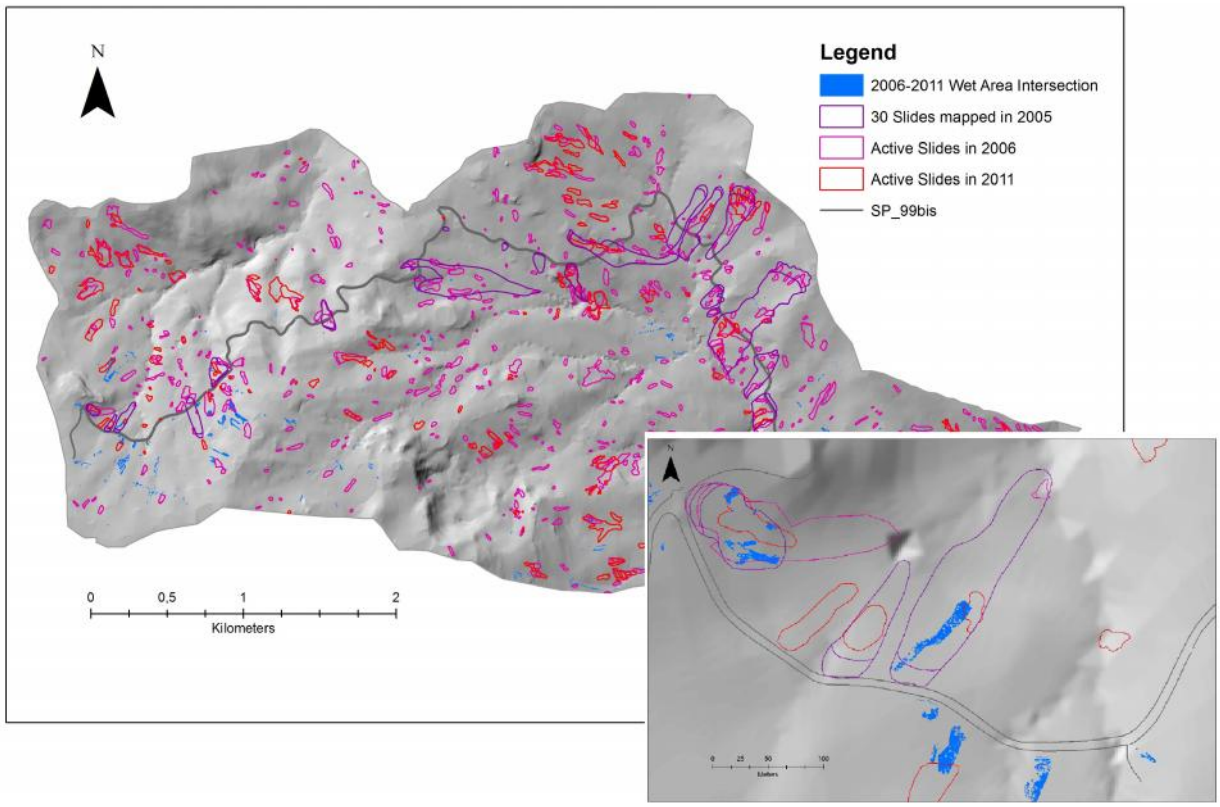

Figure 5: Distribution of recurrently wet areas based on intersection of 2006 (IKONOS-2) and 2011 (orthophoto) results obtained, respectively, from visual interpretation and supervised classification. Close-up of the western-most portion of the larger figure highlights associations of wet zones withroad-damaging landslides imapped in 2005 and landslides active in 2006 and 2011.

CONCLUSIONS

The results of our case study suggest that high resolution multispectral space- and air-borne imagery can be used not only for compiling landslide inventories, but also provide valuable insight into slope instability processes by assisting in the identification of seasonally recurrent wet areas on slopes susceptible to instability. However, further efforts are needed to test performance of semi-automatic classification of wet areas in different settings. The present work indicates that useful information about surface-water conditions can be obtained in settings with shallow slope topography, clay-rich lithology and land use/land cover dominated by agricultural soils (with little woodland).

REFERENCES

1 Van Westen, C J, E Castellanos & S L Kuriakose, 2008. Spatial data for landslide susceptibility, hazard, and vulnerability assessment: An overview. Engineering Geology, 102: 112–131

2 Guzzetti, F, A C Mondini, M Cardinali, F Fiorucci, M Santangelo &K-T Chang, 2012. Landslide inventory maps: new tools for an old problem. Earth-Science Reviews,112: 1–25

3 Wasowski J, C Lamanna, G Gigante & D Casarano, 2012. High resolution satellite imagery analysis for inferring surface-subsurface water relationships in unstable slopes. Remote Sensing of Environment, 124: 135-148 doi: 10.1016/j.rse.2012.05.007

4 Wasowski J, C Lamanna & D Casarano, 2010. Mapping mid-slope road landslides and instability factors with high resolution satellite imagery. In: Proceeding of the IAEG 11th Congress - Geologically Active, edited by Williams et al. (Auckland, New Zealand), 2563–2570

SURFACE DISPLACEMENTS OF THE 2014 CEPHALONIA (GREECE) EARTHQUAKE USING HIGH RESOLUTION SAR INTERFEROMETRY

George Benekos[1], Konstantinos Derdelakos[1], Christos Bountzouklis[1] and Penelope Kourkouli [2,3]

1. Harokopio University of Athens, Department of Geography, El. Venizelou 70 Kallithea, 17671 Athens, Greece ;benekos@hua.gr ;gs20953@hua.gr ; gem14cbo@student.lu.se
2. GAMMA Remote Sensing, Worbstrasse 225, CH-3073, GümligenSwitzerland; kourkouli@gamma-rs.ch
3. University of Leicester, Department of Geography, University Road, Leicester, LE1 7RH, UK

ABSTRACT

The island of Cephalonia, Western Greece, was struck by two strong seismic events, with magnitudes, ML= 5.8 and ML = 5.7 which occurred on Jan. 26, 2014 and Feb. 3, 2014 respectively. The first event was located near Argostoli's town, whereas the second one was located at the north part of Livadi village. These two strong earthquake events followed by smaller aftershocks provoking extensive crustal movements and structural damage effects. Differential Synthetic Aperture Radar Interferometry (DInSAR) is a powerful remote sensing tool for ground motion monitoring. The last two decades, DInSAR is widely applied to a variety of applications including natural hazards such as earthquakes. In 2007, a high resolution X-band satellite namely TerraSAR-X was launched. Due to its short revisit cycle of 11 days and its short wavelength, there is a good potential to capture faster surface movements. This study refers to the application of the DInSAR using TerraSAR-X strip map data to monitor the co- and post-seismic surface deformation caused by the second earthquake event. Hence, based on the interferometric processing of multiple scenes, several differential interferograms calculated showing the deformation patterns which caused before and after the seismic event. First results show that the main part of the island shows stability or a small uplift whereas the western part shows a significant deformation pattern. Those results permit to identify the local tectonic setting of the study area and investigate the reasons that some of settlements affected more

INTRODUCTION

On January 26 and February 3, 2014, two strong seismic events took place in the island of Cephalonia at a shallow depth causing catastrophic consequences in the western region of the island. According to NOA (National Observatory of Athens) those events were measured at 5.8 and 5.7 ML respectively (Figure 1). Cephalonia Island is located in western Greece which is the area of interaction between the African and the Eurasian lithospheres. Eastern Mediterranean lithosphere, which is the front part of the oceanic-like African lithosphere, is subducted beneath the Aegean continental lithosphere, which is the front part of the Eurasian lithosphere, along the Hellenic Arc – Trench system (1)(Le Pichon&Angelier, 1979). Four major tectonic blocks can be distinguished on the island, based on lithology, on similar structure features and on a common evolution during the upper Quaternary: (a) the Erissos peninsula block (northern part of the island); (b) the Paliki peninsula block (western part of the island); (c) the Ainos block (central and eastern part of the island); (d) the Argostoli block (southwestern part of the island). Each of these major blocks consists of several subordinate units and is flanked by a major thrust fault. The seismicity of the area, has been analysed by Kokinou et al. (2006) (2), gathering focal mechanisms of M>5 earthquakes that occured between 1972 and 2003. Also several authors (e.g. Scordilis et al. 1985; Kiratzi& Langston 1991) (3,4) studied the major event of of January 17, 1983 (Ms=7.0) and its aftershocks.To the latter family are more likely to belong the MS=7.2 earthquake of 1953 (5) and the Ms= 5.8 of 2002 (6)and to the former, the MS=6.3 earthquake of 1972 (7), the MS=7.0 of 1983

(8) and those of 2014. A dextral fault with small reverse component, striking NNE-SSW, was the cause of the recent seismic activity event of January/February as shown by the preliminary focal mechanisms of the main shock. An area covering the entire extent of Paliki Peninsula has been indicated by the distribution of aftershocks, whereas preliminary focal mechanism analysis shows that they have been caused by both dextral and reverse faults, striking approximately NNE-SSW and NW-SE respectively. Factors like the epicentral depth of the main shock and the aftershocks (up to 15 km), the geometrical characteristics (strike and dip angle) of the planes in the preliminary focal mechanisms, as well as their deformation pattern show that this earthquake sequence can be interpreted as an activation of a transpressional bend of the CFZ with no expression of the causative fault on land, considering the proximity of the area to the CFT. Uplift and bending of the overlying Eocene to Miocene sediments, has been caused by this transpressional bend that is expressed as a series of blind thrust faults (9).

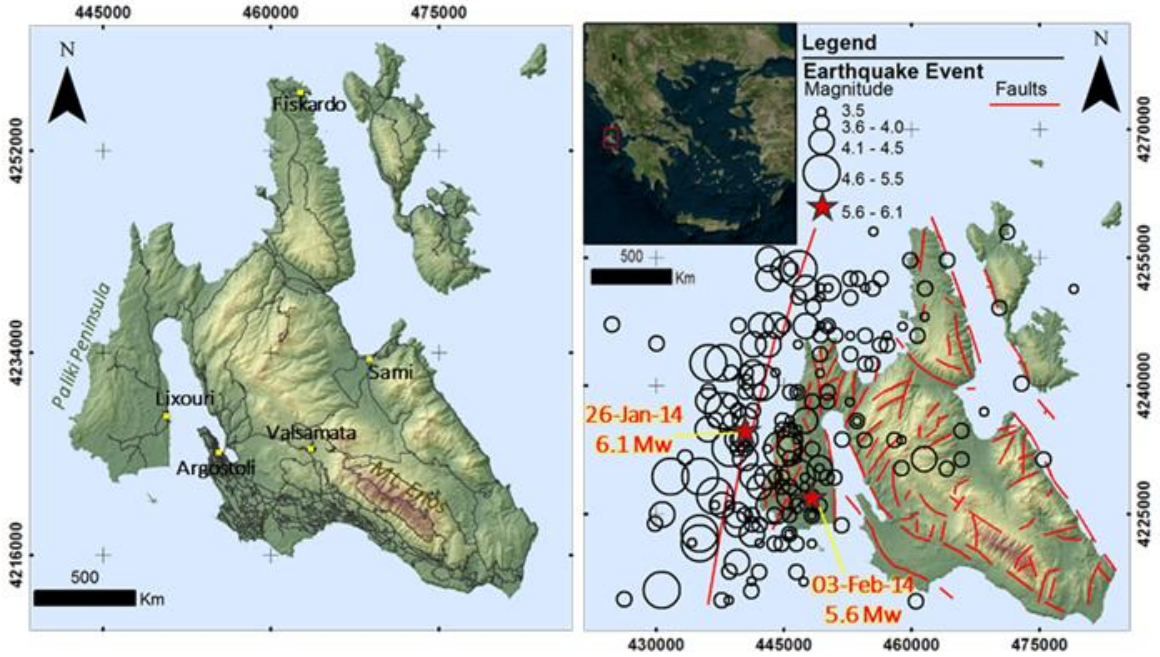

Figure 1: Location map of the Cephalonia Island (left pane) and the seismological map (right pane) (Source: European - Mediterranean Seismological Center).

Differential Synthetic Aperture Radar Interferometry (DInSAR) technique has been widely used to identify ground deformation caused by different natural and anthropogenic phenomena. Many scientists are motivated by the potential of SAR interferometry to be applied for a wide range of applications related to seismotectonics (10,11). The utilization of an appropriate interferometric dataset allows measuring the various components of the seismic cycle, namely the pre-seismic, co-seismic, and post-seismic deformation (12, 13, 14, 15, 16, 17). The aim of this study is to measure the ground motion, which caused by the two latest strong seismic events in Cephalonia Island, using the DInSAR method. Three high resolution StripMap scenes acquired from TerraSAR-X satellite are used. DInSAR is applied and three differential interferograms were calculated showing the displacement of both co-seismic and post-seismic periods. Results indicate the seismic behavior in the area of interest and further analysis demonstrates the reason that some areas had suffered more damages in contrast to other parts of the island.

DATA & METHODOLOGY

We analyzed the induced deformation field by exploiting SAR scenes acquired from the TerraSAR-X (X-band) satellite. The scenes acquired in StripMap mode with a high resolution of about 3 m and with small temporal baseline (repeat cycle 11 days). In order to monitor the deformation which caused due to the seismic events, three Single Look Complex (SLC) ascending scenes with

acquisition dates 28/01/2014, 08/02/2014 and 19/02/2014, were selected. In addition, a Digital Elevation Model (DEM) with a very high resolution of 5 m per pixel and a vertical accuracy better than 5 m, was used. The analysis has been done using the GAMMA software.

The first step of the interferometric processing was the coregistration of the images in order to obtain the same geometry. The three images coregistered using as master the scene with date 28/01/2014. Additionally, the 5 m DEM was used and its heights transformed in SAR geometry in order to introduce them in the SLC coregistration. After a refinement step, we estimated the offsets between the datasets showing low standard deviations below 0.05 pixel. Afterwards, a total number of three differential interferograms were estimated, two for the co-seismic period and one for the post-seismic. The differential interferometric pairs are shown in Table 1. Firstly, the initial differential interferograms were estimated. The topographic phase component has been removed from each interferogram using a very high resolution Digital Elevation Model (DEM). These flattered interferograms were filtered using an adaptive Goldstein noise filter with a small size window (12×12 pixel) and then the unwrapping procedure was followed using the Minimum Cost Flow (MCF) algorithm (18) and a qualitative coherence threshold (γ>0.3). Additionally, a baseline refinement was performed in order to further improve the baseline estimation and consequently mitigate the errors. Finally, a 5×5 multi-looking in range and azimuth was applied which corresponds to about 15 m × 15 m pixel size on the ground.

Table 1: Differential Interferometric Pairs and their Baseline Spatio-temporal Characteristics

	No.	Differential Interferometric Pairs	Spatial Baseline (m)	Temporal Baseline (days)
Co-seismic	A	28/01/2014 - 08/02/2014	108	11
	B	28/01/2014 - 19/02/2014	170	22
Post-seismic	C	08/02/2014 - 19/02/2014	62	11

RESULTS

The estimated interferograms were introduced in a GIS environment in order to analyze the spatiotemporal displacement which caused by the seismic event (Figure 2). It is evident that the Cephalonia Island has been affected from the seismic event. Particularly, the two co-seismic interferograms (A & B) show that the western area of the island has been influenced the most from the earthquake. In the central-south part of Paliki peninsula, these interferograms demonstrate a maximum motion of ~+12 cm in the line of sight (LOS) direction towards the satellite sensor whereas in the north and east part of the peninsula a maximum LOS motion of ~-7 cm away from the satellite is observed.

The comparison of the co-seismic results show an interesting finding. In contrast with the first interferogram, the second one shows a diminution at the uplifted area and an increase of subsidence at the east coast and north part of Paliki's peninsula.Specifically, in the first co-seismic pair is observed an uplift motion between +6 cm and +12 cm whereas in the second co-seismic pair with the longer temporal baseline the uplift motion decreased from +6 cm to +2 cm.

On the east coast part the coseismic (A) revales a subsidences from - 5.5cm to -1cm and at the coseismic (B) the observed motion moved southern at Lixouri Village an increased between -7cm to -1cm. The same deformation pattern identified at the north part of Paliki's peninsula, the (A) coseismic deformation map showing values from -4cm to -2cm and the (B) coseismic increased to -7.5 to -2 cm. The post-seismic (C) deformation map covering the period 08/02/2014 - 19/02/2014 and illustrates stability. That reveals that after the two strong seismic events and the followed aftershocks, the Cephalonia Island and mainly the center-south of Paliki peninsula shows low displacement rates.

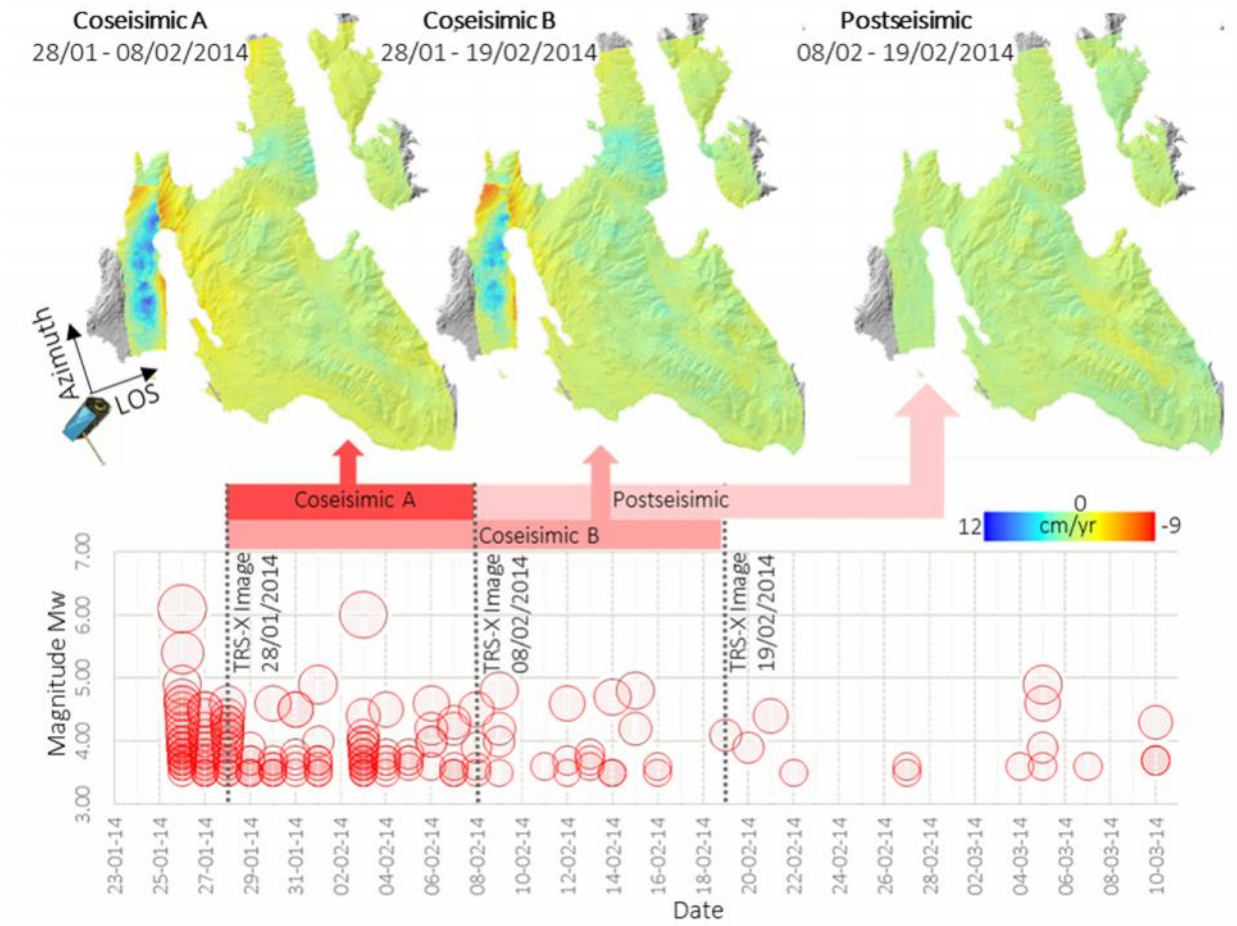

Figure 2: Three Differential Interferometric Pairs (two coseismic and one postseismic). On the bottom is presented the seismic sequence (Source: European - Mediterranean Seismological Center) Coseismic A period is illustrated with an intense red color, the Coseismic B with a less intense red color and with the pink is presented the postseismic period.

CONCLUSIONS

In this study, we have applied a DInSAR technique and we detect crustal movements due to a major earthquake event. The method was applied using three temporal TSX images covering the Cephalonia Island before and after the 3 Feb.2014 Cephalonia's earthquake. With high resolution data we managed to measure a wide area with a high spatial density of deformation trend measurements mapping the seismic crustal movements

ACKNOWLEDGEMENTS

The authors would like to thank Christian Minet for the TerraSAR-X data from Deutsches Zentrum für Luft- und Raumfahrt (DLR) and Associate Professor Issac Parcharidis for the for the organization of the research process. Especially we would like to thank the PhDcandidate Penelope Kourkouli for the significanthelp at the processing chain and for the helpful advices for the paper's writing. The seismic events were retrieved from European - Mediterranean Seismological Center.

REFERENCES

1 Le Pichon, X., Chamot-Rooke, N., Lallemant, S., Noomen, R., Veis, G., 1995. Geodetic determination of the kinematics of Central Greece with respect to Europe: implications for Eastern Mediterranean tectonics. Journal of Geophysical Research 100 (12), 675–690.

2 Kokinou, E., Papadimitriou, E., Karakostas, V., Kamberis, E. & Vallianatos, F., 2006. The Cephalonia Transform Zone (offshore Western Greece) with special emphasis to its prolongation towards the Ionian Abyssal Plain, Mar. Geophys. Res., doi:10.1007/s11001- 006-9005-2.

3 Scordilis, E.M., Karakaisis, G.F., Karakostas, B.G., Panagiotopoulos, D.G., Comninakis, P.E. & Papazachos, B.C., 1985. Evidence for transform faulting in the Ionian sea – The Cephalonia island earthquake sequence of 1983, Pure App. Geophys., 123(3), 388-397 , doi:10.1007/BF00880738.

4 Kiratzi, A.A. & Langston, C.A., 1991. Moment tensor inversion of the 1983 January 17 Kefallinia event of Ionian islands (Greece), Geophys. J. Int., 105(2), 529-535, doi: 10.1111/j.1365-246X.1991.tb06731.x.

5 Stiros, S.C., Pirazzoli, P.A., Laborel, J. &Laborel-Deguen F., 1994. The 1953 Earthquake in Cephalonia (Western Hellenic Arc): coastal uplift and halotectonic faulting, Geophys. J. Int., 117, 834-849.

6 Tselentis, G.-A., Melis, N.S., Sokos, E. & Beltas, P., 1997. The winter 1991-1992 earthquake sequence at Cephalonia island, western Greece, Pure Appl. Geophys., 150, 75-89.

7 Papadimitriou, E. E., 1993. Focal mechanism along the convex side of the Hellenic Arc and its tectonic significance, Boll. Geof. Teor. App., 35, 401–426.

8 Scordilis, E.M., Karakaisis, G.F., Karakostas, B.G., Panagiotopoulos, D.G., Comninakis, P.E. & Papazachos, B.C., 1985. Evidence for transform faulting in the Ionian sea – The Cephalonia island earthquake sequence of 1983, Pure App. Geophys., 123(3), 388-397 , doi:10.1007/BF00880738.

9 Alexandros Chatzipetros, Sotiris Sboras, Spyros Pavlides, 2014. The Cephalonia (Greece) January 26, 2014 M6.1 earthquake: preliminary interpretation and stress transfer analysis, Geophysical Research Abstracts Vol. 16, EGU2014-16820

10 Massonnet, D. and Feigl K.L., 1998, Radar interferometry and its application to changes in theearth's surface. Reviews of Geophysics, 36(4), 441-500.

11 Zebker, H.A., Rosen, P.A., Goldstein, R.M., Gabriel, A. and Werner, C.L. 1994. On the derivation of coseismic displacement fields using differential radar interferometry: The Landers earthquake. Journal of Geophysical Research 99: doi: 10.1029/94JB01179. issn: 0148-0227.

12 Strozzi, T., Wegmu¨ller, U., Tosi, L., Bitelli, G., and Spreckels, V., 2001, Land subsidence monitoring with differential SAR interferometry. Photogrammetric Engineering and Remote Sensing, 67(11), 1261–1270.

13 Donnellan, A., Parker, Peltzer, G., 2002. Combined GPS and InSAR models of postseismic deformation from the Northridge earthquake. Pure and Applied Geophysics 159, 2261–2270.

14 Prati, C., Ferretti, A., &Perissin, D. 2010. Recent advances on surface deformation measurement by means of repeated space-borne SAR observations. Journal of Geodynamics, 49 pp. 161-170

15 Yague-martinez N, Eineder M, Cong X, Minet C.: Ground Displacement Measurement by TerraSAR-X Image Correlation: The 2011 Tohoku-Oki Earthquake. IEEE Geoscience and Remote Sensing Letters. 2012;9(4):539–543.

16 T. Frontera, A. Concha, P. Blanco, A. Echeverria, X. Goula, R. Arbiol, G. Khazaradze, F. Pérez, E. Suriñach, 2012, DInSARcoseismic deformation of the May 2011 Mw 5.1 Lorca earthquake, (Southern Spain), Solid Earth 01/2012; 3:111-119. DOI:10.5194/se-3-111-2012

17 Liu, W., and F. Yamazaki, 2013,Detection of crustal movement from TerraSAR-X intensity image, IEEE Geoscience and Remote sensing Letters, Vol. 10, No. 1, pp. 199–203, 2013.

18 Constantini, M., 1998. A novel phase unwrapping method based on network programming. IEEE Transactions on Geoscience and Remote Sensing 36 (3), 813–821.

APPRAISAL OF THE DAMAGES CAUSED BY THE 12TH JANUARY 2010 HAITI EARTHQUAKE BY ASTER MULTITEMPORAL IMAGERY ANALYSIS

Kanakaki Stavroula [1], Parcharidis Issaak [1] and Poscolieri Maurizio[2]

1. Dept. of Geography, Harokopio University of Athens, El. Venizelou 70, Athens 17671, Greece, phone: +30 2109549345; e-mail: parchar@hua.gr, stavroula_argiro@hotmail.com
2. CNR - Institute of Acoustics and Sensor "O.M. Corbino", Via Fosso del Cavaliere 100, 00185 Rome, Italy; phone: +39 06 49934110; e-mail: maurizio.poscolieri@idasc.cnr.it

ABSTRACT

A strong earthquake of 7.0 Mw magnitude struck on January 12th 2010 Haiti, causing serious damages to most of its capital, Port-au-Prince, and neighbouring areas.

Enriquillo-Plantain Garden fault is the main fault system that contributed to the 12th January earthquake. It is a prominent strike-slip fault being the result of the relative movement between Caribbean and North-American crustal plates.

This paper studies the impacts of Haiti earthquake on natural and human environments, using satellite imagery acquired before and after the earthquake. In particular, ASTER multispectral data sets were employed, aiming at pinpointing the damages caused by the strong seismic event.

The analyzed scenes, acquired before and after the earthquake, cover two different areas, the Haiti capital, Port-au-Prince, and the Miragoane lake region, located west of the capital. The analyzed ASTER bands are the visible and near-infrared (VNIR), as well as the thermal bands (TIR), including the backward looking NIR ones.

The application of various remote sensing techniques to the ASTER multitemporal imagery pointed out severe damages across the capital, consisting mostly of destroyed buildings, and nearby coastline regions, while, as regards the Miragoane region, severe alterations of lake coastline were identified. However, extended cloud coverage in both study areas was present, preventing sometimes suitable results.

INTRODUCTION

On January 12th 2010, 4.53 p.m. local time, a really strong earthquake of a 7.0 Mw magnitude hit the Haiti island causing major material damages and much human loss. Haiti is a Caribbean country that shares the Ispaniola island with Dominican Republic on the western side of the island, covering one third of it.

The Enriquillo-Plantain Garden (EPG) fault is the main fault system that contributed to the catastrophic earthquake. It is a prominent strike-slip fault being the result of the relative movement between Caribbean and North-American crustal plates. The quake epicentre was about 25 km (USGS) west of the country capital centre, Port-au-Prince, causing serious damages to all surrounding areas such as Carrefour, Petit and Grand Goâve.

The state apparatus was unable to respond to this event and face it promptly; thus, many foreign forces rushed to help in many ways. There were many dead, seriously injured and homeless people, while major drugs and food shortages occurred.

Different studies were carried to apply Remote Sensing methods for detecting areas

damaged by the 2010 earthquake (1,2). Satellite data offer a direct and quick way to extract useful information about the earthquake impacts. There are plenty of satellite data that can be used like the optical and the radar systems. Optical data of a high spatial resolution can give satisfying information about areas like the residential ones that faced more serious damages.

This case study used various relevant methods in order to examine the Haiti earthquake impacts on natural and human environment, using as input high resolution optical satellite data and comparing techniques and results with one another in terms of damage assessment. The analyzed satellite data are ASTER multispectral bands which do not exhibit a very high spatial resolution (about 15 m), meaning that they don't reach the 1 m or less spatial resolution of VHR sensors, such as Quickbird, Ikonos, Wordview and others do, but are quite good for attempting a first serious damage evaluation.

DATA

The analyzed imagery consists of ASTER (*Advanced Spaceborne Thermal Emission and Reflection Radiometer*) "*L1B Registered Radiance at the Sensor V003*" data set covering two different areas, the Haiti capital, Port-au-Prince, and the Miragoane lake region, located west of the capital, on the south side of the island. The analyzed ASTER bands are the visible and near-infrared (VNIR) with 15 meters ground resolution, as well as the thermal bands (TIR) with 90 m ground resolution: on the whole nine spectral bands, including the backward looking NIR ones.

More specifically, five ASTER scenes were used. Three, acquired before the earthquake, cover the Northern and Southern parts of Port-au-Prince as well as the Miragoane lake area, on the south-western side of the island, while other two, recorded after the earthquake, show the capital center and the Miragoane lake area (Figure 1, left).

The two pre-earthquake images, showing the Northern and Southern parts of Port-au-Prince, were acquired on January 11th 2009, with a cloud cover of 1% and 12% respectively. The pre-earthquake imagery covering the Miragoane lake area was gathered on January 18th 2009 at (2% cloud cover). On the other hand, the two post-earthquake images, showing the capital centre and Miragoane lake area, were acquired respectively on January 21st 2010 at with a 0% cloud cover and on January 8th 2011 (4% cloud cover).

PREPROCESSING

Before applying any image processing method to the acquired scenes, first of all, it was necessary to carry out suitable pre-processing procedures for correcting and preparing the original data.

There were two pre-earthquake scenes, covering the capital area on the northern and southern sides. So, it was created a mosaic consisting of the pairs of the VNIR (green, red and near-infrared) bands which later became a stacked three bands file.

It was then applied a mask to the pre-quake mosaic scenes according to the post-quake scene to create the final stacked image that covers exactly the same area as the post-quake image. Next, the two images were co-registered (3) using a number of tie points that were inserted manually on pixels that the user evaluates covering the same area.

15 Ground Control Points (GCPs) with a RMS of 0.004 were used for the capital

images and, as regard the Miragoane lake images, 11 GCPs were employed with a RMS of about 0.589.

As far as the data Radiometric Correction is concerned, the VNIR bands radiance values were converted to relative reflectance by applying the IAR Reflectance Calibration which normalizes the pixel values of original bands to the average spectrum calculated from the entire scene (3).

On the other hand, the TIR bands were radiometrically calibrated by applying, more specifically, the Thermal Atmospheric Correction for approximating and removing the atmospheric contributions from thermal infrared radiance data. The algorithm first determines the wavelength that most often exhibits the maximum brightness temperature. This wavelength is then used as the reference wavelength. Only spectra that have their brightest temperature at this wavelength are used to

calculate the atmospheric compensation. The surface temperature of every pixel is estimated from the data and used to approximate the brightness temperature using the Planck function (3).

ANALYSIS METHODS

As it was mentioned before, first of all, it was necessary, for applying the next image processing procedures, to create stacked files of VNIR bands and other ones of the TIR bands as regards the imagery acquired before and after the earthquake.

Principal Component Analysis

The Principal Component Analysis (PCA) was applied to a stacked file including the 3 VNIR bands of the pre- and post-earthquake scenes, covering the Haiti capital, obtaining on the whole six Principal Components (PC). As such, important statistical information can be taken analyzing the resulting eigenvectors and eigenvalues matrixes.

It appears that all the eigenvector values of the first PC are positive while the second PC exhibits positive values for the pre-quake bands and negative ones for the post-quake bands. This means that the second principal component is possibly somehow highlighting the differences between imagery acquired before and after the earthquake (Figure 1, right). In dark tones are showed areas appearing brighter after the earthquake than previously. These areas exhibit high 2nd PC negative values. It is possible also to pinpoint changes along the coastline of the capital. On the other hand, the eigenvalues matrix shows that the first band collects the 67.24% of the whole components information, while the second one gets the 24.55%. The PC3 up to the PC6 bands get 5.99%, 1.47%, 0.47% and 0.27% respectively and collect the total noise as well.

Next, the PCA was applied to the thermal bands of pre- and post-earthquake imagery covering the Miragoane lake obtaining ten Principal Components in total. Unfortunately, the corresponding results were hindered by the high cloud coverage of the thermal imagery acquired after the earthquake over Miragoane lake area.

Normalized Difference Vegetation Index (NDVI)

Another image analysis method that was applied to the Haiti ASTER bands was the calculation of the *Normalized Difference Vegetation Index* (NDVI) whose values indicate the amount of green vegetation present in a given pixel. Higher NDVI values indicate greener vegetation. First of all, NDVI was calculated separately from the stacked files of Red and NIR (Nadir looking) bands of ASTER scenes covering the Port-au-Prince area and acquired before and after the earthquake. NDVI images taken after the earthquake showed that there are some parts of the capital coastline and some other regions in the capital centre where the pixels had got big negative values, what does mean strong shortage of vegetation on these areas. Conversely, the pre-earthquake NDVI images exhibited more extensive positive values; this can be an indicator of changes that appeared in the area and would represent vegetation or land use alterations that possibly have a relation with the 2010 earthquake.

Moreover, the NDVI was calculated from the stacked Red and NIR bands of the pre- and post-earthquake imagery covering the Miragoane lake region: the resulting images show clearly enough the extensive cloud coverage of the scene. Clouds appear very dark because of the cloud high capability of absorbing the sun radiation. Just due to this extensive cloud coverage over most of the image, only the lake was selected as study area since it appears quite clear on both date images. Moreover, north and south of the Miragoane Lake passes a segment of EPG fault that makes the area more interesting to be studied. Comparing the NVDI images obtained from the two dates, alterations show up along the lake coastline and not only there.

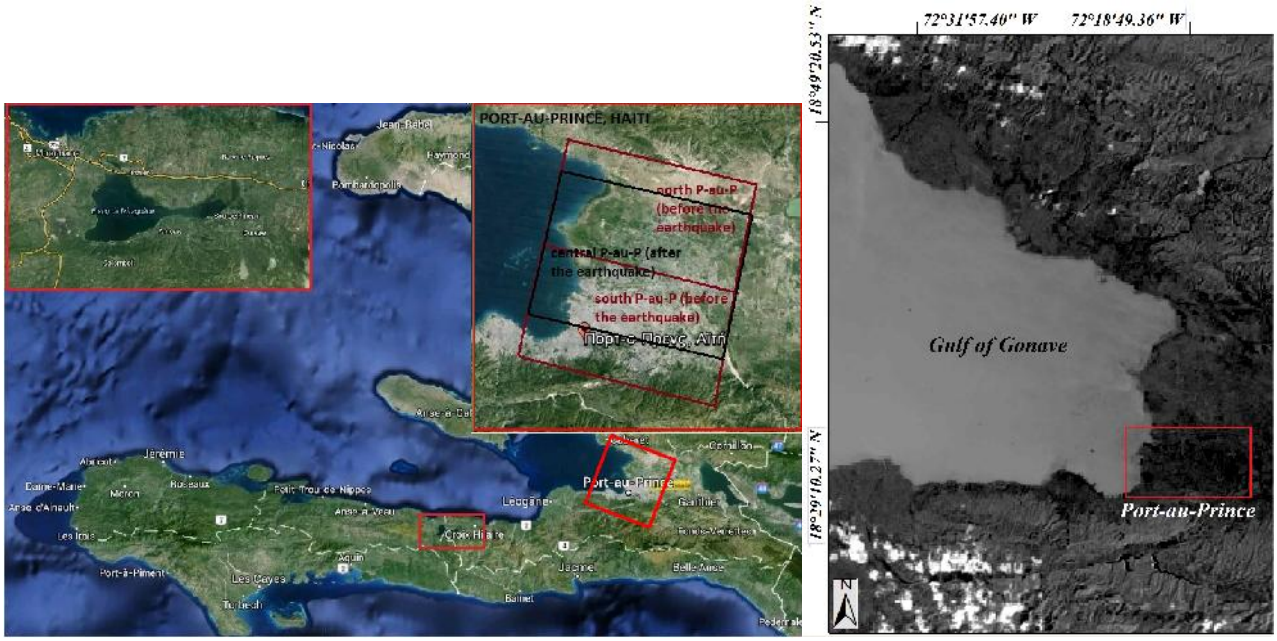

Figure 1: (Left) Location map of the study areas shown within red squares. (Right) 2nd Principal Component obtained by processing the VNIR bands of the images covering the Port-au-Prince and the broader area, acquired before and after the earthquake

False Colour Composite (FCC) Images

Another image processing method applied to the ASTER imagery was the False Colour Composite (FCC) of peculiar by-products. In particular, the combined bands were the aforementioned NDVI images gathered from different dates. As such, the pre-earthquake dates were indicated as NDVI 2009 for both study areas whereas the post-earthquake dates as NDVI 2010 for the capital area and NDVI 2011 for the lake area respectively. The FCCs were set adopting as Red band NDVI 2009, as Green band NDVI 2009 and as Blue one NDVI 2010 or NDVI 2011. Thus, FCC (Figure 2) were obtained that appear in grey, yellow and blue colours. Areas depicted in grey colours show up where no temporal changes have occurred, while yellow colour areas stand for regions that during 2009 were reflecting more than after the earthquake (as yellow sets the red and green colours contribution). This probably means that yellow shades have to do with vegetated regions that after the earthquake do not exist anymore or changed their use (like sedimentary areas). The opposite may occur also for the blue colour areas. Blue regions represent vegetated areas that were reflecting more after than before earthquake. Serious alterations can be easily observed along the whole lake coastline and the characteristic islet on the eastern side of the lake (Figure 2, right). A significant observation about the two NDVI images is that for the capital image on the south the clouds that existed before the earthquake look blue while for the lake NDVI image the clouds look yellow because existed after the earthquake.

RESULTS

The outcomes of the whole image analysis process evidenced that the original data, gathered for this study, were carrying various problems like extended cloud coverage especially in regions of interest in both study area scenes. More specifically, the pre-earthquake capital images had cloud coverage over a specific area on the south that didn't cause such a serious problem to the study, while the post-quake lake images exhibited extended cloud coverage on the whole scene, so hindering the analysis.

Furthermore, the VNIR bands spatial resolution was not enough for a more detailed research of destroyed buildings on the capital centre; however, it provided a satisfying overview of the situation after the earthquake. In this framework, figure 3, showing the 2nd PC of stacked VNIR bands of pre- and post-quake images, exhibits areas and important buildings in the capital that suffered

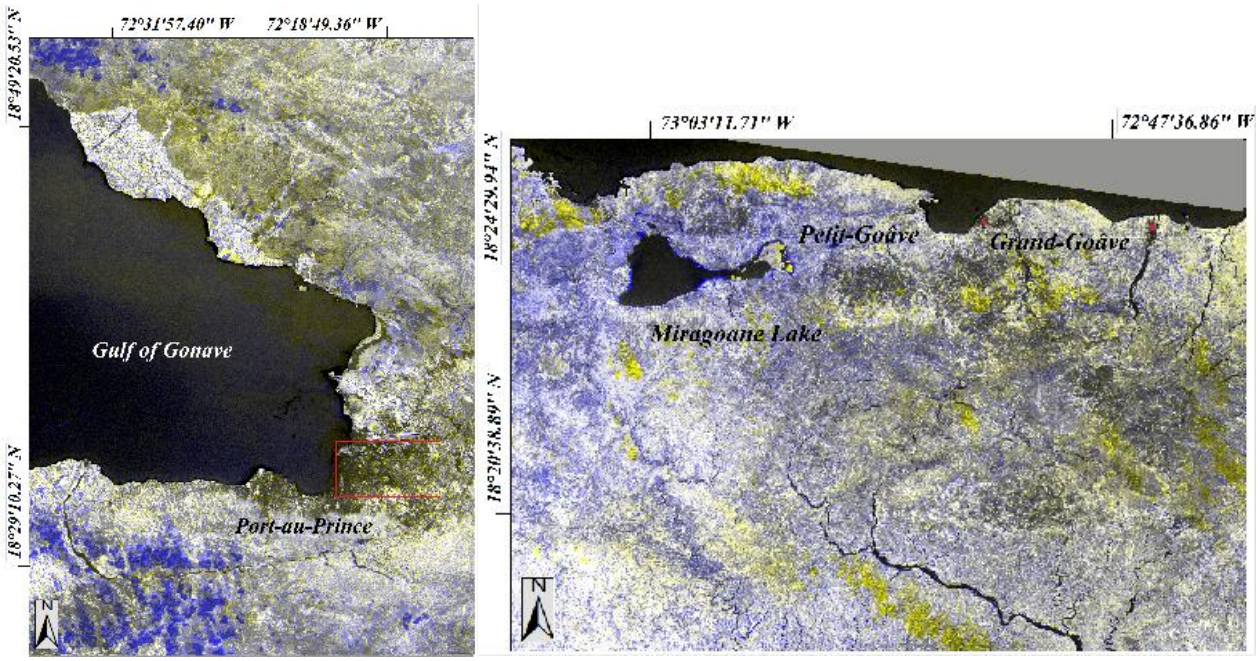

Figure 2: (Left) FCC image of NDVI '09 and NDVI '10, Port-au-Prince. (Right) FCC image of NDVI '09 and NDVI '11, Miragoane lake

severe damages like the National Palace of Port-au-Prince and the building of the National Bank of the Republic of Haiti. Moreover, there are regions shown in black that represent the buildings that collapsed completely or partially. They are: the National Palace, the Haitian Parliament, the Haitian Foreign Ministry, the Bank of the Republic of Haiti, the *Sainte Anne* church, the Country Supreme Court, the *École des Casernes Dessalines* facilities, the *Congrégation des Sœurs de Notre-Dame* building, the Turgeau hospital, the *Saint Louis roi de France* cathedral, the Saint John evangelist school and an area of debris. These results were checked with the International Chapter and SERTIT damage maps. It seems that some areas that are shown in these maps have been detected. Of course, it was impossible to identify these buildings with ASTER imagery because of its relatively low spatial resolution, but it could be stressed that the 2nd PC is showing in dark colours whole areas around these buildings that are seemingly destroyed areas.

On the other hand, as far as Miraogane lake area is concerned, figure 4, where a *FCC* of multitemporal NDVIs is portrayed, shows specific areas along the lake coastline where many alterations and changes can be observed. Most of these occur on the eastern side of the lake coastline.

CONCLUSIONS

Current results of this research were related with other similar studies (4) and, as aforementioned, with study maps from USGS and other geo-portals for pinpointing the damaged areas and comparing the obtained results.

Many buildings where is known that have collapsed were difficult to be pinpointed by means of the results of the present study because of the not extremely high spatial resolution, while areas of collapse were detected on some analysis by-products.

Useful recommendations for future research should be the acquisition of imagery with better spatial resolution, preferably with the same viewing geometry, for obtaining more valuable results and managing to contribute to the study of the effects of the Haiti strong earthquake.

REFERENCES

1 A A V V, 2011. Special Issue: Haiti 2010 Earthquake. PS&RS, 9: 883-952

2 A A V V, 2011. Special Issue: Haiti 2010 Earthquake. PS&RS, 10: 995-1066

3 ENVI Version 4.7, 2009. Getting Started with ENVI, ITT Visual Information Solutions

4 de las Doblas Lavigne M, 2010. Geological Deformations & Potential Hazards triggered by the 01-12-2010 Haiti Earthquake (Google Earth Imagery), In: GEO Haiti Event Supersite Website, 03-11-2010.

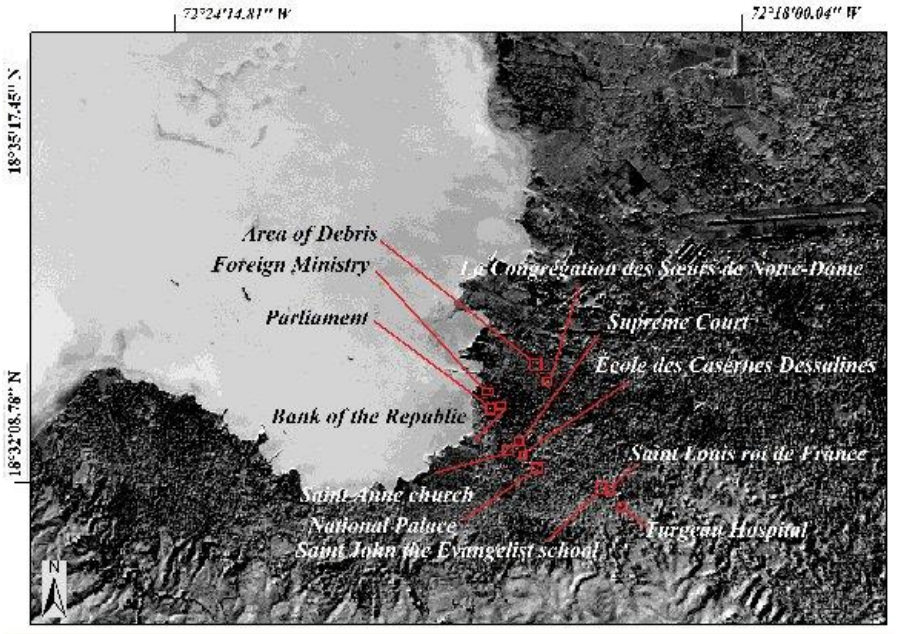

Figure 3: Damaged areas and collapsed buildings in central Port-au-Prince (2nd PC)

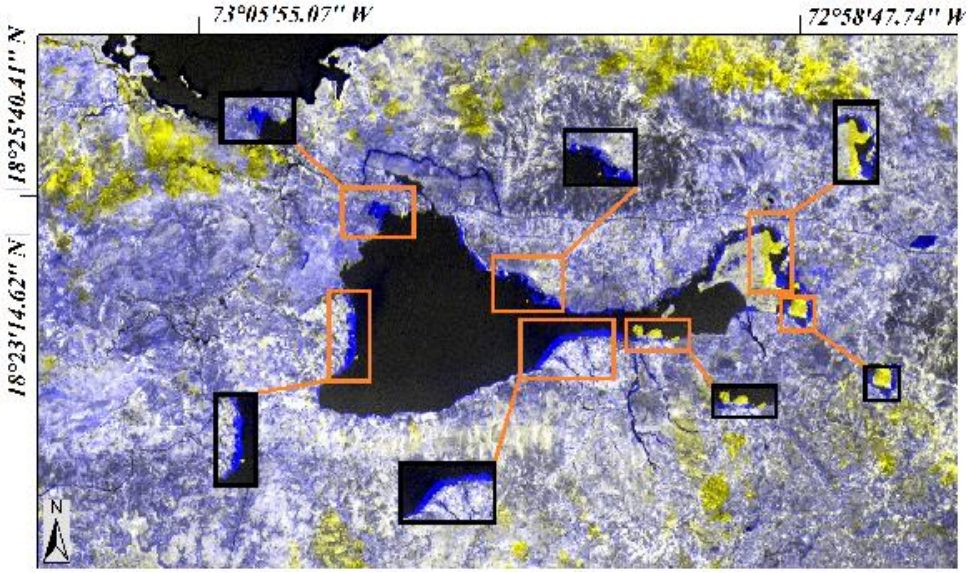

Figure 4: Changes along the Miragoane lake coastline (FCC of multitemporal NDVIs)

AUTOMATIC DRAINAGE EXTRACTION FROM REMOTE SENSING DATA

Konstantinos G. Nikolakopoulos[1], Cristos Choussiafis[2] and Vassileia Karathanassi[2]

1. University of Patras, Department of Geology, Patras, Greece; knikolakop@upatras.gr
2. National Technical University of Athens, School of Rural Engineering, Athens, Greece; christos_hous@hotmail.com, karathan@survey.ntua.gr

Abstract

The hydrological network analysis was based for many years on the topographic maps of the Hellenic Military Geographical Service (HMGS). The evolution of GIS software and the existence of many satellites acquiring stereo data with global coverage made possible the DSM creation and the automatic drainage extraction. In this study the suitability and the accuracy of drainage network derived from ALOS PRSIM remote sensing data are validated with reference to the respective information from the topographic maps of 1/50.000. A fifth order sub-basin of Alfios river in Western Peloponnese was selected for the validation.

INTRODUCTION

The automatic DSM generation has become an important part of international research in the last 10 years as a result of the existence of many satellite sensors that can provide stereo pairs. Many new algorithms have been developed, the performances of which have been assessed and reported in the literature [1], [2], [3], [4], [5], [6], [7], [8], [9], [10]. Especially studies on the accuracy of ALOS PRISM data have been also published [11], [12].

The aim of this study is to evaluate ALOS Prism stereo-data for their suitability to derive topographical and hydrological parameters using as reference the topographic maps of 1/50.000. The identification of drainage networks as quoted in [13] can be achieved using traditional methods as field observation and topographic maps or advanced methods using DEM and remote sensing. Concerning traditional methods we do not have the real representation of the drainage network because of the cartographic generalizations and subjective judgments of cartographers. In another study [14] it is mentioned that "remote sensing data has the advantages of spatial, spectral and temporal availability of data covering large and inaccessible areas within a short time in hydrological studies".

The area of study is situated in western Peloponnese. A fifth order sub-basin of Alfios river is selected for the validation. Two PRISM data sets acquired on 2008 and 2009 respectively were used in this study. ALOS data was provided by the European Space Agency. The 2008 set contains three scenes collected from the three radiometers. The 2009 set contains only the nadir and forward images. Thus four different stereo-pairs were used for the creation of four ALOS DSMs over the same area. Twenty-five ground control points and more than one hundred tie points were used. For all the stereo-pairs the same gcp's were used. Four DSMs with a pixel size of 7,5m were created. No further processing (editing) was done to the four DSMs.

After a first control for random or systematic errors the automatic drainage extraction was performed to the four DSMs in ARCGIS. Drainage networks were extracted from each of them. The extracted networks are compared with network digitized from the topographic map of the Hellenic Military Geographical Service (Figures 1 and 2). HMGS network has been used as a reference to the true river network. The extraction of drainage networks from the DEMs at the study area was carried out using the ArcHydro extension within ArcGIS 9.3 and Spatial Analyst Tools (Hydrology). ArcHydro tools are based on D8 algorithm [15]. We repeated the automatic extraction many times using different threshold values (50, 200, 500). As the threshold value

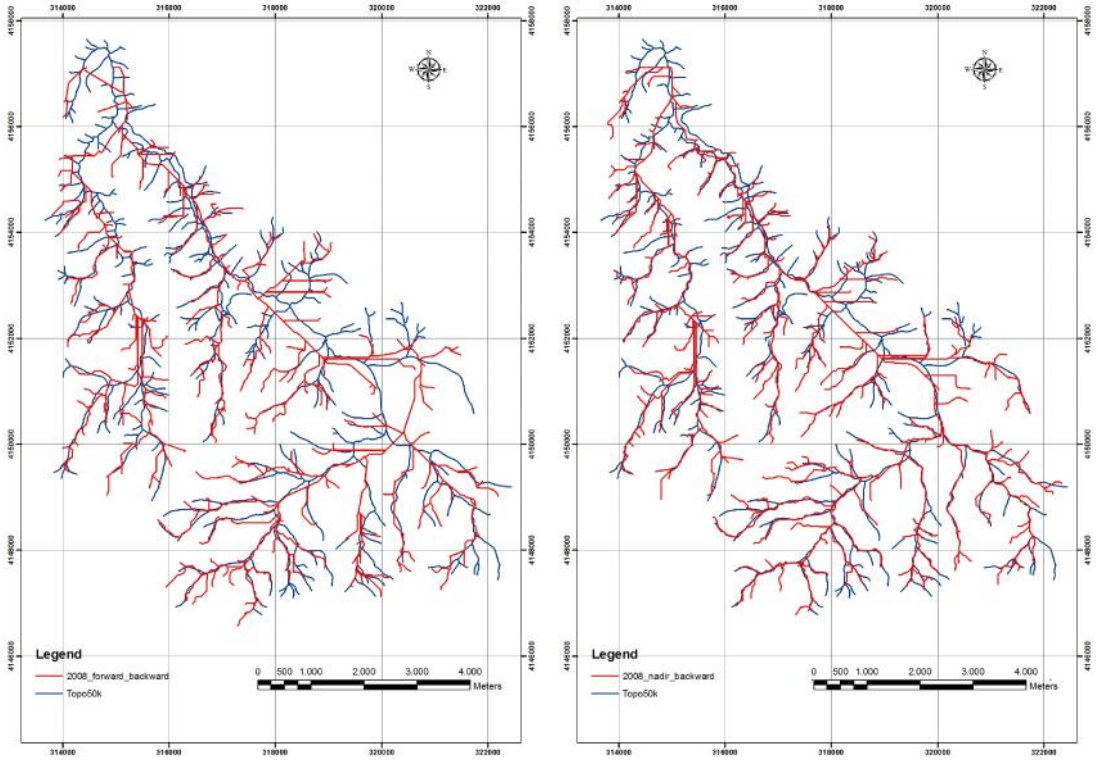

Figure 1: At the left: The extracted drainage network from the ALOS 2008 forward-backward stereo pair. At the right the extracted drainage network from the ALOS 2008 nadir-backward stereo pair. The reference network from the topographic maps is presented with blue colour.

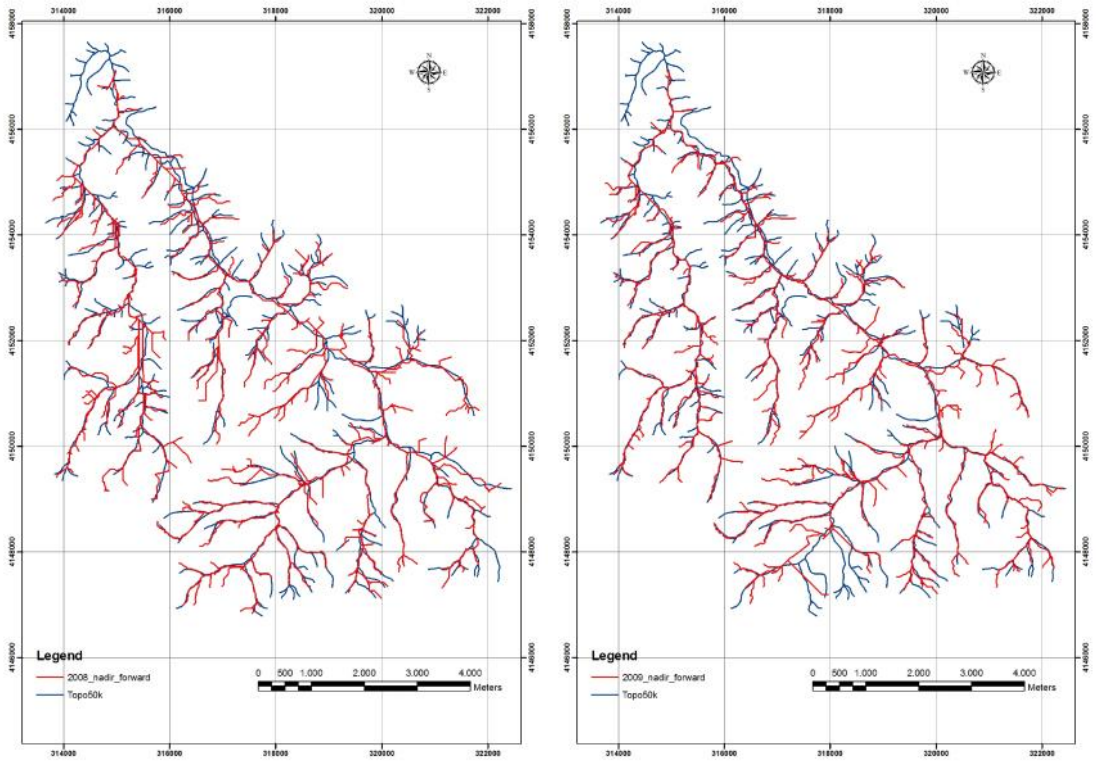

Figure 2: At the left: The extracted drainage network from the ALOS 2008 forward-backward stereo pair. At the right the extracted drainage network from the ALOS 2008 nadir-backward stereo pair. The reference network from the topographic maps is presented with blue colour.

decreases more branches are being created. In order to quantify the differences between the official drainage network that was digitized from the topographic maps and the extracted drainage networks from the ALOS DSMs the Horton's first and second laws were used. The results are presented and analyzed in the next paragraphs.

RESULTS

For the application of the first law of Horton the number of branches of the river networks under study was measured and the branching ratio (Rb) was also calculated, giving the ideal number of branches for each order and the deviations between the actual and ideal values. The tables 1-5 present the results of applying the first Horton's law for each of the studied hydrographic networks.

A first remark is that the derived networks from the ALOS DSMs presents a higher number of first order branches and a lower number of second order branches compared to the digitized network. The average branching ratios (Rb) of the extracted networks present small fluctuations and in general there are quite similar to the branching ratio of the digitized network. From all the tables It is observed that the number of the extracted branches of the hydrographic network is less than the ideal values, with the largest negative deviation in the fourth order branches (Tables 1-5). This is an index that the existing hydrographic network haven't reach its maturity level (ideal values).

For the application of the second law of Horton the mean length of branches was calculated through "clean" lengths of branches per order, the length ratio RL, ideal values and deviation of the actual values for the studied river networks. The tables 6-10 present the results of applying the second Horton's law for each of the studied hydrographic networks.

From Tables 6-10 it can be observed that the average length of the first order branches of the networks derived from the ALOs data is lower than the respective length of the of the first order branches of the digitized network. In contrary the average length of the second order branches of the networks derived from the ALOs data is higher than the respective length of the of the first order branches of the digitized network. These observations are in complete agreement with the results of the first Horton's law (Tables 1-5). Higher number of branches means a lower average length and vice versa.

The application of the second Horton's law (Tables 6-10) shows large negative deviations between the ideal and the actual values. As it can be observed in all the tables (all the extracted networks and the digitized network present high negative deviation values) this is an indication of the stage of youth for the river network.

The results from the application of the first and the second law of Horton to the extracted drainage network and to the digitized drainage network lead to the conclusion that the specific fifth order branch of Alfios river is in the youth stage and it is not given the required time to smooth the effects of geology and tectonics in the specific basin.

Table 1: Application of the 1st law of Horton to the drainage network derived from the 2008 forward backward DSM

Order	Nu Actual Values	Nu ideal Values	Deviation %	Rb	Rb_{av}
1	243	320	-23.98	4,96	4.22
2	49	76	-35.18	4,45	
3	11	18	-38.47	5,5	
4	2	4	-52.70	2	
5	1	1	0		

Table 2: Application of the 1st law of Horton to the drainage network derived from the 2008 nadir backward DSM

Order	Nu Actual Values	Nu ideal Values	Deviation %	Rb	Rb_{av}
1	266	360	-12.70	4.83	4.35
2	55	83	-52.63	4.58	
3	12	19	-36.72	6	
4	2	4	-54.07	2	
5	1	1	0		

Table 3: Application of the 1st law of Horton to the drainage network derived from the 2008 nadir forward DSM

Order	Nu Actual Values	Nu ideal Values	Deviation %	Rb	Rb_{av}
1	265	364	-27.235	4.14	4.37
2	64	83	-23.231	5.33	
3	12	19	-37.119	6	
4	2	4	-54.218	2	
5	1	1	0		

Table 4: Application of the 1st law of Horton to the drainage network derived from the 2009 forward backward DSM

Order	Nu Actual Values	Nu ideal Values	Deviation %	Rb	Rb_{av}
1	247	299	-17.38	4.41	4.15
2	56	72	-22.11	6.22	
3	9	17	-47.95	3	
4	3	4	-27.85	3	
5	1	1	0		

Table 5: Application of the 1st law of Horton to the drainage network derived from the Topo50K

Order	Nu Actual Values	Nu ideal Values	Deviation %	Rb	Rb_{av}
1	204	352	-42.00	2.55	4.33
2	80	81	-01.50	7.27	
3	11	19	-41.34	5.5	
4	2	4	-53.81	2	
5	1	1	0		

Table 6: Application of the 2nd law of Horton to the drainage network derived from the 2008 forward backward DSM

Order	L_u Actual Values in km	L_u ideal Values in km	L_u/L_{u-1}	$L_u$average	Deviation %
1	0.32	0.32		2.89	0
2	0.79	0.94	2.44		-0.16
3	1.18	2.71	1.50		-0.56
4	8.88	7.84	7.51		0.13
5	1.18	22.71	0.13		-0.95

Table 7: Application of the 2nd law of Horton to the drainage network derived from the 2008 nadir backward DSM

Order	L_u Actual Values in km	L_u ideal Values in km	L_u/L_{u-1}	$L_u$average	Deviation %
1	0.31	0.31		2.52	0
2	0.68	0.79	2.17		-0.14
3	1.54	1.99	2.27		-0.23
4	8.60	5.02	5.59		0.71
5	0.58	12.69	0.07		-0.95

Table 8: Application of the 2nd law of Horton to the drainage network derived from the 2008 nadir forward DSM

Order	L_u Actual Values in km	L_u ideal Values in km	L_u/L_{u-1}	$L_u$average	Deviation %
1	0.29	0.29		2.49	0
2	0.57	0.72	1.97		-0.21
3	1.64	1.80	2.87		-0.09
4	8.18	4.49	4.50		0.82
5	1.12	11.20	0.14		-0.90

Table 9: Application of the 2nd law of Horton to the drainage network derived from the 2009 forward backward DSM

Order	L_u Actual Values in km	L_u ideal Values	L_u/L_{u-1}	$L_u$average	Deviation %
1	0.29	0.29		2.80	0
2	0.63	0.81	2.18		-0.22
3	1.98	2.28	3.13		-0.13
4	2.03	6.39	1.03		-0.68
5	9.91	17.92	4.88		-0.45

Table 10: Application of the 2nd law of Horton to the drainage network derived from the Topo50K

Order	L_u Actual Values in km	L_u ideal Values in km	L_u/L_{u-1}	$L_u$average	Deviation %
1	0.38	0.38		2.18	0
2	0.35	0.83	0.93		-0.57
3	2.56	1.81	7.27		0.41
4	0.75	3.96	0.30		-0.80
5	0.18	8.63	0.23		-0.98

CONCLUSIONS

The application of the first and second Horton's laws on the specific fifth order branch of Alfios river based on the digitized drainage networks from topographic maps and on the automatically extracted drainage networks from ALOS PRISM DSMs lead us to the following observations:

All the extracted drainage networks from the DSM show a quite good spatial overlap with the manually digitized drainage networks, and offer a quite close representation of the actual network, as far as number of branches and branch lengths are concerned.

The statistics of the two Horton's laws to all the drainage networks indicate that the specific hydrographic network haven't reach its maturity level (ideal values).

REFERENCES

1 Toutin, Th., (2001). "Elevation modelling from satellite VIR data: a review", International Journal of Remote Sensing, 22, pp. 1097–1125.

2 Toutin, Th., (2004). "Geometric processing of remote sensing images: models, algorithms and method", International Journal of Remote Sensing, 25, pp. 1893–1924.

3 Toutin, Th., Che Nier, R. & Carbonneau, Y., (2001). "3D geometric modelling of Ikonos Geo images", In ISPRS Joint Workshop ''High Resolution from Space'', Hannover, unpaginated CD-ROM.

4 Zhen, X., Huang, X. And Kwoh, L.K., (2001). "Extracting DSM From Spot Stereo Images", In 20th Asian Conference On Remote Sensing, Singapore, Unpaginated Cd-Rom.

5 Konstantinos G. Nikolakopoulos, Emmanuel K. Kamaratakis & Nektarios Chrysoulakis, (2006). "SRTM vs ASTER Elevation Products. Comparison for two Regions in Crete, Greece", International Journal of Remote Sensing, Vol 27, No 21-22, p. 4819-4838.

6 Konstantinos G. Nikolakopoulos, Dimitrios A. Vaiopoulos, Georgios Aim. Skianis, (2004). "Comparing a DTM created with ASTER data to GTOPO 30 and to one created from 1/50.000 topographic maps", Proc of SPIE, Vol. 5574, p. 43-51.

7 Konstantinos G. Nikolakopoulos & George Lathourakis, (2005). "Along the track vs across the track satellite stereo-pair for DTM creation", IEEE, IGARSS 2005, Vol. 8, p. 5324- 5327.

8 Konstantinos G. Nikolakopoulos & Nektarios Chrysoulakis, (2006). "Updating the 1:50.000 topographic maps using ASTER and SRTM DEM. The case of Athens, Greece", Proc. of SPIE Vol. 6366, p. 6366061-11.

9 Konstantinos G. Nikolakopoulos, Panagiotis I. Tsombos & Alexandra Zervakou, (2007). "Evaluating SRTM and ASTER DEM accuracy for the broader area of Sparti, Greece", Proc. of SPIE Vol. 6746 p. 67460F1-12.

10 Panagiotis I. Tsombos, Konstantinos G. Nikolakopoulos & Lathourakis George, (2008). “DEM creation from Cartosat data and comparison to DEM from other sources”, Proc. of SPIE Vol. 7106, p.71061C1-12.

11 Panagiotis I. Tsombos, Konstantinos G. Nikolakopoulos, (2009). “DEM creation from ALOS data and comparison to DEM from other sources. A case study from Greece”. Proc. of ‘ALOS PI 2008 Symposium”, ESA SP664 Unpaginated CDRom.

12 Panagiotis I. Tsombos, Konstantinos G. Nikolakopoulos & Lathourakis George, (2009). “DSM from ALOS and comparison with airphoto DEM: the case of Thessaloniki, Greece”. Proc. of SPIE, Vol. 7478, p. 74780L1-10,

13 Ozdemir, H., Bird. D., (2008). Evaluation of morphometric parameters of drainage networks derived from topographic maps and DEM in point of floods. Journal of Environmental Geol-ogy 56 (7): 1405-1415.

14 Nikolakopoulos, K., Gioti, E. (2011). Suitability of DSM derived from Remote Sensing data for hydrological analysis with reference to the topographic maps of 1/50000. Book of Advances in the Research of Aquatic Environment 1: 121-128.

15 Liu, X., Zhang, Z. (2010). Extracting drainage network from high resolution DEM in Toowoomba, Queensland. Paper presented at the Queensland Surveying and Spatial Conference 2010, Australia, September 1-3.

LINEAMENT ANALYSIS IN NORTHERN COLOMBIA, SOUTH AMERICA

Mauricio Baquero[1], Camilo Montes[2] and German Bayona[3]

1. Corporación Geológica ARES, Bogotá, Colombia; mbaquero@cgares.org
2. Universidad De Los Andes, Departamento de Geociencias, Bogotá, Colombia; cmontes@uniandes.edu.co
3. Corporación Geológica ARES, Bogotá, Colombia; gbayona@cgares.org

ABSTRACT

Relationships that allow inferring buried structures from surface lineaments can be a powerful tool in research and exploration of natural resources such as water, hydrocarbons, and economic ores. A linear characteristic of a superficial parameter genetically related to a structural, stratigraphic, sedimentary, geochemical or to a combination of these factors is a "lineament". The way lineaments reflect structures depends on the exposure degree of the affected rock. In areas not covered by recent deposits, lineaments directly reflect structures since lineaments are the intersection between planes of discontinuity with the surface. The relationship between lineaments and structures in regions covered by recent deposits may be more complex. Without neotectonics, covered structures can control both the pre-depositional topography and the location of fluids affecting deposits. Both the original materials and its subsequent affectation have the potential to print linear signals to the surface.

Derived products from satellite imagery and DEMs were used to identify 46000 km of lineaments in 52000 km2 of exposed and covered areas. This project presents a high density of directional data collected at different scales and from different sources, providing methodological contributions in data processing, particularly in external attribute acquisition. Possible fracture patterns were characterized and geological controls on lineament orientation was described using directional analyses grouped by information on province, age and rock type affected by lineaments.

INTRODUCTION

Geological lineaments represent the intersection between discontinuity planes (e.g. faults, fractures, joints, etc.) and an observation surface. They might be enhanced by presence, linear changes or absence of drainage and vegetation. It also might be obscured when instead of a continuous line, it is expressed as an alignment of separate features. O'Leary's et al [1]–widely accepted- lineament definition is the basis for the present work: *"a mappable, simple or composite linear feature of a surface, whose parts are aligned in a rectilinear or slightly curvilinear relationship and which differs distinctly from the patterns of adjacent features and presumably reflects a subsurface phenomenon."*

A comparison between lineaments and mapped structures show that lineaments "are largely a reflection of tectonic fractures emphasized on the surface by topography, drainage, and vegetation"[2]. If no man-made linear feature is collected and bedding-related lineaments are avoided, treating lineaments as structures is a possibility. Since most important faults are probably mapped in our work area, it is likely that non-fault-matching-lineaments represent fractures.

Lineament research has been focused in diverse manners used diverse source datasets and with multiple applications. Using multispectral data ([3],[4]), topography from relief maps and DEMs([5],[6],[3]), Radar ([7]). Popular applications include mineral mapping ([7]), groundwater ([8]), neotectonics ([2]), regional geology ([9],[10],[5],[6],[3]) and volcanism ([4]).

Because lineament interpretation is highly subjective, multiple attempts to produce a more robust, repeatable and interpreter-independent method have been proposed. Examples include Hough-

transform ([11],[12]), edge-detection ([13]), object-oriented analysis ([14]), and fuzzy B-spline algorithm ([15]).

While most accepted lineament definitions don't involve scale, we did not find work examples with short lineaments. There are however multiple examples of regional-only lineaments in Colombia ([5],[6]) and elsewhere ([10],[7]).

The goal of this paper is to describe the methods employed in collecting and processing lineaments from multispectral and topographic datasets, using low-length threshold, high-density collection. This approach might produce less dependence on interpreter subjectivity. By adding geological attributes to the lineaments, the present work also pretends to characterize the possible controls that rock age, type and province might exert on geometric aspects of lineaments in this region of northern Colombia.

Location

The project is located in the northern part of Colombia (Fig 1) by the Caribbean Sea, in an area withtwo regions with contrasting precipitation regimes:lush mountain ranges in the southand a desert lowland region with three hilly areas in the north (Fig 2). Sierra Nevada de Santa Marta (SNSM), a triangular massif having the highest point on earth by the sea side (5800m) and Serranía de Perijá (PER) a lower mountain range reaching 3500m in the Colombia-Venezuela border; Cesar-Ranchería (CR) basin is a lowland lying between these elevated regions. Guajira peninsula contains two main lowland regions, Alta and Baja Guajira. The former contains three hilly areas the Serranías of Macuira (MAC), Jarara (JAR) and Cocinas (COC) with elevations below 600m.

Figure 1. Work area (yellow box)

Geology

Figure 2 displays geological provinces of the work area, which is located along the southern Caribbean Plate boundary, a margin owing its character to the oblique convergence and right lateral shearing between the Caribbean plate and northwestern South America ([16]). Baja and Alta Guajira are depressed provinces filled with Neogene and Recent deposits, while the three ranges in Alta Guajira expose mostly metamorphic and sedimentary Precambrian to Mesozoic rocks. Right-lateral Oca Fault separates northern from southern provinces. Cesar-Ranchería Basin fills with Recent sediments the space and masks the suture between Sierra Nevada de Santa

Marta, a triangular 5800m massif of mostly Precambrian to Mesozoic metamorphic and intrusive rocks, and Serranía de Perijá, a mountain range mainly composed of sedimentary Paleozoic to Mesozoic rocks.

Table 1 contains the main features of the provinces included in Figure 2.

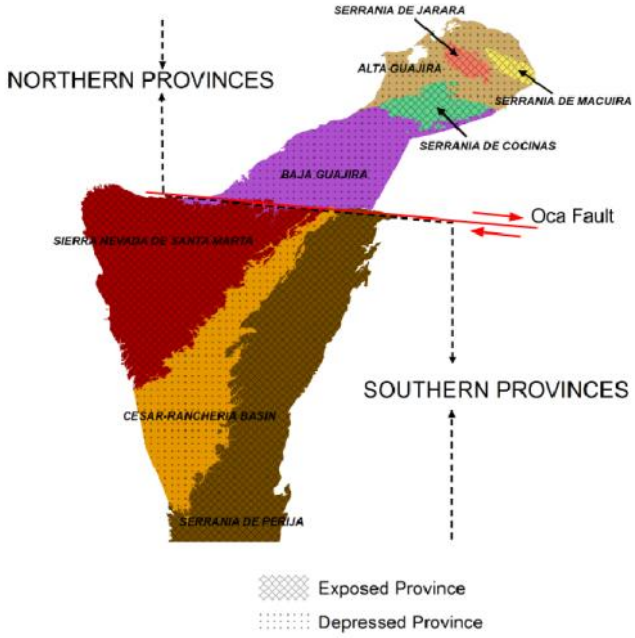

Figure 2. Map of Geological Provinces

Table 1: List of Geological Provinces.

PROVINCE	ABREVIATION	GROUP	TYPE
Alta Guajira	ALTA	Northern Provinces	Depressed
Serranía de Macuira	MAC	Northern Provinces	Exposed
Serranía de Jarara	JAR	Northern Provinces	Exposed
Serranía de Cocinas	COC	Northern Provinces	Exposed
Baja Guajira	BAJA	Northern Provinces	Depressed
Sierra Nevada de Santa Marta	SNSM	Southern Provinces	Exposed
Cesar – Ranchería	CR	Southern Provinces	Depressed
Serranía de Perijá	PER	Southern Provinces	Exposed

METHODS

Three main steps constitute the methodology of the work: data preparation, image interpretation and directional statistics.

Data preparation

Landsat 7 and SRTM, two medium-resolution, free-access datasets were the main sources for lineament interpretation: multispectral information from Landsat data was integrated into a principal component (4th) image while 15m, Band 8 data was used as visible spectrum data source. Three SRTM-derived products (relief, slope, and aspect maps) were prepared (Fig 3).In the

northernprovinces, high-resolution World View imagery was used as an additional source data in the visible spectrum.

One of the expressions of lineaments is the shape of the surface. 90m SRTM data was used to prepare the following products for lineament interpretation: eight shaded-relief images each with a different illumination direction, a slope image and an aspect image. Shaded imagery (Fig. 3A) provided a direct way to identify aligned drainages and divides; a complete range of illumination direction allowed for a complete detection of these features. Aligned slope changes in the mountain area were identified with the slope image (Fig. 3B); in the flat regions, aspect image (Fig. 3C) allowed detecting slight changes in slope orientation.

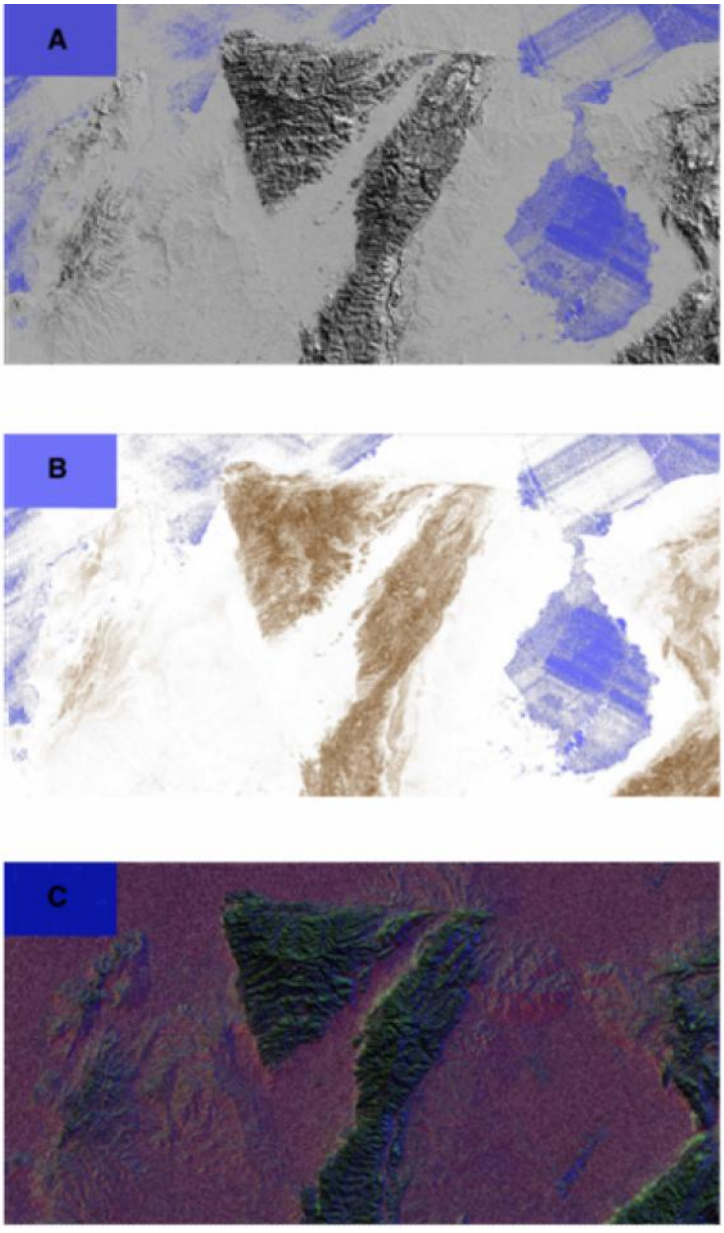

Figure 3. SRTM-derived products in the southern region. A) Example of illuminated SRTM DEM (NW illumination).B) Slope image from the SRTM DEM. C) Aspect image from the SRTM DEM.

Reflected light provide morphological and compositional information from the surface. 15m Landsat 7's band 8 visible light was multi-directionally linearly-enhanced with a Sobel filter. Multispectral information variability was integrated in a 30m Principal Component image where a similar filter was applied. PC4 showed the best potential for linear data interpretation. Landsat data provided information from the whole extent of the work area.

North of the Oca Fault, most of the region is covered with high-resolution WV data. The natural color composition available in Google Earth was used in the interpretation of more detailed lineaments in this area.

Official geological maps (1:100000 – 1:500000) where integrated into a seamless polygon coverage with province, rock age and rock type attributes.

Image interpretation and processing

All source imagery was systematically interpreted following the same rules:

1) Multiple interpretation scales. Each image dataset was progressively examined and interpreted at scales 1:600.000, 1:300.000, and 1:100.000.
2) Low length threshold. Regardless source data, 10 pixels was the minimum length that a linear feature required for collection.
3) Man-made linear features (roads, fences) and those that could be produced by image collection or processing (striping) were avoided in the collection.
4) Because the project is focused on structures, bedding- parallel linear features were avoided as well.

Lineament datasets underwent attribute generation processing in GIS environment (Fig 4).

1) Interpretation scale and source image were added as attributes.
2) Azimuth and length were calculated for all lineaments and stored as additional fields (conforming the “internal attributes” along with source image and interpretation scale).
3) Using linear referencing techniques, geology polygons were used to provide data to lineaments. These are considered the “external attributes” (Fig. 4). Rock age, rock type and province information from surface geology was assigned as attributes to the lineaments (Figs 4 and 5).

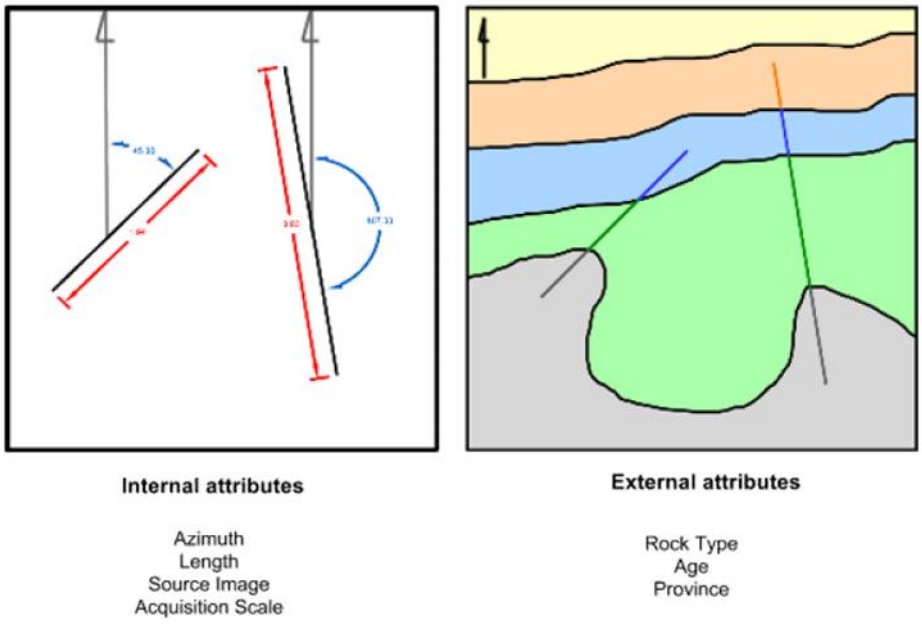

Figure 4. Lineament attributes

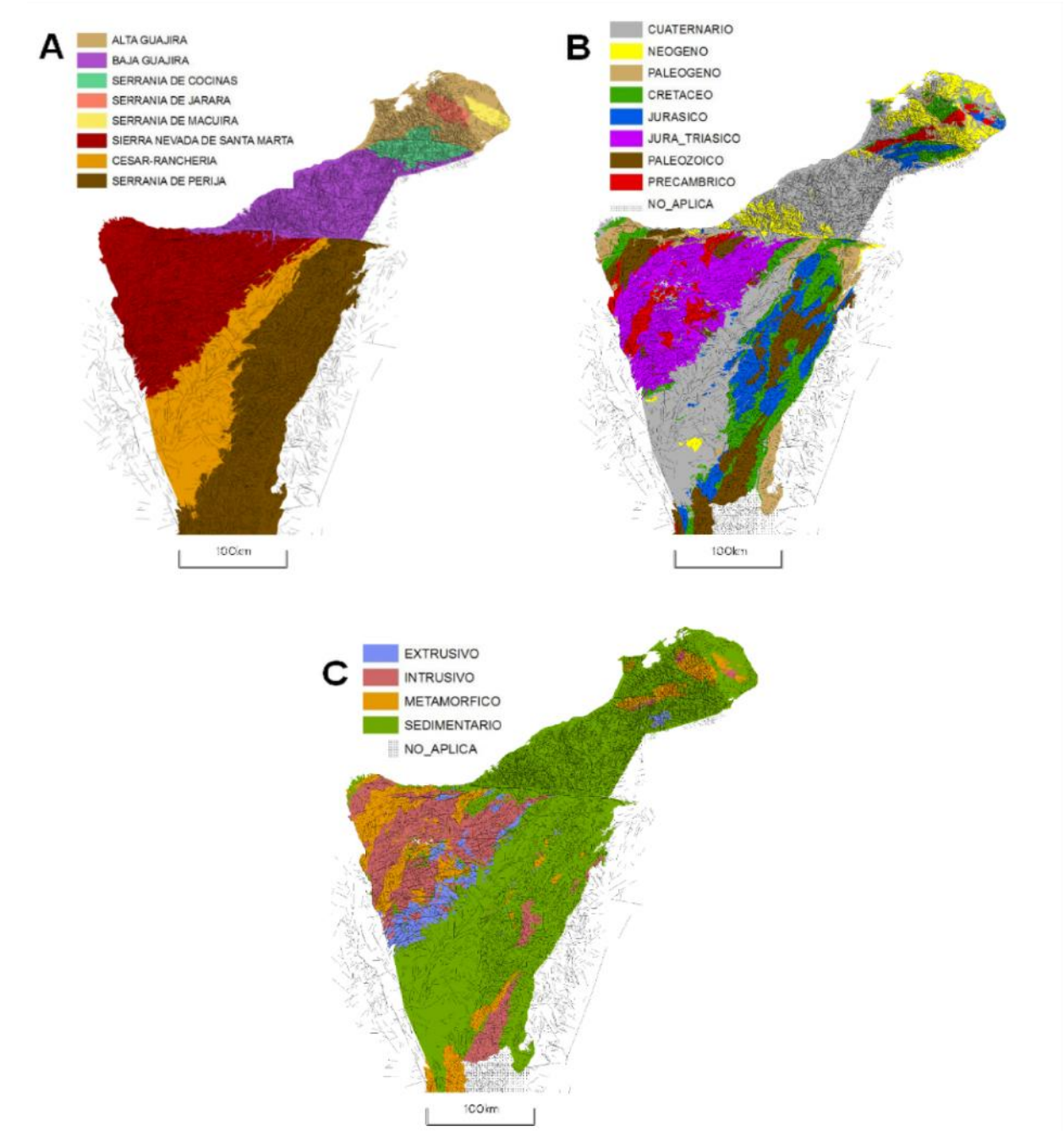

Figure 5. Lineaments with maps of provinces (A),

rock age (B) and rock type (C).

Directional statistics

The massive geographic database of lineaments covering 59000km with internal and external attributes provides opportunities for generation of rose diagrams using any combination of attributes as grouping parameters.

Using directional statistics software, exported tables allowed to generate rose diagrams that proved useful in the comparison of the variable effect that each parameter exerts on the overall orientation of lineaments.

Pivot tables were the link between the tables and the software that produced diagrams of all possible combinations of 1, 2 and 3 external attributes.

The following part contains some of the most important findings.

RESULTS

One of the first observations on lineaments is that their appearance changes with province. Figure 6A shows that SNSM has strong tendency towards NEE orientation and long curved lineaments. PER contains a long NE lineament that separates a higher density of medium lineaments in the N from shorter, less dense lineaments in the south. CR, virtually covered by recent sediments, shows the lowest density. A set of short, NW trending lineaments affects all provinces, being denser in the first two.

Rose diagrams (Fig 6B) shows that CR performs an intermediate role between opposite symmetry, bimodal distributions of SNSM and PER with a symmetric bimodal distribution whose peaks are between those of the former two.

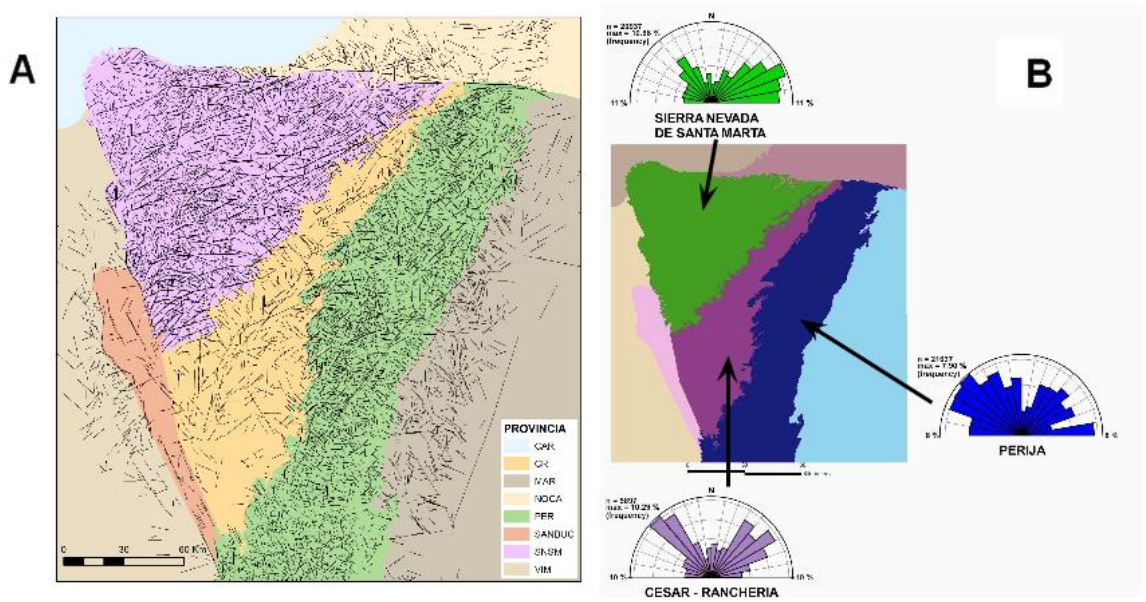

Figure 6. Lineaments in southern provinces (A) and their rose diagrams (B).

In order to establish the spatial variations on lineaments orientation, a square grid of 20km was used to segment them. Rose diagrams were constructed on top of the grid (Fig 7).

E-W lineaments are located mostly on the mountain provinces (SNSM and PER) and N-S lineaments are rare. In PER, E-W lineaments dominate the southern portion, while they are present throughout SNSM.

In SNSM, NW lineaments are more important in central (trending more NNW than NW) and northern areas (NW trend). Similarly, in the central regions NEE is the tendency, while northern areas display more NE orientation.

NW lineaments are more widespread in the northern part of PER with a NWW to NWWW preference in the south. NE lineaments are constrained to the northern half.

NE lineaments dominate CR province with some NW influence in the south and boundary regions.

The integrated lineament attribute table was used to feed directional statistics, so that multiple grouped rose diagrams were produced. Figure 8 contains the results of using external attributes (geology) in grouping all lineaments.

Province demonstrates to be the principal control on lineament orientation. As discussed before, this is clear in the southern provinces, where (regardless rock age and type) all SNSM roses show a NE tendency. Contrastingly, most PER roses show a NW direction; because of its active filling basin character, CR only shows one rose diagram (same as in figure 6B) which is the intermediate between SNSM and PER.

In the northern provinces, the effect of province is less dramatic but it is also the main control on lineament orientation. The depressed provinces show similar roses, but the difference between exposed provinces is more evident, especially in the oldest rocks.

In general, sedimentary rocks present symmetric bimodal distributions and disperse distributions, unimodal distributions are more likely to occur in igneous rocks, and metamorphic rocks are prone to asymmetric bimodal distributions. Less defined distributions tend to occur in sedimentary or Paleozoic rocks.

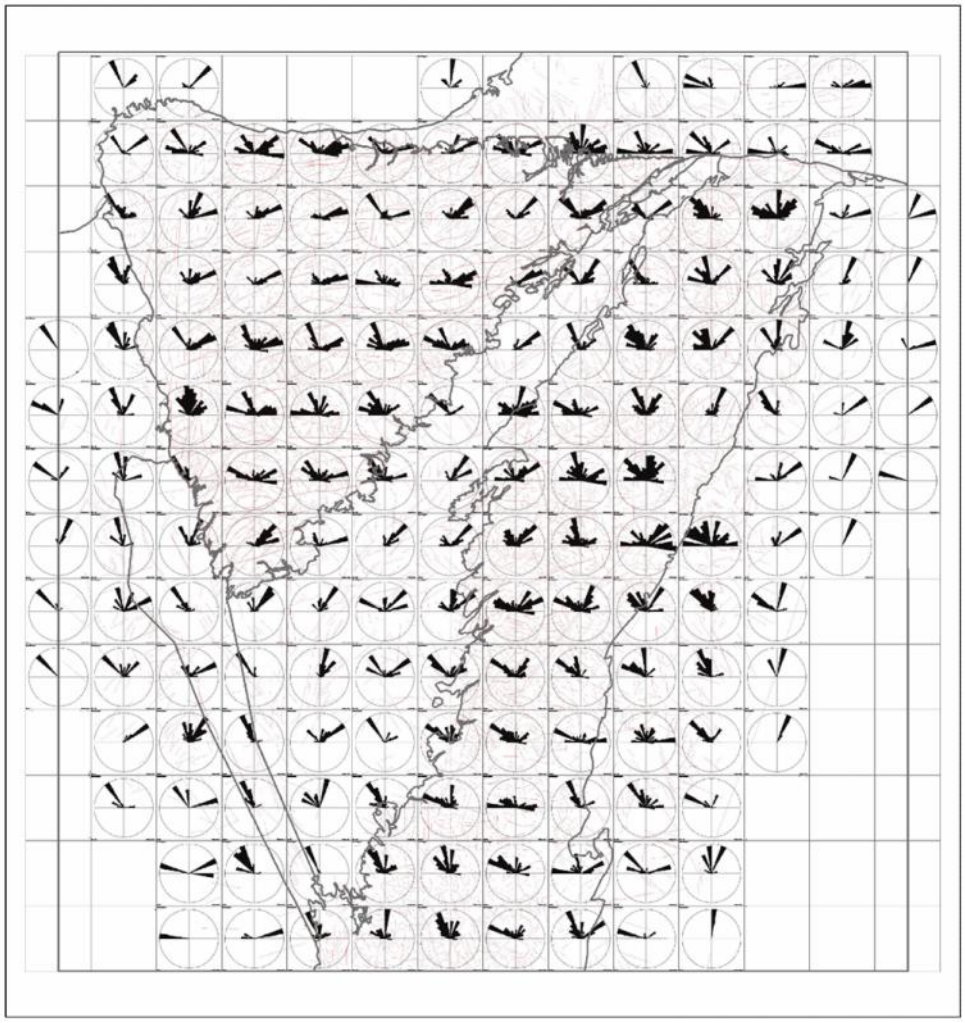

Figure 7. Variation in orientation of lineaments.

Southern provinces sampled with a 20x20km grid. Lineaments in light red.

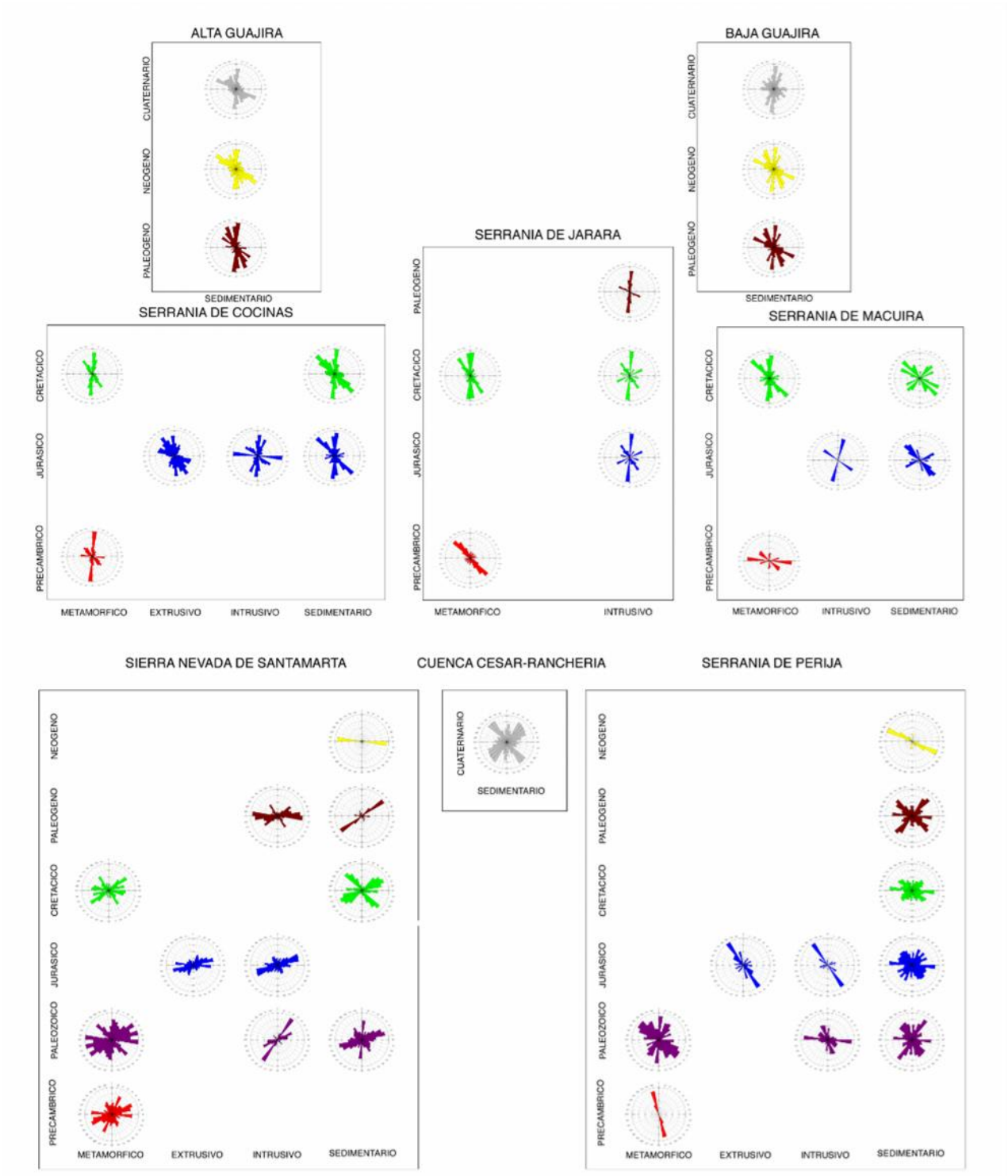

Figure 8. Rose diagrams of lineaments.

Results grouped by province, rock age and rock type.

CONCLUSIONS

The acquisition of a dense network of lineaments with internal (geometric, methodological) and external (geologic) attributes was key in producing a high population for directional statistics and evaluate geologic controls on their orientation. Geological attributes exert control on the orientation of lineaments. Province is the most important, followed by rock age androck type.

Difference in orientations between SNSM and PER supports the idea of separate evolution. Two main theories of tectonic development argue the permanent relative position of these terrains. It is difficult to explain evolution in spatial proximity that produce such disparity.

Because of its interpretative character, lineament maps might depend on the interpreter. It has been shown wide differences in interpretations from similar data sources ([17]). The proposed method of low threshold provides better amount of data for directional statistics and might reduce the interpretation variability. Further research is required in this topic.

The method relies heavily on the interpretation but this time-consuming phase is compensated with semi-automatic linear referencing and directional statistics workflows.

Possible future developments in this line of research include the identification of practical applications of an attributed lineament dataset, developing calibration strategies using field data and the development of a more robust methodology of lineament collection, less dependable on the interpreter.

ACKNOWLEDGEMENTS

This work was possible thanks to funds provided by Colombia's department of science, technology and innovation (COLCIENCIAS).

REFERENCES

[1] D. W. O'Leary, J. D. Friedman, and H. A. Pohn, 1976. Lineament, Linear, Lineation: Some Proposed New Standards for Old Terms. Geological Society of America Bulletin 87, no.10: 1463.

[2] T. I.H. Rahiman and J. R. Pettinga, 2008. Analysis of Lineaments and Their Relationship to Neogene Fracturing, SE Viti Levu, Fiji. Geological Society of America Bulletin 120, no. 11–12: 1544–1555.

[3] E. S. Papadaki, S. P. Mertikas, and A. Sarris, 2011. Identification of lineaments with possible structural origin using ASTER images and DEM derived products in Western Crete, Greece. *In*: EARSeL eProceedings, vol. 10, no. 1, p. 10.

[4] E. E. Nama, 2004. Technical note: Lineament detection on Mount Cameroon during the 1999 volcanic eruptions using Landsat ETM. International Journal of Remote Sensing, vol. 25, no. 3, pp. 501–510, Feb. 2004.

[5] G. Ujueta, 1992. Lineamientos Rio Ariari, Bogota y Gachala en los departamentos de Cundinamarca y Meta, Colombia.Revista Academia Colombiana de Ciencias, vol. XVIII, no. 70, pp. 345–358.

[6] G. Ujueta, 1994.Modelo de Desplazamiento entre la Cordillera Oriental de Colombia y los Andes de Merida. Revista Academia Colombiana de Ciencias, vol. XIX, no. 72, pp. 95–105.

[7] Shuichi Miyatake, 2002. Regional Lineament Analysis and Alteration Mineral Mapping for Intrusive-related Copper Exploration in the Myanmar Central Volcanic Belt. Presented at the Asian Conference on remote Sensing 2002, Khatmandu, Nepal.

[8] Michael W. Fies, 2004. Lineament analysis South Florida region aquifer storage and recovery regional study. U.S. Army Corps of Engineers, Jul-

2004.http://www.evergladesplan.org/pm/projects/project_docs/pdp_asr_combined/013007_asr_lineament_dtmt.pdf (last date accessed 18 August 2014).

[9] S. Christopher Caran, C. M. Woodruff, Jr., and Eric J. Thompson, 1981. Lineament Analysis and Inference of Geologic Structures - Examples from the Balcones/Ouachita Trend of Texas. Transactions - Gulf Association of Geological Societies, vol. XXXI, no. 1981, pp. 59–69.

[10] Sally N. Shake and J. Gregory McHone, 1987.Topographic Lineaments and their Geologic Significance in Central New England and Adjacent New York.Northeastern Geology, vol. 9, no. 3, pp. 120–128.

[11] Wang, Jinfei, and Philip J. Howarth, 1990. Use of the Hough Transform in Automated Lineament Detection. IEEE Transactions on Geoscience and Remote Sensing 28 (4): 561–66.

[12] A. Karnieli, A. Meissels, Fisher, Leonid, and Arkin, Yaacov, 1996.Automatic Extraction and Evaluation of Geological Linear features from Digital Remote Sensing Data Using a Hough Transform.Photogrammetry Engineering & Remote Sensing, vol. 62, no. 5, pp. 525–531.

[13] Argialas, D. P., and O. D. Mavrantza. 2004. Comparison of Edge Detection and Hough Transform Techniques for the Extraction of Geologic Features. International Archives of the Photogrammetry, Remote Sensing and Spatial Information Sciences 34. http://www.cartesia.org/geodoc/isprs2004/comm3/papers/376.pdf (last date accessed 2 Sept 2014)

[14] O. D. Mavrantza and D. P. Argialas, 2006.Object-oriented image analysis for the identification of geologic lineaments.International Archives of Photogrammetry, Remote Sensing and Spatial Information Sciences, vol. 36, no. 4/C42.

[15] Maged Marghany, 2012. Three-Dimensional Lineament Visualization Using Fuzzy B-Spline Algorithm from Multispectral Satellite Data.*In*Remote Sensing - Advanced Techniques and Platforms, Chapter 10,CInTech.

[16] Montes et. al., 2010. Clockwise rotation of the Santa Marta massif and simultaneous Paleogene to Neogene deformation of the Plato-San Jorge and Cesar-Ranchería basins. Journal of South American Earth Sciences, 29: 832-848

[17] Huntington, J.F., y A.P. Raiche, 1978. A Multi-Attribute Method for Comparing Geological Lineament Interpretations. Remote Sensing of Environment 7, n.o 2: 145-61.

REFINING OF GEOMORPHOLOGICAL MAPS OF YOUNG GLACIAL AREAS BASED ON GEOINFORMATICS AND REMOTE SENSING

Karolina Orlowska[1,2], Adrian Ochtyra[1,2], Adriana Marcinkowska[1], Elzbieta Wolk-Musial[1], Bogdan Zagajewski[1]

1. University of Warsaw, Department of Geoinformatics and Remote Sensing, Faculty of Geography and Regional Studies, Warsaw, Poland, bogdan@uw.edu.pl, adriana.marcinkowska@student.uw.edu.pl
2. University of Warsaw, College of Inter-Faculty Individual Studies in Mathematics and Natural Sciences, Warsaw, Poland, karolina.orlowska@student.uw.edu.pl, adrian.ochtyra@uw.edu.pl

ABSTRACT

Geoinformatics along with remote sensing are widely used as cartography supporting tools that allows revision and digitalization of analogue maps. The aim of this research was to test an applicability of remote sensing data and geoinformatic software in refining and updating analogue geomorphological maps of young glacial areas. The area of research covered glacial areas of north - western Poland caused by Würm glacial period (also called Wisconsin or Vistulian). All analysis were held in ESRI's ArcGIS 10 software. Two types of materials were used: scanned analogue cartographic materials (geomorphological map 1:500 000, geological map 1:200 000, topographic map 1:100000) and digital data (Landsat 5 TM RGB 453 composition and SRTM Digital Terrain Model). During the process a geomorphological map 1:500 000 has been digitalized and rescaled to 1:300 000. All map units has been manually revised, their content updated and borders refined based on information acquired from Landsat 5 TM imagery and SRTM DTM. A coded digital legend has been designed for all of the units. A database with basic geomorphological and spatial information has been attached. The results were: up to date modifiable digital geomorphological map of young glacial areas of Poland 1:300 000 accompanied with database, digital legend of geomorphological units and a printable map layout.

Keywords:geomorphology, mapping, young glacial forms, Landsat, satellite images

INTRODUCTION

Nowadays remote sensing is the main source of up-to-date spatial and environmental information used in map-making, while GIS proved to be highly applicable in its handling (1, 2). Validand detailed cartographic dataare crucial for proper decision making in environmental management, spatial modeling and spatial planning (3, 4). Geomorphological maps can provide information which support such areas as, among many others, disaster and crisis management, landslides analysis or flood prevention (4).In case of Polish geomorphological maps, there is a strong lack of current and small scale cartographic materials (5, 6). For that reasons, there is a strong need for a tool allowing to update the materials in a fast and effective way.

This paper presents an attempt of developing consistent method of analogue map digitalization and revision using geoinformatic software and remotely sensed materials.

STUDY AREA

The area that underwent analysis is north-western part of Poland, a 43538 km^2 in total. From the east the area's border is determined by a 17° 00' E meridian, from the north it is defined by the coast of the Baltic Sea, from the west by Polish - German national border, and from the south by 52° 00' N parallel of latitude (Fig. 1). It is a part of young glacial areas of Poland, caused by the Würm glacial period. Most of the occurring geomorphologic forms are the result of fluvial accumulational, depositional and erosional processes as well as glacial and fluvoglacial erosion and accumulation.

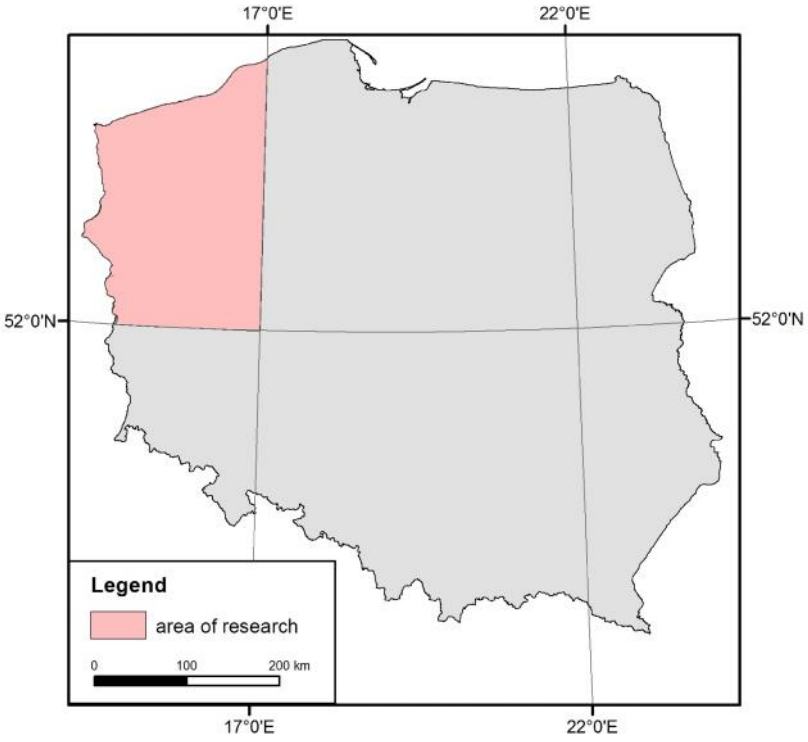

Figure 1: The area of research.

MATERIALS

The main and the most crucial material used in the research was analogue General Geomorfological Map of Poland in 1:500 000 (Fig. 2a) edited by Professor Starkel and designed in 1980 by Department of Geomorphology and Hydrology at Institute of Geography and Spatial organization of Polish Academy of Science (7). It covers 173 land forms, sorted by age, genesis and morphogenetic aspects.

Other analogue materials were: Geological Map of Poland 1:200 000 (Fig. 2b) designed by Polish Geological Institute in 1968-1998 (8) and Topographic Map of Poland 1:100 000 (Fig. 2c), published by General Staff of the Polish Armed Forces, both in SK-42 coordinate system (9).

Main digital material was Landsat 5 Thematic Mapper satellite imagery (Fig. 2d) acquired in June and July of 1992 with a spatial resolution of 30m for visible, near and mid-infrared spectrum, and 120m for thermal infrared.To increase the effectiveness of photointerpretation and strengthen the visual difference between vegetation and other types of land cover, a 453 composition was used (10).

Another material was Digital Terrain Model acquired during Shuttle Radar Topography Mission with scenes of a 1° of longitude and 1° of latitude with a horizontal spatial resolution of 30m and vertical

of 90m (10). Due to a small height difference of the area of research, the z value of the DTM had to be increased 10 times in order to enhance the visibility of land forms (6, 14). DTM was used to generate such output as: colored height model, contours for the base map and as a 3D semi-transparent terrain model (5, 6, 14, Fig. 2e).

Figure 2: Examples of used materials.

METHODS

The aim of the research was to digitalize base cartographic material - General Geomorphological Map of Poland 1:500 000 (7) - update its content and change the scale from 1:500 000 to 1:300 000, thus making it more detailed. All analyses described were held in ArcGIS 10.

A following method has been developed during the process (6, 11, 12, 13, 14, Fig. 3):

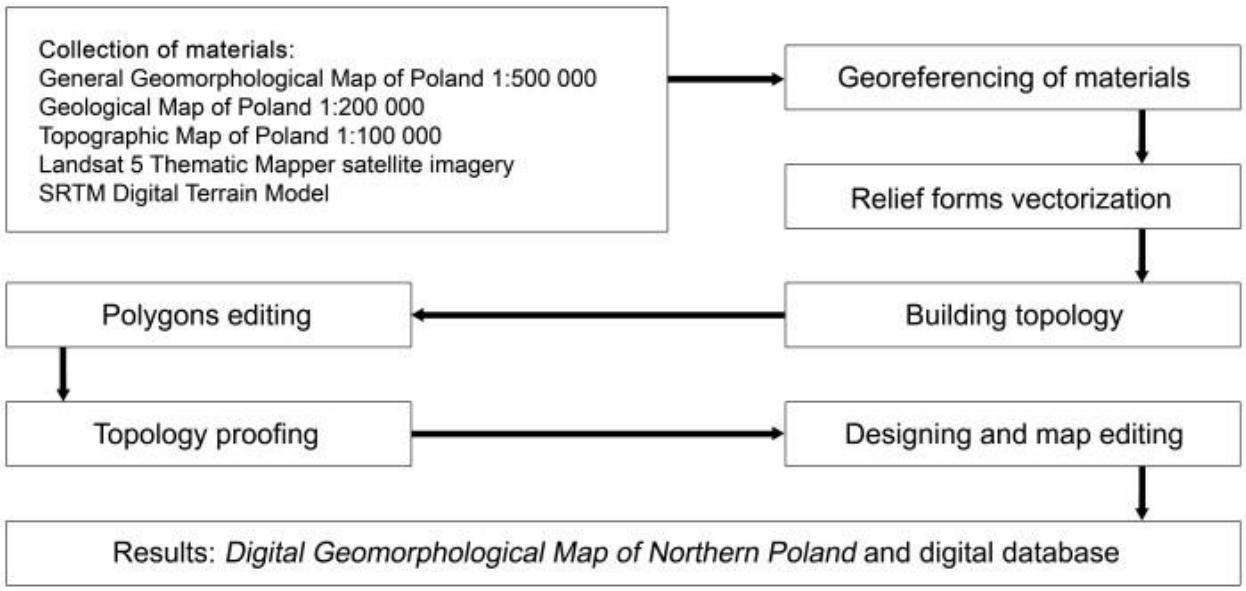

Figure 3: Schemata of the method of refining geomorphological maps.

First step was to collect all materials, both analogue and digital. Next, each sheet of all analogue materials was georeferenced using ArcGIS Georeferencing tool (Fig. 4).The overall RMSE should not exceed more than 1 pixel of an image, which gives an error of 15m in reality. The project was prepared in Polish UWPP 1992 coordinate system (6, 11, 12, 13, 14).

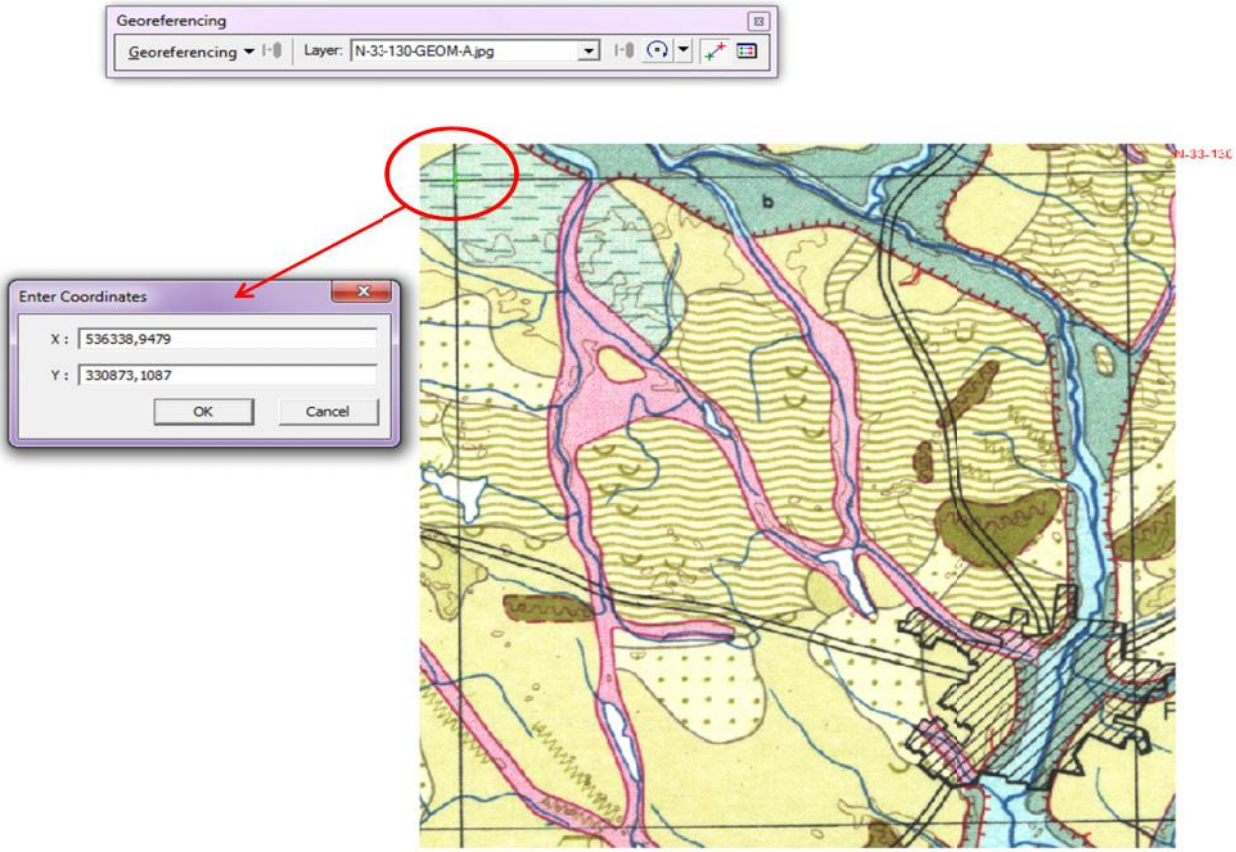

Figure 4: Georeferencing of analogue materials.

Next, all land forms present on geomorphological map of north – western Poland has been selected to be manually digitalized (Fig. 5). Form present on the base material has been consulted with additional sources, from which Landsat 5 TM imagery (10), being the most detailed material, was treated as decisive one. The form was digitalized into polygons (vast terrain forms and surface hydrological elements), polyline (rivers and erosional edges) or marked by a signature (detached, small forms e.g. single kettles) (14).

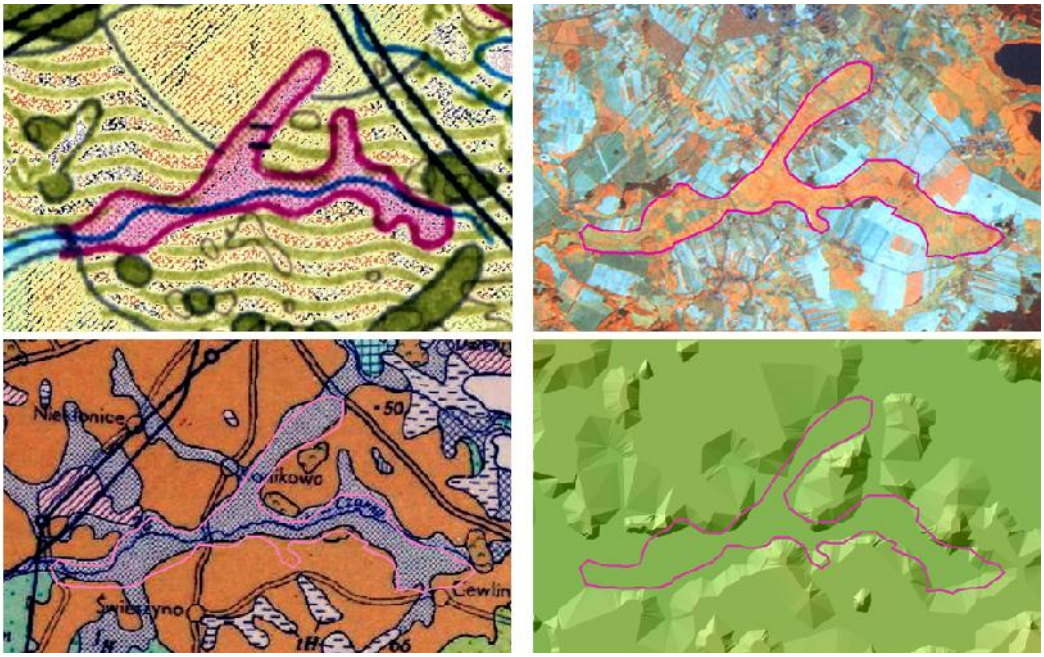

Figure 5: Example of polygon form vectorization: subglacial channels from the Vistulian – form identified on base material has its borders refined through visual interpretation of geological map, Landsat 5 TM image and DTM (14).

The following steps were: topology building and proofing, along with polygons editing. Due to the manual character of the vectorization process, most of the vectorized forms had angular shape.To eliminate this issue ArcGIS PAEK algorithm with a tolerance of 300m was applied (6, 14, Fig. 6). Moreover, a topology check was carried out which eliminated two major errors occurring in case of polygon forms: *must not have gaps* that removed any gaps between two or more forms and *must not overlap* which purpose was to avoid doubling polygons area.

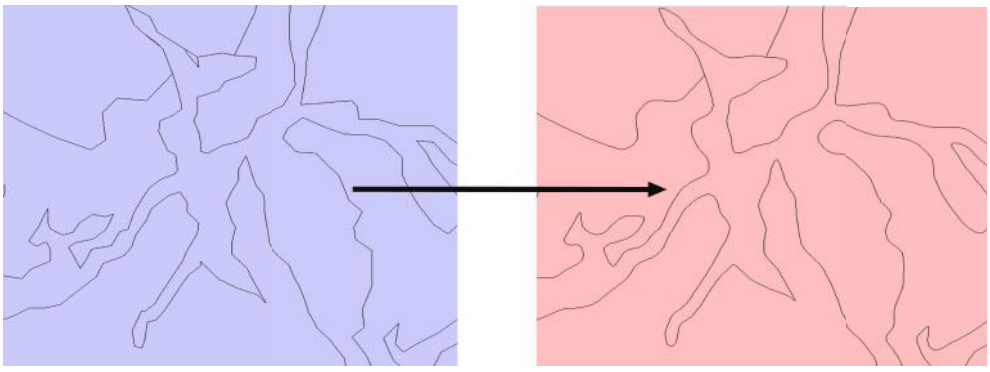

Figure 6: Results of applying PAEK algorithm.

The last step of the process was to prepare a layout of the map. The legend of the General Geomorphological Map of Poland (7) was translated into a digital version, while keeping most of its characteristic, eg. colours, shadings and symbols (6, 11). A hierarchical list of codes corresponding to each form was prepared (6, 14). Codes were added to each digitalized unit in shapefile's table of attributes (Fig. 7) allowing to apply digital legend as .lyr file(6, 14).

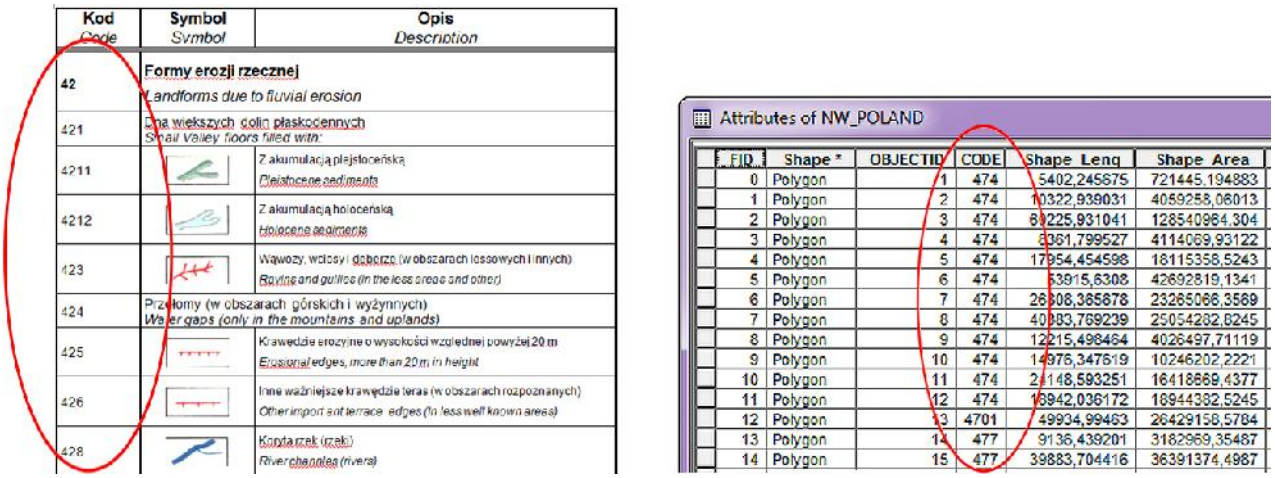

Kod *Code*	Symbol *Symbol*	Opis *Description*
42		Formy erozji rzecznej *Landforms due to fluvial erosion*
421		Dna większych dolin płaskoczennych *Small Valley floors filled with:*
4211		Z akumulacją plejstoceńską *Pleistocene sediments*
4212		Z akumulacją holoceńską *Holocene sediments*
423		Wąwozy, wąwozy i dołerze (w obszarach lessowych i innych) *Ravine and gullies (in the loess areas and other)*
424		Przełomy (w obszarach górskich i wyżynnych) *Water gaps (only in the mountains and uplands)*
425		Krawędzie erozyjne o wysokości względnej powyżej 20 m *Erosional edges, more than 20 m in height*
426		Inne ważniejsze krawędzie teras (w obszarach rozpoznanych) *Other important terrace edges (in less well known areas)*
428		Koryta rzek (rzeki) *River channles (rivers)*

Attributes of NW_POLAND

FID	Shape *	OBJECTID	CODE	Shape_Leng	Shape_Area
0	Polygon	1	474	5402,245875	721445,194883
1	Polygon	2	474	10322,939031	4059258,06013
2	Polygon	3	474	89225,931041	128540984,304
3	Polygon	4	474	8361,799527	4114069,93122
4	Polygon	5	474	17954,454598	18115358,5243
5	Polygon	6	474	53915,6308	42692819,1341
6	Polygon	7	474	26308,365878	23265066,3589
7	Polygon	8	474	40383,769239	25054282,8245
8	Polygon	9	474	12215,498464	4026497,71119
9	Polygon	10	474	14976,347619	10246202,2221
10	Polygon	11	474	24148,593251	16418669,4377
11	Polygon	12	474	18942,036172	18944382,5245
12	Polygon	13	4701	49934,99463	26429158,5784
13	Polygon	14	477	9136,439201	3182969,35487
14	Polygon	15	477	39883,704416	36391374,4987

Figure 7: Use of hierarchical coding system and attribute table.

Finally, a printable layout of the map was prepared (Fig. 8). It contained the map's content, legend, graticule, numeric and measured scale, information about the authorship and department (14).

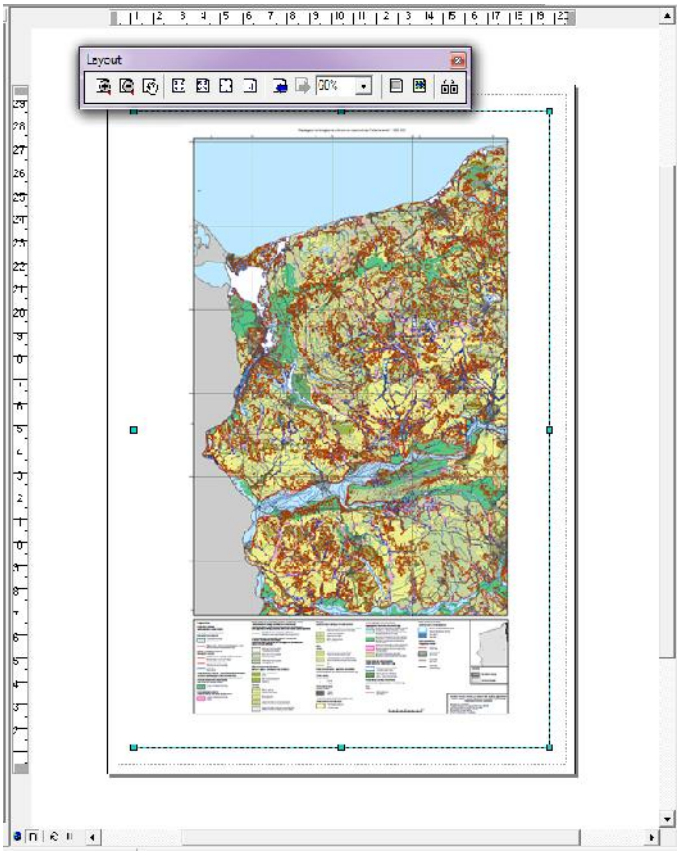

Figure 8: Map's layout.

RESULTS

The result of the conducted analysis is a set of three editable *.shp layers prepared in ArcGIS software containing as follows: 2907 polygons, 1810 polylines and 550 multipoints. A database in a form of table of attributes has been attached to all three shapefiles. The table contains codes of hierarchical numeric legend and basic spatial information about the forms - area or length. The legend consist of 39 types of geomorphological units (27 polygon, 10 polylines and 2 multipoint unit types). Moreover, a printable layout of the map in 1:300 000 was prepared.

CONCLUSIONS

The method presented in this paper shows that remote sensing materials, e.g. Landsat 5 TM (10) are highly applicable in preparation and actualization of geomorphological maps. Moreover, geoinformatic tools have wide application in map digitalization. Though successful, the method proved to be highly time consuming. It can be improved by implementation of automated solutions, thus further studies on the subject are highly recommended.

ACKNOWLEDGEMENTS

The authors would like to thank prof. dr. Jan R. Oledzki and dr. Elzbieta Wolk-Musial from the Department of Geoinformatics and Remote Sensing of the Faculty of Geography and Regional Studies at the University of Warsaw for their valuable help in the research.

REFERENCES

(1) Albertz J, Wiedemann A, 2003.Topographic and thematic mapping from satellite image data, Department for Photogrammetry and Cartography, TU Berlin, www.alwie.net/lit/lstMap.pdf (last date accessed: 20 August 2013)

(2) Pavelka K, 2009.Topographic and thematic mapping from multi-resolution satellite images, Czech Technical University in Prague, Faculty of Civil Engineering, Dept. Mapping and Cartography, Czech Republic, http://www.researchgate.net/publication/228873146_Topographic_and_Thematic_Mapping_from_Multi-Resolution_Satellite_Images (last date accessed:25September2014)

(3) Bocco G, Mendoza M& Velazquez A, 2001. Remote sensing and GIS-based regional geomorphological mapping – a tool for land use planning in developing countries, Geomorphology, 39: 211 - 219

(4) Melelli L, Gregori L, Mancinelli L, 2012. The use of remote sensed data and GIS to produce a digital geomorphological map of a test area in central Italy, In: Remote Sensing of Planet Earth, edited by: YChemin, Italy: 97 - 116

(5) Wolk-Musial E, Gatkowska M, 2011.Detailed geomorphological map of Narwianski National Park with its buffer zone in scale 1: 25000, Polish Remote Sensing of Environment, 45: 40-50

(6) Marcinkowska A, Ochtyra A, Wolk-Musial E, Zagajewski B, 2013.Geomorphological map of pomorskie and warminsko-mazurskie voivodeships using geoinformatic methods, Polish Remote Sensing of Environment, 49: 43-81

(7) Starkel L, 1980. General Geomorphological Map of Poland 1:500 000 (Military Institute of Cartography)

(8) Mojski J E, 1969-1998. Geological Map of Poland 1:200 000 (Polish Geological Institute)

(9) Topographic Map of Poland 1:100 000 (General Staff of the Polish Armed Forces)

(10) U.S. Geological Survey, www.usgs.gov, Web. 10.12.2012

(11) Borzuchowski J, Oledzki J R, 2005.Digital geomorphological map of Karpaty Mts, Polish Remote Sensing of Environment, 46: 52 - 71

(12) Krzeminski J, 2009. General geomorphological map of Podlasie (Poland) in the scale 1:300 000, Polish Remote Sensing of Environment, 42: 43-58

(13) Napiorkowska M, 2011. Digital geomorfological map of Mazovia, Polish Remote Sensing of Environment, 45: 23-39

(14) Orlowska K, Zagajewski B,2013. Digital geomorphological map of north - western Poland in a scale of 1:300 000, M.A. Thesis, Department of Geography and Regional Studies, Warsaw University

STUDYING THE FLOW OF ASOPOS AND NEMEAS RIVER SYSTEMS USING AIRPHOTOS AND GIS.

Konstantina Mexia[1]
[1] University of Patras, Department of Geology, mexiak@yahoo.com

Key words: Asopos, Nemeas, Retrogressive erosion, Reversal, Archaeological sites

ABSTRACT

The object of the present paper is to study the flow of river systems Asopos and Nemeas- which are in the wider area of the Nemea archaeological site - in order to understand how the evolution of these rivers in time affected the whole area.

The study area is a section of the NE part of the Peloponnese, specifically the zone between the villages of Velo and Vrachati.

In order to access our goal aerial photographs and GIS analysis were used. The geomorphological and tectonic analysis of the area and the development and evolution of settlements therein (based on archaeological studies) gave us clues about the shape of the terrain over time. The main factors affecting the shape of the terrain (intense tectonic activity and retrogressive erosion) were not adequate reasons - in our case - to effect immediate abandonment of the area (since they are fairly slow processes – in the human timescale). Their effect, however, is evident over time, in the form of gradual abandonment of sites, movement of settlements or the creation of new settlements.

INTRODUCTION - METHODOLOGY

The study area is located in the northeastern part of the Peloponnese, between the villages of Velo and Vrahati, in the prefecture of Corinthia. It is bounded west of the watershed of the basin of Asopos river, east of the watershed of the basin of the Nemeas river, north of the Corinthian Gulf and south by the mountains Xerovouni, Megalovouni and Tritos.

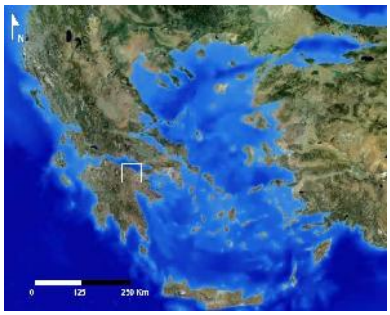

Figure 1. Study Area

The purpose of this paper is to investigate the flow of the river systems of Asopos and Nemeas and the surrounding archaeological sites situated there, in order to understand the physical processes affecting the area (e.g. Sakellariou - Faraklas 1971; Bengston 1991; Seger and Alexander 1993; Zelilidis 2000; Miller 2005). For this study we used GIS software, in order to construct a simplified geological map, a geomorphological map of scale 1:50,000, topographic maps and fieldwork. We also created maps showing the locations of archaeological sites, as they developed over time in the area, with the help of archaeological literature.

ARCHAEOLOGICAL POSITIONS

In the western part of the study area, lays the plain of Phlius, hosting the city of modern Nemea and to the east lays the lower valley of Ancient Nemea. The plain of Phlius is the largest of all Corinthian inland plains and shows traces of habitation back from prehistoric times up to the Roman period.

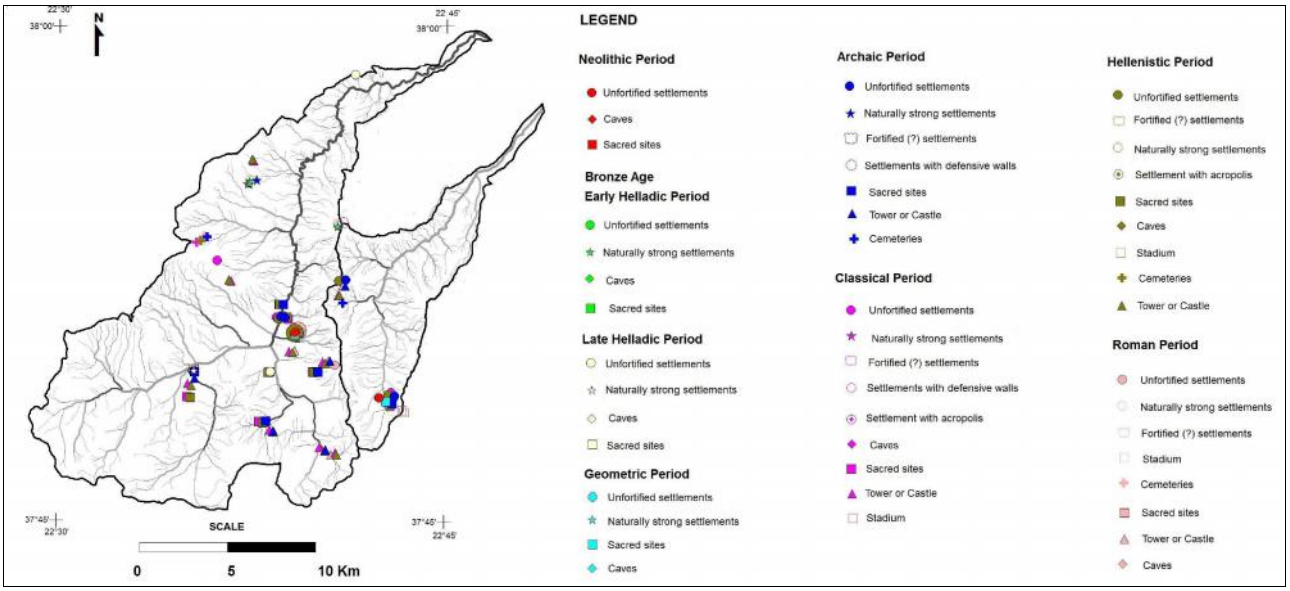

Figure 2. Archaeological Sites in the plain of Phlius and the valley of Ancient Nemea

The position that was selected for the settlement of Phlius - which is the most important settlement in the area - was the hill of Panagia. The suitability of soil and adequacy of water in the region, caused in the course of time the spread of life in other parts of the basin. The image of the area over time shows no change (figure 2).

The choice for the settlement of Phlius is mainly associated with the lithology of the area. Erodible and practically impermeable deposits enabled the construction and agricultural work that would serve and facilitate the lives of residents. The creation of the settlement between the two branches of the river (III6 and IV2), which received a significant number of smaller streams, provided the required water supply for the settlement (figure 3).

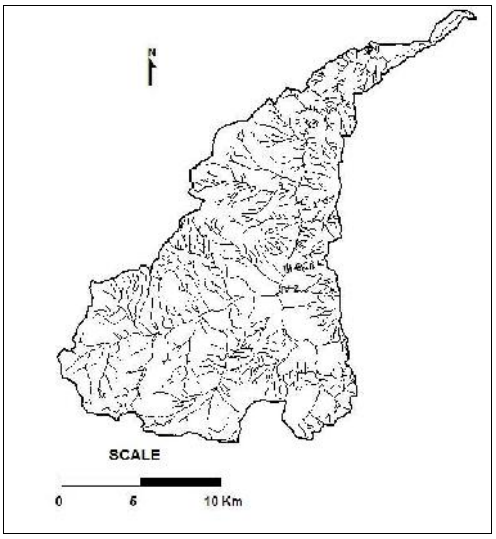

Figure 3. The III6 and IV2 branches of Asopos river

East of the plain of Phlius extends the small valley of Ancient Nemea. This valley was inhabited from prehistoric times up to the classic years. The two neighboring plains (plain of Phlius and plain of Ancient Nemea) are separated by the Trikarano mountain. Southeastern, the valley borders the hill Evaggelistria. This highland valley is long and narrow, with a width of 1600m along the E-W axis.

The modern village in the center of the valley is called Ancient Nemea (Heraklion), and extends to the southern and eastern slopes of the hill Tsoungiza (Miller 2005). The plain is crossed by the river of Nemea. The elevation at the center of the valley is 333m about above sea level.

The most important archaeological site in the valley is the temple of Nemean Zeus , which experienced two major periods of activity , the 6th-5th century BC and then, in the late 4th century BC (330 BC). At a distance of 450m east - southeast of the temple is the stadium, where every two years the famous Panhellenic games of Nemea took place. The configuration of the site of the temple of Zeus and the stadium, the restoration of the temple of Zeus and the excavations were conducted in the area for many years, from the year 1973 onwards, from the University of California at Berkeley, under the direction of Professor Stephen G. Miller (Miller 2005) (figure2).

GEOLOGY - GEOMORPHOLOGY - TECTONICS OF THE STUDY AREA

In the southern section of the study area, the geological zones of Tripolis and Pindos appear. They are represented almost exclusively by Triassic age limestone of Tripolis zone and Upper Cretaceous limestones of Pindos, in the Eastern area. In places, Eocene age flysch formations appear (zone of Tripoli) and Maistrichtean - Paleocene flysch formations (Pindos zone). In the rest of the region Pleistocene formations occur. Specifically, in the central part : conglomerates, marly conglomerates, marls, sandstone marls, and sandstones are found. These sediments were derived mainly from the southern mountains. The quaternary deposits occupy a large part of the lowland of NE Peloponnese, in the form of conglomerates and deposits, while in the same time new and old talus cones develop with significant extent, on the outskirts of the alluvial plains of Nemea and Phlius (Papanikolaou 1986) (figure 4).

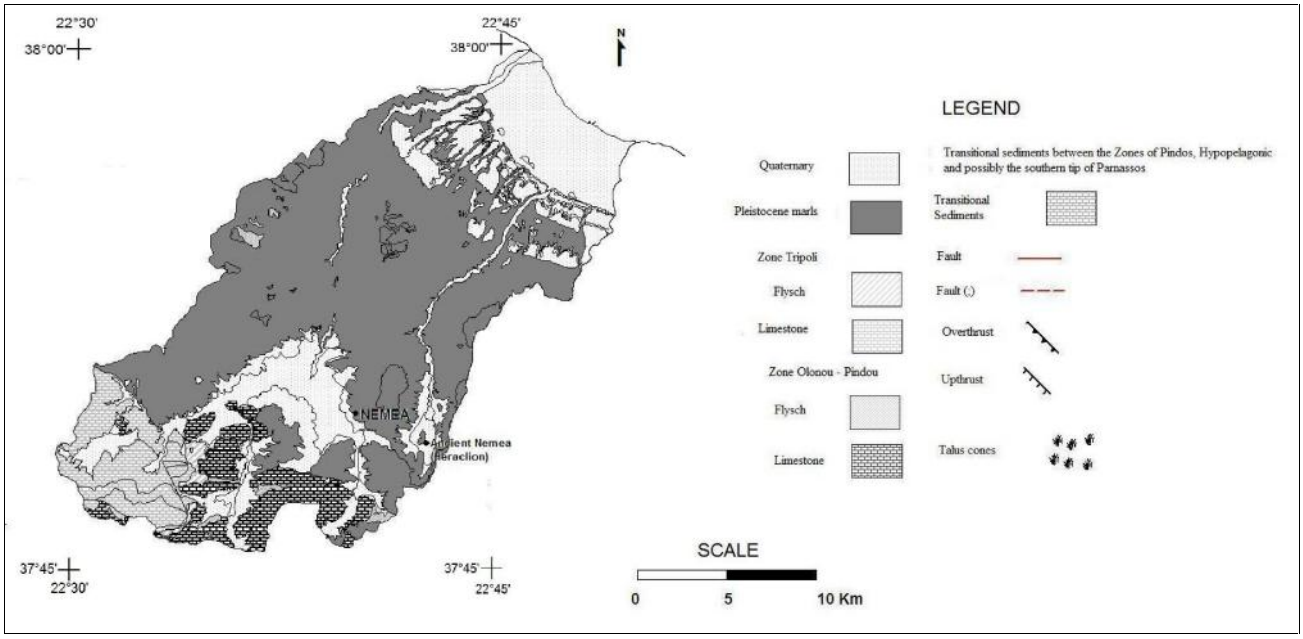

Figure 4. Simplified geological map of the study area

In the study area, lie the plains of Nemea (Phlious field) with an area of 28,6 Km2 and Ancient Nemea (6,07 Km^2), while downstream the valleys of the rivers Asopos and Nemeas or Zapantis are found. The erosion of alpine formations, derived from the southern mountain, named

Megalovouni, supply the plains of Asopos and Nemeas with large volumes of clastic material.The Asopos river originates from the mountain of Megalovouni, crosses the easily erodible Neogene deposits and flows into the Corinthian Gulf, east of the city of Kiato (figure 5). The catchment area of the river is 270.39 Km^2. The network of Asopos has a complex form that reflects the tectonic and lithological conditions prevailing in the region and cannot be classified into a specific type. There is a well developed hydrographic network, as the whole region is covered by the practically impermeable marl deposits.

To the east, the stream Nemeas or Zapantis, begins to flow from the south rim of the Ancient Nemea valley (it stems from the mounain Megalovoyni) and flows in the Corinthian Gulf (figure 5). The catchment basin of the Nemeas river has an area of 68.73 Km^2. It crosses the Neogene deposits where the retrogressive erosion is strong and flows into the sea near the village Vrahati. This is a relatively new, small drainage basin, which continues to evolve in time.

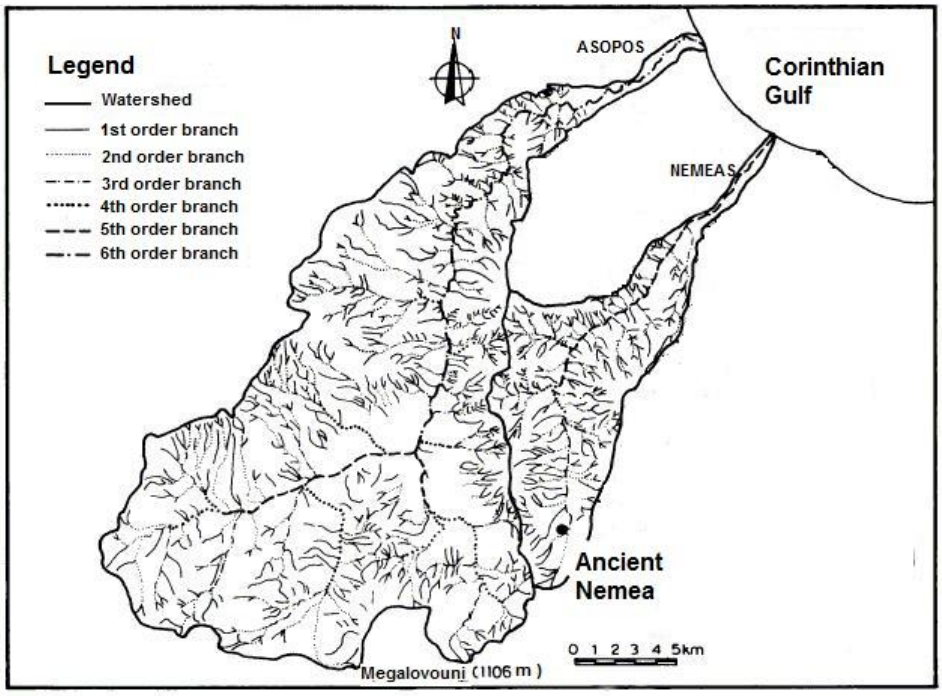

Figure 5. The two hydrographic networks: Asopos and Nemeas

THE FORMATION AND EVOLUTION OF THE AREA IN THE COURSE OF TIME

Based on the geomorphological map we charted and the presence of wind gaps and knick points, it is confirmed, that in the early Holocene, the relief was different. The tectonic activity - as evidenced by the relatively high percentage of faults, which are the result of seismic movements - caused significant changes in the course of river systems. Thus, the hydrographic networks draining the region have recorded this tectonic activity and the geomorphological processes that led to their current form. Specifically, the Asopos river in order to correspond to the lifting and backwards tilting of the southern margin of the Corinthian Gulf (which is part of the Corintian basin), reversed its course in the past to the south. An important role in the evolution of this network was played by the tectonic uplift of the region. In the early Quaternary, the network of Nemeas river and the northern parts of Asopos river did not exist. The existing part of Asopos network flowed northwards into the Corinthian Gulf. Because of the elevation of the northern Peloponnese, the coastline of the Corinthian Gulf shifted northwards and the drainage network elongated, in order to find an outlet to the sea. The high rate of elevation prevailed against deep erosion, resulting in the separation of the upstream parts of the Asopos network. This separation resulted in the reversal of flow to the south, as shown by the wind gaps which are mapped in the

boundaries of the basin. Then the evolution of the downstream part of the network, due to the rise of the northern Peloponnese and subsequent extension of it, expanded the network to the north. In the land, which emerged, the hydrographic network of Nemeas was created. The river Nemeas grows exclusively on Pleistocene deposits. At the same time, the retrogressive erosion led to the capture of the remaining streams and to the change of flow of Asopos river, once again towards the Corinthian Gulf. The wind gaps identified at the southern foot of the mountain Megalovouni, south of the city of Nemea, confirm the reversal of this network (figures 6,7). The presence of wind gaps on the southern edge of the Asopos basin, shows that this river system was unable to respond to the elevation of the area.

Specifically, the wind gaps were located at positions with the following coordinates:

a) 22°35'24" E and 37°46'48" N (figure 6)

b) 22°38'24" E and 37°45'36" N (figure 7)

Respectively, knick points in the catchment basins of river networks, show the places where, at present, there is intense retrogressive erosion. These points were found in the following locations with the coordinates:

a) about 2200 m. from the village of Leriza 22°39'00" E and 37°52'48" N (Asopos River) (figure 8)

b) about 1800 m. SW of Chalki village 22°42'36" E and 37°52'12" N (Nemeas River) (figure 9)

Figure 6.Wind gap in Asopos River

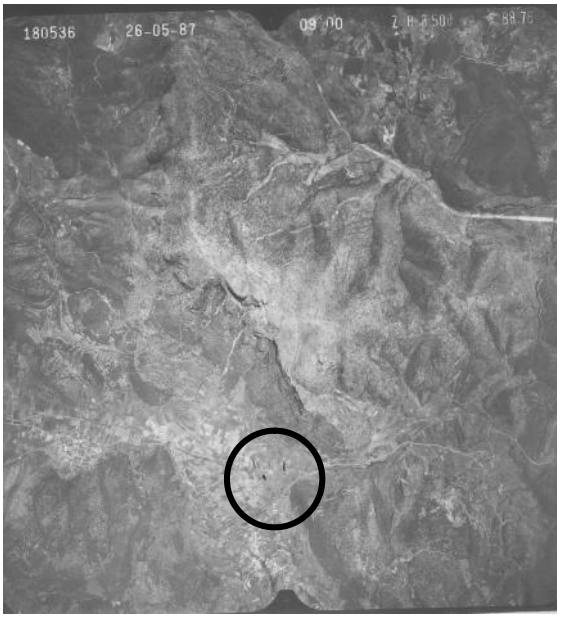

Figure 7.Wind gap in Asopos River

Based on this geomorphological regime, in Upper Holocene (5000 years BP), we witness human activity (Neolithic Age) in the area. The flow of the river has not changed significantly. The region, however, as evidenced by this study, has changed appearance, as new river branches have been created and others have been abandoned. The effect of retrogressive erosion, aided by existing fault lines and lithology, lengthened the branches of streams and differentiated the extent of the watersheds.

Going east, to the adjacent area of Nemeas river, it is likely that this valley has a different shape presently, compared to the Lower Holocene. A number of first order branches were not created back then and the lengths of branches of larger order were smaller.

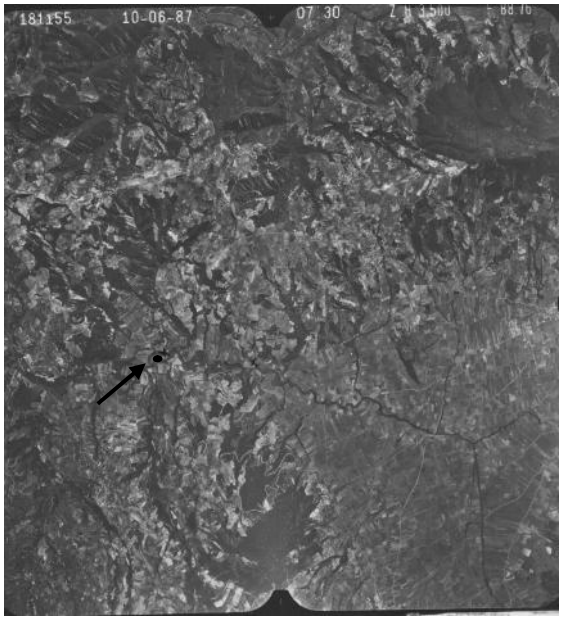

Figure 8. Knick point in Asopos river

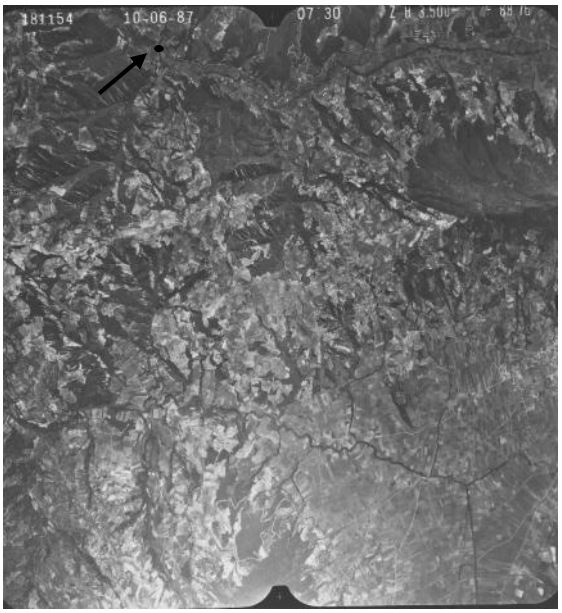

Figure 9. Knick point in Nemeas river

CONCLUSIONS

The study of the aerial photos and the GIS maps that were created, lead us to the following observations :

1. The Asopos river was created in the recent geological past (Pleistocene), with an initial flow direction to the north, ending in the Corinthian Gulf. Upward movements of northern Peloponnesus in combination with intense rift tectonism could not be compensated for by downwards erosion and this resulted in the reversal of the course of Asopos to the south.

2. In particular, the reversal of the course is attributed to secondary faults, that caused lifting and turning of individual tectonic blocks to the south (Seger and Alexander 1993, Zelilidis 2000). This procedure led to the capture of the inverted branches from the remaining rivers, which continue to flow northward. The lithology and tectonic activity of the area allow for the creation of new river branches, while retrogressive erosion, aided by other parameters, continues to be active and shapes the current relief. The effect of retrogressive erosion - as a result of corrodible marly deposits - is responsible both for the capture of Asopos river and for the shape of the northern edge of the valley of Ancient Nemea.

3. Before the Holocene (Late Pleiocene - Early Pleistocene) the river system returned to its original direction. The easily erodible Neogene deposits caused the activation of retrogressive erosion. The intense action of retrogressive erosion of pleiopleistocene deposits in the basin of Asopos allowed the capture of the remaining branches by the remaining atrophic river and the return of the flow in the original direction.

4. A significant number of new branches were created in the Holocene. This was the effect of the action of retrogressive erosion, while in the future, it is likely that new branches will be added to existing river networks, aided by lithology and tectonic activity.

5. In the Asopos basin, the presence of prehistoric residential facilities, occurs as fortified and unfortified settlements throughout, while in historic times, the area shows intense residential development. The archaeological remains (defensive walls, temples, castles, settlements) until the Roman period , are now showing the existence of organized societies .

6. In the drainage basin of Nemeas, we witness human presence throughout the Neolithic period and the Bronze Age. Specifically, on the hill of Tsoungiza archaeologists have found traces of unfortified settlements throughout the Neolithic period and the Bronze Age. During the transition to

the Geometric period, the area seems to change, with the construction of a temple in the nearby area. In the years that followed, the human presence becomes stronger as shown by the important public installations (stadium of Nemea - classical period).

7. The study area was a place with intense human presence. The residential development seems to have benefited from the geological formations (fertile and impermeable deposits - marl and marly conglomerates) which form the subsoil, presence of water courses and the proximity to the sea. The configuration of the valleys over time influenced the choice of installation positions of the residents. The shape of the two basins over time shows the suitability for inhabitation of the site and the construction of infrastructure.

REFERENCES

1 Betz, R., N.P. Hitt, R.L. Dymond, C.D. Heatwole, 2010. A method for quantifying stream network topology over large geographic extents. Journal of Spatial Hydrology, 10(1): 15-29.

2 Cherry J. F., Davis L. J., Demitrack A., Mantzourani E., Strasser F. T. Talalay E. L.,1998. Archaeological Survey in an Artifact-Rich Landscape: a Middle Neolithic Example from Nemea, Greece. American journal of Archaeology, 92: 159-176.

3 Herz N., Garrison G. E., 1998. Geological methods for Archaeology. Oxford University Press, pp. 3-14

4 History of Greek Nation. 1970-74. Volumes A, B, C1, C2, D, E. Athens Publishing Co. (in Greek)

5 Lekkas E., Lozios S., Skourtsos E., Kranis H., 1998. Floods, geodynamic environment and human intervention. The case of Corinth (Greece). Proceedings of the International Conference on Computer Simulation in Risk Analysis and Hazard Mitigation, pp. 135-145.

6 Miller S. G. 1990. A Guide to the Site and Museum. University of California press. Berkley.

7 Miller St., Bravo J., Kraynak L., Landon M. , Marchand J., 2005. Nemea Museum and Archaeological Site. Athens. (in Greek)

8 Ori G. G., 1989. Geologic history of the extensional basin of the Gulf of Corinth (Miocene – Pleistocene), Greece. Geology, 17(10): 918 – 921.

9 Papanikolaou D., 1986. Geology of Greece. University of Athens.

10 Pausanias Periegesis of Greece, “Corinth – Laconia”. 1976. Edited by N. Papachatzis. Athens Publishing Co.(in Greek)

11 Sakellariou M., Faraklas N., 1971. Corinthia - Cleonaea, Ancient Greek Settlements XI.

12 Seger M. & Alexander J., 1993. Distribution of Plio - Pleistocene and Modern coarse - grained deltas south of the Gulf of Corinth, Greece. Spec. Publs. Int. Ass. Sediment. vol. 20: 37-48.

13 Zelilidis A., 2000. Drainage evolution in a rifted basin, Corinth Graben, Greece. Geomorphology 35: 69-85.

PERSISTENT SCATTERERS INTERFEROMETRY FOR LANDSLIDE STUDY IN A SMALL SCALE INHABITED AREA

Parcharidis I.[1], Stamatopoulos C.[2]., Foumelis M.[3], Benekos G[1] Balla, L.[2]*

1. Harokopio University, Dep. of Geography, El. Venizelou 70, 17671, Athens, Greece, tel: +30 2109549345, e-mail: parchar@hua.gr, benekos@hua.gr
2. Stamatopoulos and Associates Co, Isavron 5, 11471, Athens, Greece, tel: +30 2103603911, e-mail: info@saa-geotech.gr
3. European Space Agency (ESA-ESRIN), Research and Development Section, Science, Applications and Future Technologies Dept., Frascati (Rome), tel: +30 0694188385, e-mail: michael.foumelis@esa.int

ABSTRACT

The aim of this study concerns the development a ground deformation monitoring based on PSI (Persistent Scatterers Interferometry) processing of radar data in order to predict and mitigate the risk of ground displacement cased by slope instability. The study area is located in Kerasia village at Plastiras Lake Municipality (Central Greece). The problem under treatment is a creeping landslide in an inhabited area. PSI processing using a data set of ERS-1/2 scenes for the period 1992-2000 was applied to retrieve the displacement history of the of the area for the considered time interval.

INTRODUCTION

Numerous phenomena can induce displacements of the earth surface and thus cause dislocations in structures and infrastructures particularly in urban areas. Landslides affect many areas of Greece and are characterized by low probability of evolution into a catastrophic event but can have very large direct and indirect impacts on man-made structures (1,2,3). Methodologies for the risk assessment and mitigation are therefore a major issue. Conventional methods of ground deformation monitoring, present many disadvantages such as high costs and time consuming. The space based Differential Interferometry Synthetic Aperture Radar (DInSAR) techniques could present a valuable tool for detecting, monitoring, quantifying the deformation and with field-work contribution can identify causes which may induce deformation. DInSAR has already proven its potential for mapping ground deformation phenomena, e.g. earthquakes, volcano dynamics, etc. and to cover in continuity large areas. In recent years the innovative Persistent or Permanent Scatterers Interferometry (PSI) technique (4,5), which overcomes several limitations of repeat-pass interferometry, has been widely applied for monitoring of slope instability with millimetric precision (6,7,8,9,10,11,12,13,14,15,16). According to this technique reliable deformation measurements can be obtained in a multi-image frame work on a small subset of image pixels corresponding to stable areas. These point-targets could be used to monitor terrain motion by analysing the phase history of each one. The response of clays along slip surfaces includes considerable strain softening at large displacement (17). The area of study is located in the region of the Municipal Department of Kerasia in Plastiras Municipality (Central Greece).

THE AREA OF INTEREST

The area of study is in the Kerasia village in Plastiras Municipality Figure 1. The problem under treatment is landslide in inhabited area. The broad area belongs to the lower part of Agrafa mountain range with an average altitude of 910 m. Average slope in this zone is of the order of 20% or 35%. The broad area is characterized by one of the highest rainfall-snowfall quantities in Greece; the average annual equivalent rainfall height is about 1200 mm with the 80% of this fall between months of October to April. The area of study is classified as belonging to Category II of

seismic action with ground acceleration A = a x g = 0.24 g. The area is characterized from a complex geological structure. It primarily consists of limestones, strata of the transitional type to flysch and the particular phases of flysch of the Olonos-Pindos zone. Intense tectonic deformation is observed. The typical geological profile consists of limestone bedrock, on which sandstone and clayey schist phases of flysch are deployed. Thus, slopes of the residential area consist principally from sediments of flysch. An upper completely weathered layer that is soil of clay, sand-clay and clay-sand composition and a lower mildly weathered layer of the formation are distinguished. The existence of many springs indicates a rich water load in the subsoil. Water moves both through the limestones and the flysch. The weathered zone and the fractured zone of flysch develop shallow depth and no permanent flow water tables and springs and surficial water tables and springs. The water from springs and outflows within the residential area usually move uncontrollably causing soil formations to saturate thus weakening their geomechanical behavior and developing excess pore water pressures.

Figure 1. Location of the study area showing in Google Earth environment

The nature of the movements are creeps, translatory slides (planar or either), rotational - cycloid slides, settlements, falls and mudflows. The phenomenon is known to occur since early in the last century and various reports refer to it. Landslides have caused ruptures in walls and floors of buildings, wall turnings, cracks on the road surfaces of the municipal road network, the creation of soil cracks, tilting and uprooting of trees Figure 2. As main causes of these phenomena, the following have been identified : (a) Steep morphological gradients, (b) nature of formations, thickness and the poor mechanical properties of surface materials in the weathered zone, recent refills etc. (c) Inadequate surface drainage, (d) soaking of loose materials by water from intense rainfalls, cultivation and irrigation of slopes during summer, leakages and the absence of a drainage system, (e) the absence or inadequate function of retaining measures, (f) insufficient foundations and age of houses that have been damaged, (g) undercuts and scouring.

Figure 2. Kerasia village photos showing damage at houses due to landslide

DATA AND METHODS

In this study SAR scenes from ERS-1 and 2 satellites operating in C-band were used. In total 29 Single Look Complex (SLC) scenes of VV polarization acquired in descending orbit (track: 279, frame: 2835) and covering the period 1992–2000 were utilized. Moreover, a Digital Elevation Model (DEM) produced by the Shuttle Radar Topography Mission (SRTM) of approximately 90 m spatial resolution was used for topography removal. Finally, precise orbit state vectors were ingested in processing to enhance the accuracy of the satellite's orbit and estimate the initial interferometric baselines. Specifically, for the ERS scenes, orbit data from DELFT Institute (NL) for Earth-Oriented Space Research (DEOS) (18) were obtained. The methodology that has been used in this study was basically the Persistent Scatterers Interferometry (PSI) based on the Interferometric Point Target Analysis (IPTA) algorithm of the GAMMA software suite. The IPTA is a toolbox that can support many different processing schemes including different techniques for candidate point scatterers selection, spatial and temporal phase unwrapping, etc. The first step of processing chain was the coregistration of the SLCs scenes to a common master geometry. For our dataset the scene of 23 Februry-1997 was selected as reference. The achieved coregistration accuracy was satisfactory with standard deviations of individual range and azimuth offsets from the offset regression fit, less than 0.3 pixels. Based on the coregistered SLCs scenes, two candidate lists of point scatterers (PSs) were initially generated using two different selection approaches. The first list was generated based on phase properties and the second based on low intensity variability as the intensity and phase depend on the point-target cross section and position. Then, the two candidate point lists were combined into a single one, which finally was used for the analysis. The IPTA methodology requires one single scene as reference in order to form multiple pairs and produce interferograms. The criteria by which the reference scene was selected were the following: (i) forming interferometric pairs with the minimum baseline (Bp), (ii) acquisition date near the central date of the time period for which there are available SAR acquisitions, and (iii) reference scene to present low atmospheric distortions. For the specific project the ERS scene acquired on 23 Februry-1997 was selected as reference scene. Afterwards the initial differential interferograms were generated using the coregistered SLCs, the DEM heights, and the preceding point lists. This is performed by simulation of the unwrapped interferometric phase based on the initial baselines and the DEM. Then, the differential interferograms were analyzed in the temporal and spatial domain in order to obtain information on the atmospheric phase term, deformation phase term, and baseline errors. Thus, processing proceeds by applying a least-squares regression on the differential phases in order to estimate terrain height and deformation rate relative to a reference point target. The selection of the reference point is considered to be the most critical part of the processing, as final deformation rates and histories are greatly affected by this decision. Some criteria for the selection of the reference point are dictated by the applied method, such as the high quality of the point in terms of phase stability overtime. Others are related to the regional geodynamic setting of the area and the related pattern of deformation which needs to be extracted. In this case the selected reference point-target is located at 561094.00 E, 4351207.50 N position, about 4.5 km towards southeast at Kalyvia village. Based on the regression analysis, the quality of the PS candidates was further evaluated through the estimated standard deviation of the phase difference. PSs with a phase standard deviation larger than the indicated threshold (in this case 1.0 radian), significantly reducing the number of points. The majority of the rejected points were located over mountainous areas. Moreover, because residual phases contain the atmospheric term, nonlinear deformation, and error terms, they were further processed in order to compensate atmospheric and noise effects. Thus, residual phases were spatially filtered by applying a low-pass spatial filter. Atmospheric and error terms were reduced by the spatial filtering around the reference points, assuming that stability occurred in the region of the area. Further iteration was done in order to improve the estimated error in the final regression model. The generated results consist of height corrections, linear deformation rates, atmospheric phase, refined baselines, temporal coherence, and nonlinear deformation histories for each scatterer. Finally the deformation phases were transformed into displacements and geocoded to the selected cartographic reference system (UTM projection, WGS'84 datum). Following the transformation of the interferometric

phases from range–Doppler coordinates into map geometry (geographic coordinates) PSs were imported into a GIS environment and plotted on a high-resolution Quickbird image in Google Earth environment. Finally, a total number of 223 scatterers for the time period 1992–2000 were identified with average annual motion about -1.37 mm/year and their density is approximately 60 points/km2 Figure 3 and the point scatterers motion statistics (mm/year classes) are shown in the Table 1.

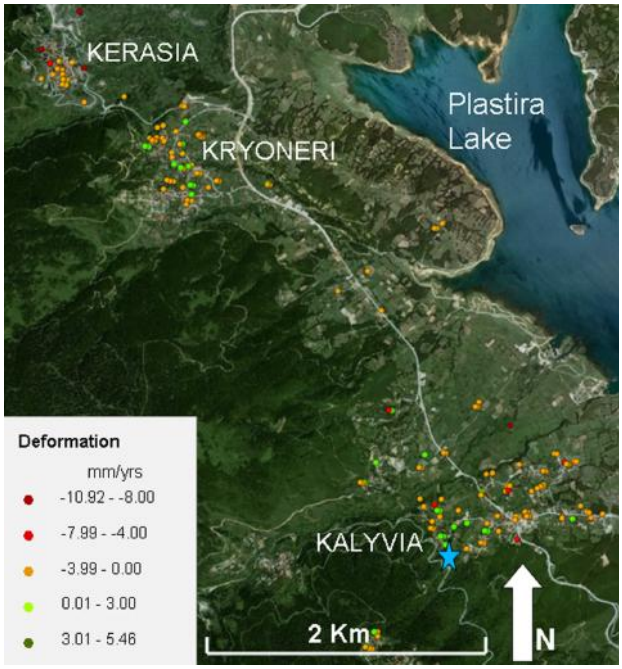

Figure 3. Point targets deformation map of the broader area produced by permanent scatterers interferometry method and plotted in Google earth environment. The blue star represents the reference point target.

Table 1: Point targets motion statistics

Point-target motion classes in mm/year	% of point-targets in each ass
>-3.5	8.09%
-3.5 to -1.5	36.77%
-1.5 to + 1.5	50.22%
+1.5 to + 3.5	4.48%
+3.5 to +max	0.44%

Within Kerasia village, where the study is focused, a number of 22scatterers was identified having average annual motion rates of -2.9 mm/year Figure 4. It is obvious that the majority of the scatterers show subsidence and are located within the settlement of Kerasia with major rates of deformation located in the northern part of the village.

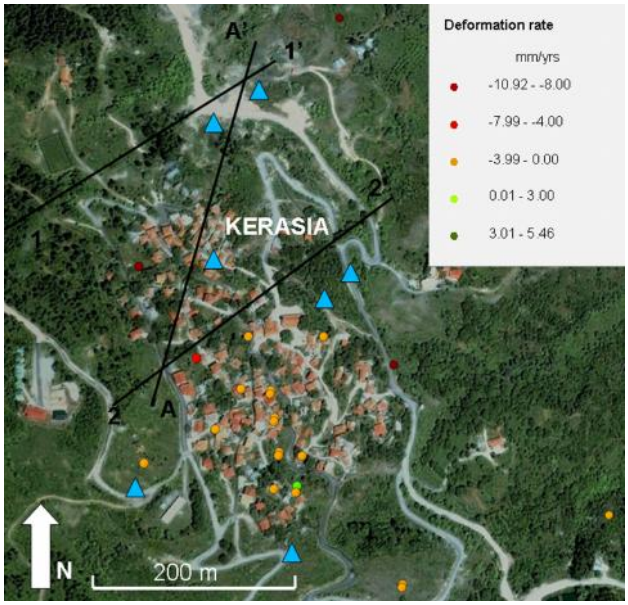

Figure 4. Point targets deformation map for Kerasia in Google Earth environment, the sections studied and location of boreholes (triangles).

RESULTS

The case of Kerasia in Plastiras Municipality as a continuous “creeping” slide is a typical example of all those phenomena that occur in Greek hilly and mountainous areas particularly in zones of considerable precipitation, triggered principally by water movement and favored by soil composition and stratification, weakness of surface formations, steep morphological gradients and not well studied human interventions. Many of them as in Kerasia go back for a long time in the past. There may be hundreds of similar cases developing in rural residential areas and many others may emerge in the near future. They affect houses and other structures which are most vulnerable since the overwhelming majority has not been built with modern codes and usually with no design at all. But they affect also utility networks (water, telephone lines, electricity etc.), roads, bridges and other infrastructure. Damage of roads is of particular concern because of their length of exposure and their function connecting different places. The social and economic impact of incurred loss and damages is apparent. This phenomenon can sharply increases and accelerates due to strong rain events or earthquake. In this case not only material damage is involved but risk for human lives too. Satellite data available, even though not many in this study, covering a certain period in the past (1992 to 2000) have been useful to indicate not only the location, but also the magnitude of sliding movements of an average rate of 8.4 mm/year. But the real importance of the access to these data is the acquired capability of using this technology in the future not only for the area of Kerasia but for many other areas too. By monitoring displacements and their rate variation due to slow soil motion from satellites focusing in areas where initiation of phenomenon is manifested or suspected and in other sites of significance, timely preparation for treating the problem can be ensured. This shall be of important social, economic and environmental benefit.

ACKNOWLEDGEMENTS

The present study was carried out within the frame of TERRAFIRMA-GMES (www.terrafirma.eu.com) ESA’s project. Authors would like to acknowledge European Space Agency for ERS-1/2 SLC radar scenes provision.

REFERENCES

1 Marinos, P., Kavvadas, M., Tsiambaos, G., Saroglou, H., 2002. Rock slope stabilization in Mythimna castle, Lesvos island, Greece. 1st European Conference on landslides, Balkema Publ., ed: Rybar Stembeck and Wagner, Prague, 635-639.

2 Sabatakakis, N., Koukis, G., Mourtas, D., 2005. Composite landslides induced by heavy rainfalls in suburban areas: City of Patras and surrounding area, western Greece. Landslides 2, 202-211.

3 Koukis, G., Sabatakakis, N., Ferentinou, M., Lainas, S., Alexiadou, X., Panagopoulos, A., 2009. Landslaide phenomena related to major fault tectonics: rift zone of Corinth Gulf, Greece. B. Eng. Geol. Envirn. 68, 215-229.

4 Ferretti, A., Prati, C., Rocca, F., 2001. Permanent scatterers in SAR interferometry. IEEE T. Geosci. Remote 39, 8–20.

5 Werner, C., Wegmüller, U., Strozzi, T., Wiesmann, A., 2003. Interferometric point target analysis for deformation mapping. In Proceedings of the IEEE International Geoscience and Remote Sensing Symposium, Toulouse, France, July 2003, 7, 4362–4364

6 Strozzi, T., Farina, P., Corsini, A., Ambrosi, C., Thüring, M., Zilger, J., Wiesmann, A., Wegmüller, U., Werner, C., 2005. Survey and monitoring of landslide displacements by means of L-band satellite SAR interferometry. Landslides 2 (3), 193–201.

7 Colesanti, C. Wasowski, J., 2006. Investigating landslides with space-borne Synthetic Aperture Radar (SAR) interferometry. Eng. Geol. 88, 173-199.

8 Rott, H., Nagler, T., 2006. The contribution of radar interferometry to the assessment of landslide hazards. Adv. Space Res. 37, 710-719.

9 Corsini, A., Farina, P., Antonello, G., Barbieri, M., Casagli, N., Coren, F., Guerri, L., Ronchetti, F., Sterzai, P., Tarchi, D., 2006. Space-borne and ground-based SAR interferometry as tools for landslide hazard management in civil protection. Int. J Remote Sens. 27(12), 2351-2369.

10 Bovenga, F., Nutricato, R., Refice, A., Wasowski, J., 2006. Application of multi-temporal differential interferometry to slope instability detection in urban/peri-urban areas. Eng. Geol. 88, 218-239.

11 Delacourt, C., Allemand, P., Berthier, E., Raucoules, D., Casson, B., Grandjean, P., Pambrun, C., Varel, E., 2007. Remote sensing techniques for analysing landslide kinematics : a review. B. Soc. Geol. Fr. 178, 2, 89-100.

12 Peyret, M., Djamour, Y., Rizza, M., Ritz, J.-F., Hurtrez, J.-E., Goudarzi, M, Nankali, H., Chery, J., Le Dortz, K., Uri, F., 2008. Monitoring of the large slow Kahrod landslide in Alborz mountain range (Iran) by GPS and SAR interferometry. Eng. Geol. 100, 131-141.

13 Meisina, C., Zucca, F., Notti, D. Colombo, A., Cucchi, A., Savio, G., Giannico, C. Bianchi, M., 2008. Geological interpretation of PSInSAR data at regional scale. Sensors 8, 7469-7492.

14 Castaneda, C., Gutierrez, F., Manunta, M., Galve J., 2009. DInSAR measurements of ground deformation by sinkholes, mining subsidence and landslides, Ebro River, Spain. Earth Surf. Proc. Land. 34, 1562-1574.

15 Del Ventisette, C., Casagli, N., Fortuny-Guasch, J., Tarchi, D., 2012. Ruinon Landslide (Valfurva, Italy) ctivity in relation to rainfall by means of GB-InSAR monitoring. Landslides 9, 497–509.

16 Lu, P., Stumpf, A., Kerle, N., and Casagli, N.: Object-oriented change detection for landslide rapid mapping, Geosci. Remote Sens. Lett., 8, 701–705, 2011

17 Stark, T.D., Contreras, I.A., 1996. Constant volume ring shear apparatus. Geotech Test J 19(1), 3-11.

18 Scharoo, R. Visser, P.N.A.M., 1998. Precise orbit determination and gravity field improvement for the ERS satellites. J. Geophys. Res. 103, 8113-8127.

LANDLSIDE INVENTORY USING A GISMA SYSTEM EXTENDED WITH STATISTICAL ADAPTIVE METHODS

Maria Kordoul[1], Katerina Kavoura[1], Konstantinos Nikolakopoulos[1]&NikolaosSabatakakis[1]

1. University of Patras, Department of Geology, Laboratory of Engineering Geology kordouli@upatras.gr, kavoura@upatras.gr, knikolakop@upatras.gr,sabatak@upatras.gr

ABSTRACT

The development of Internet technologies and applications of global geographic maps such as Google Maps have given a rapid development in the field of Geographic Information Systems (GIS). New models have been already studied like the GISMA (Geographic Information System Multi Administration) where the information's administrated from multiple users from different places of the world. In these systems it is important the information security, and the possibility of extensibility, the ability of self-management and self-development of the system. Thus, each user must have specific rights, can receive results from different mathematical and statistical methods, can update or not the data etc.

In this work we present a GISMA system that has been developed to manage information for Landslides in the region of Achaia. This system follows the basic principles of GISMA. The system has the ability to display information on Google Maps in order to displays the information anywhere in the world via internet. Authorized users in different places of the world, depending of their rights can enter data in the system, can enter new mathematical and statistical processes in order to analyze the data, and addition can add new tables and fields in the database for more complex analyzes. Finally, the implementation and evaluation of the system showed that GISMA systems are a flexible solution where GIS systems handle several users as research systems, system for Business Administration, or Government Organizations.

INTRODUCTION

Internet GIS utilize network communications to disseminate or to access geographic information. Different Internet GIS applications may need different kind of network environments for their specific purposes. The development also of Internet technologies and applications of global geographic maps such as Google Maps have given a rapid development in the field of Geographic Information Systems (GIS).Geographic information system (GIS) (Clarke 1986) is a system designed to capture, store, manipulate, analyze, manage, and present all types of geographical data. The acronym GIS is sometimes used for geographical information science or geospatial information studies to refer to the academic discipline or career of working with geographic information systems. In the simplest terms, GIS is the merging of cartography, statistical analysis, and database technology.

New models have been already studied like the GISMA (8) (Geographic Information System Multi Administration) where the informations administrated from multiple users from different places of the world. In these systems it is important the information security, and the possibility of extensibility , the ability of self-management and self-development of the system. Thus, each user must have specific rights, can receive results from different mathematical and statistical methods, can update or not the data etc.

The aim of GISMA (Geographic Information System Multi Administration) is to manage geographical information from multiple sources. In GISMA, the data input, controlled and updated by different users. Users can be located either in the same area or a different area. (8)

In GISMA the users have specific permissions of use of data as the administrator sets. So, the users can input information, take statistical or other results, update data e.t.c., or some of them as their permissions allow.

The GISMA systems can be applied to administrative services, scientific applications, general applications of information where the information is managed directly correlated with topological data (coordinates in space) while simultaneously managing the volume of information and knowledge of these have multiple supply points.

In this work we present an new GISMA system a well-documented landslide inventory of the studied area including the mapping of past and recent slope movements, together with the identification and mapping of the predisposing factors of slope instability. The data of the system include (a) past landslide occurrences and existing information on mass movements (historical catalogue) based on historical archives (review of scientific studies, technical reports, geological map descriptions, file reports, university theses, newspaper clippings etc) and (b) recent landslide occurrences based on a systematic interpretation of satellite images and aerial photographs.

The data presents on several google maps, and the user can select records using geographical queries. This GISMA system was installed in a Web Server with 1TB storage space and a bandwidth 50MBps. 20 users use this system and we test it using different procedures. The volume of information that was applied was 120 MB. The behaviour of the system was quite satisfactory (maximum time of access, insert, update and delete records was 2sec).

METHODS

Landslide Inventory Form

The primary requirement in predicting future landslides is a well documented landslide inventory of the studied area including the mapping of past and recent slope movements, together with the identification and mapping of the predisposing factors of slope instability. This constitutes the basic concept of landslide susceptibility which includes the spatial distribution of factors related to the instability processes in order to estimate zones of landslide – prone areas without any temporal implication(1,2,3).

In this work a Landslide Inventory Form was used for data codification mainly based on landslide report (12), summary (13) and glossary (14) including the former suggestions regarding landslide causes (15) and rate of movements (16).

It also noted that Landslide inventory derived from historic archives is usually unrepresentative as regards its spatial distribution. This is because the landslide data recorded and obtained by the Authorities (Public Organizations) constitute only cases that have affected residential areas and road network causing financial damages with serious socio – economic consequences. Landslides that occurred in uninhabited areas without causing damages, usually no recorded. In order to include all that occurrences, a systematic interpretation of satellite images and aerial photographs is needed. That means an inventory form suitably designed to include the obtained remote sensing information.

The inventory form shown in Fig. 1 was appropriately designed (11) to include all the required information obtained from the above mentioned different data sources.

GISMA (Geographic Information System Multi Administration)

The aim of GISMA (Geographic Information System Multi Administration) is to manage geographical information from multiple sources. In GISMA, the data input, controlled and updated by different users. Users can be located either in the same area or a different area. (8)

In GISMA the users have specific permissions of use of data as the administrator sets. So, the users can input information, take statistical or other results, update data e.t.c., or some of them as their permissions allow.

<table>
<tr><th colspan="6">Landslide Inventory Form</th><th colspan="2">Inventory Number: 214</th></tr>
<tr><td rowspan="2">Landslide location (Region, Municipality, city – village, area)</td><td colspan="5" rowspan="2">Western Greece, Achaia, Patras, Platani village</td><td colspan="2">Coordinates</td></tr>
<tr><td>lat (°)</td><td>long(°)</td></tr>
<tr><td></td><td colspan="5"></td><td>38°17'42''N</td><td>21°49'45''E</td></tr>
<tr><td>Land – use:</td><td colspan="2">Agriculture</td><td colspan="2">Crown elevation (m):</td><td colspan="2">280</td></tr>
<tr><td>Date of landslide:</td><td colspan="2">22 February 1999</td><td colspan="2">Date of observation:</td><td colspan="2">23 February 1999</td></tr>
<tr><td colspan="2">Ground slope before landslide (degrees):</td><td>30°</td><td colspan="2">Slope orientation:</td><td colspan="2">N30E</td></tr>
<tr><td rowspan="2">Dimensions of landslide:</td><td>length (m):</td><td>300</td><td>width(m):</td><td>190</td><td>depth(m):</td><td>5 – 10</td></tr>
<tr><td>crown length(m):</td><td>120</td><td>volume(m^3):</td><td>210×10^3</td><td>area (m^2):</td><td>28×10^3</td></tr>
<tr><td>Rate of movement:</td><td colspan="2">10 m/day</td><td colspan="2">Orientation of movement:</td><td colspan="2">N50W</td></tr>
<tr><td>Landslide type:</td><td colspan="6">Composite (translational – rotational)</td></tr>
<tr><td>Geology (lithology – structure – weathering)</td><td colspan="4">Plio-Pleistocene stiff clayey marls (CL) and clayey sands (SC). Weathered zone mixed with recent materials.</td><td>mantle thickness (m):</td><td>3 – 5</td></tr>
<tr><td rowspan="2">Landslide causes:</td><td>Triggering</td><td colspan="5">intense and prolonged rainfall</td></tr>
<tr><td>Preparatory</td><td colspan="5">ground conditions, human causes (excavations, loading)</td></tr>
<tr><td>Impacts to:</td><td colspan="6">Residential (one two-story house destroyed), road (failures in cutting slopes 130 m long and in an embankment 90 m long)</td></tr>
<tr><td colspan="2">Landslide reported by (organization):</td><td colspan="5">Region of Western Greece</td></tr>
</table>

Figure 1. Landslide inventory form completed with a recorded occurrence (Sabatakakis et al 2013)

The GISMA systems can be applied to administrative services, scientific applications, general applications of information where the information is managed directly correlated with topological data (coordinates in space) while simultaneously managing the volume of information and knowledge of these have multiple supply points.

It is obvious that in GISMA there are two requirements:

1. The primary knowledge is in different places - users.
2. Data may be administered from various locations

The previous two requirements lead us to the following necessities:

1. Access to the GISMA application from different access points
2. Access and management of the application by different authorized users
3. Distinction between primary users in recording and updating information and administration-management users
4. Control whether the information is valid
5. Ability to collect information and process it according to the requirements of the central administration bodies.
6. The systems must be compatible to possible changes in system requirements

The above necessities give the following principles:

(a) Principle of Multiple Access (b) Principle of identity of the information (c) Principle of Role Graduation (d) Principle of Remote-Controlled Access (e) Principle of valid Information (f) Principle of Security (g) Principle of Adaptability/Compatibility

In this study we implement a GISMA in order to record Landslide inventory of various areas. The system gives the opportunity to use many different researchers to enter information, obtain Geographical projections through different geographical queries, and use all be done from anywhere in the world anytime using internet technologies.

RESULTS

The introduction screen of the user is the Fig 2. The user gives username and password and according to his right which gives the administrator can enter new records, update, delete data. The user also cancreate or import new forms of recording, new fields in existingforms.

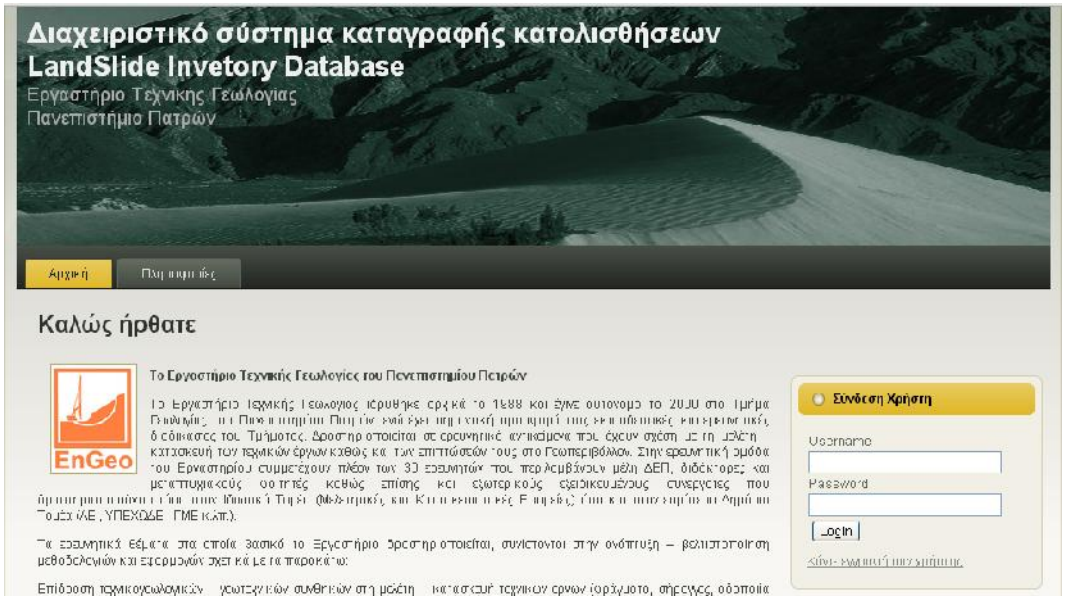

Figure 2. Introduction Screen. User gives username and password in order to have access in GISMA.

All the user can give geographical queries and take the geographical views that they want. Administrators can manage users, give those rights and control the overall system.

This GISMA system was installed in a Web Server with 1TB storage space and a bandwidth 50MBps. For this implementation we use PHP, MYSQL and many parts of Javascript and JQUERY (7).

The GISMA system follows all the basic principles of GISMA as described previously.

The system testing with the follow amount of users

- 20 Ordinary users
- 5 Registrars
- 5 Information managers
- 1 Guarantor
- 1 System Administrator

The volume of information that was applied was 200 MB.

The behaviour of the system was quite satisfactory (maximum time of access record was 2sec).

In Fig 3 the user can use the form of the GISMA which designed as the inventory form of Sabatakakis et al 2013. Administrator can design with a very easy way every form that is necessary for the system and add, delete or change fields in already designed forms.

Figure 4 show the screen that the administrator can create, update or delete fields in a form.

Figure 5 show the screen of a geographical google map that present a geographical query that a user gives. In this figure the user ask to take all the records of landslides inventory of Achaia.

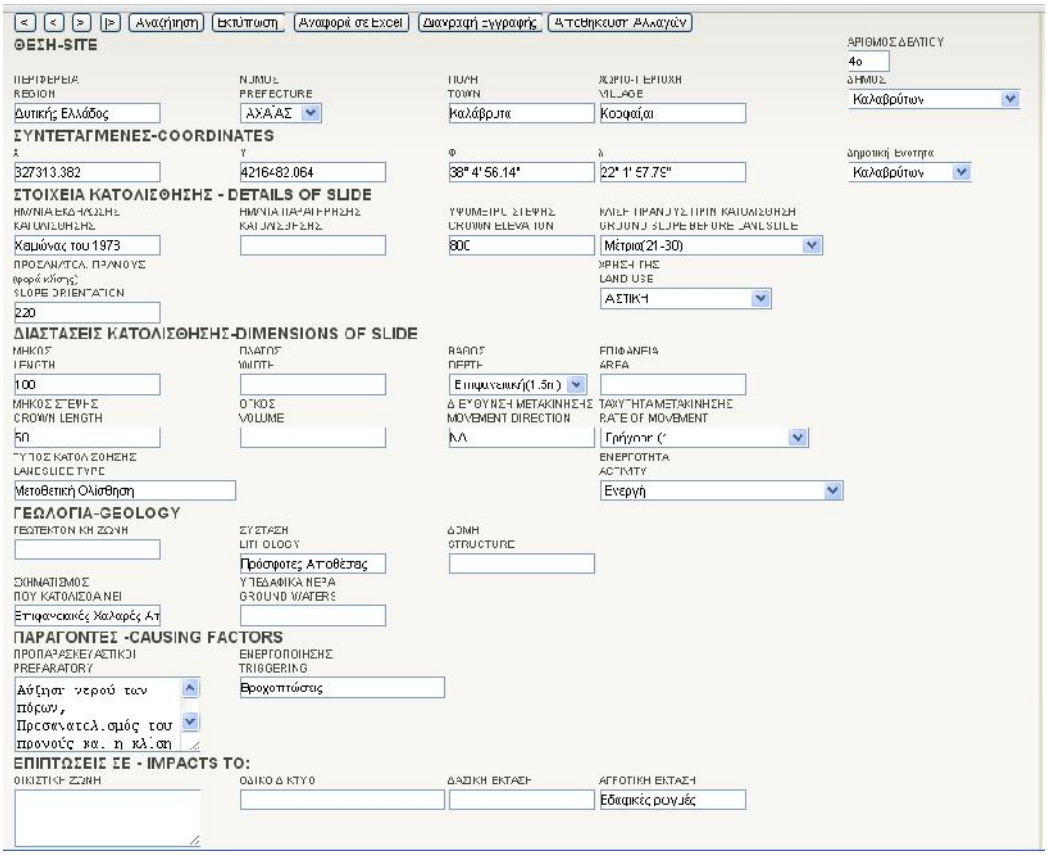

Figure 3. Landslide inventory form in GISMA completed with a recorded occurrence

CONCLUSIONS

In this study we created GISMA system already include over than 200 landslide cases occurred in Achaia, Ilia Prefecture which have been selected as “pilot study”. The system was properly designed to record and manage information from multiple users such as undergraduate, postgraduate students and other researchers of Patras University It also constitutes the basic tool for inventory-based, probabilistic approaches for landslide susceptibility zonation mapping. The system present the data on a google map and the users can select records using geographical queries. The system

Landslide occurrences are generally governed by numerous spatial predisposing factors that can be, for the purpose of susceptibility assessment, recorded and storage using a regional inventory. A reliable and accurate susceptibility assessment strongly depends on the proper identification and selection of these factors, while the inclusion or omission of some may change significantly the capability of that assessment.

A landslide inventory is usually derived from historical archives, meaning that is unrepresentative of the real spatial distribution, but also from systematic interpretation of satellite images and aerial photographs. The proposed inventory form in this work can be attempted through both sources of existing information on mass movements including historical and remote sensing data.

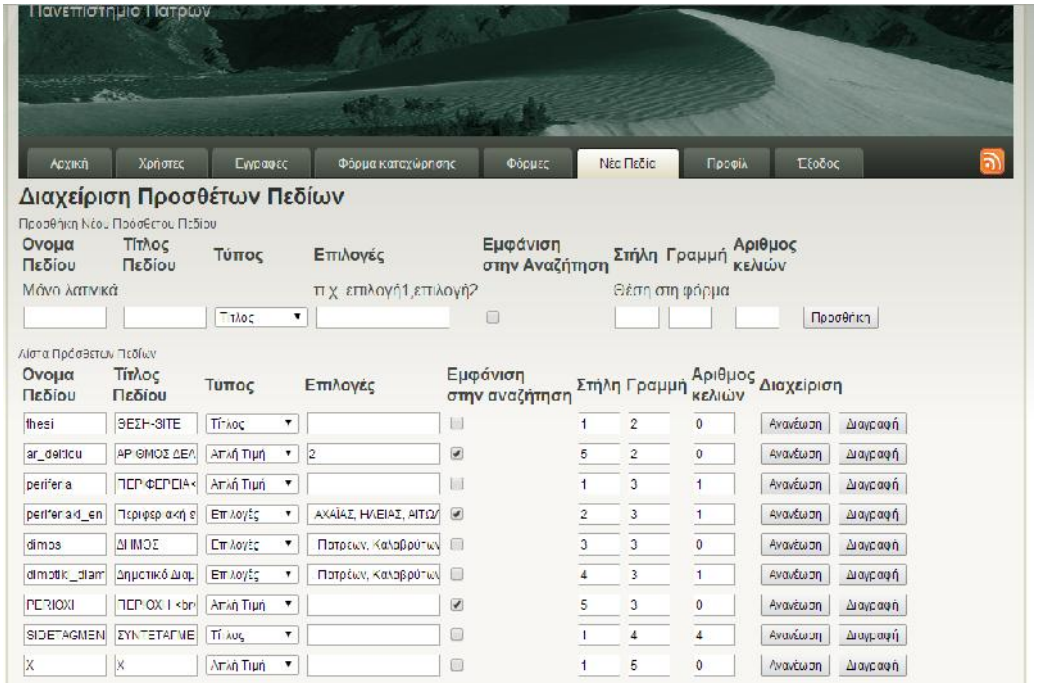

Figure 4 Landslide inventory form in GISMA completed with a recorded occurrence

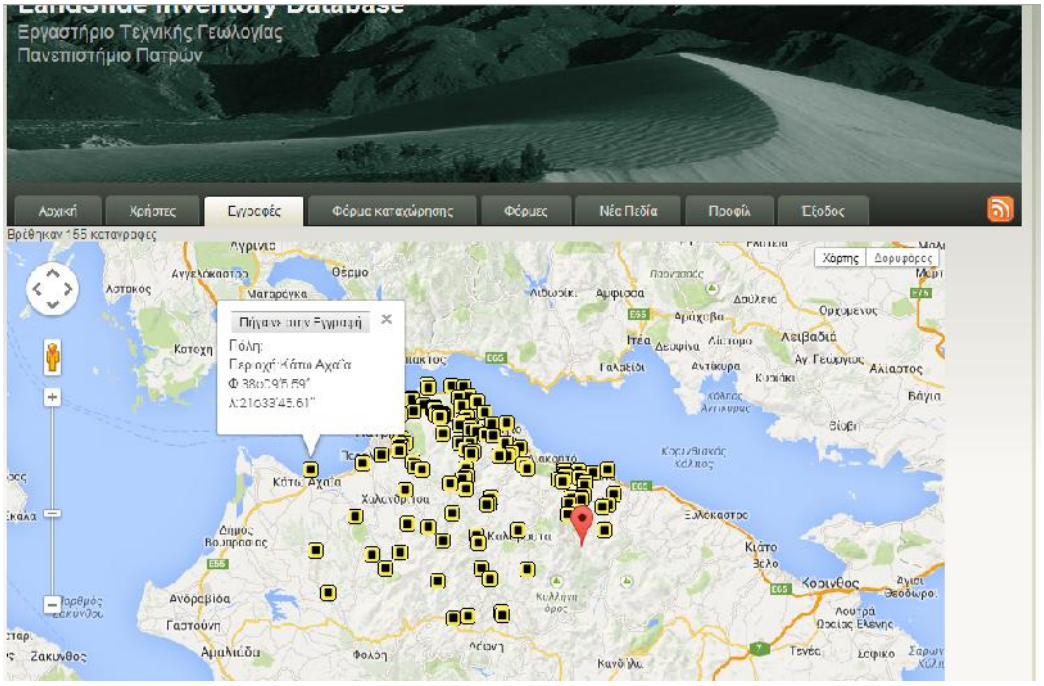

Figure 5 show the screen of a geographical google map that present a geographical query that a user gives. In this figure the user ask to take all the records of landslides inventory of Achaia.

The GISMA systems can be applied to administrative services, scientific applications, general applications of information where the information is managed directly correlated with topological data (coordinates in space) while simultaneously managing the volume of information and knowledge of these have multiple supply points. GISMA are the most appropriate systems for recording landslides inventories.

REFERENCES

1 Ayalew L, Yamagishi H, Ugawa N, 2004. Landslide susceptibility mapping using GIS-based weighted linear combination, the case in Tsugawa area of Agano river, Niigata Prefecture, Japan. Landslides 1:73–81. doi:10.1007/s10346-003-0006-9

2 Chau KT, Chan JE 2005. Regional bias of landslide data in generating susceptibility maps using logistic regression: case of Hong Kong Island. Landslides 2:280–290. doi:10.1007/s10346-005-0024-x

3 Chacón J, Irigaray C, Fernández T, El Hamdouni R 2006. Engineering geology maps: landslides and geographical information systems. Bull Eng Geol Environ 65:341–411. doi:10.1007/s10064-006-0064-z

4 Clarke C., 1986. Advances in geographic information systems, computers, environment and urban systems, Vol. 10, pp. 175–184.

5 Dobrovolny E 1971. Landslide susceptibility in and near Anchorage as interpreted from topographic and geologic maps. In: The great Alaska earthquake of 1964-Geology volume. Publication 1603. U.S. Geological Survey Open-File Report 86-329, National Academy of Sciences, USA, pp 735–745.

6 Foresman T. 1997. The History of GIS (Geographic Information Systems): Perspectives from the Pioneers. (Prentice Hall Series in Geographic Information Science) Prentice Hall PTR; 1st edition (November 10, 1997), 416 p.

7 Kerner M. 2008. "PHP 4 is Dead—Long Live PHP 5". InternetNews. Retrieved 2008-03-16.

8 Kordouli M., Kavoura Kat., Nikolakopoulos K., Sabatakakis N. LANDSLIDE INVENTORY USING GISMA TECHNIQUES, 13o International Congress of Geological Society of Greece, 5-8 September, Chania, Greece

9 Fernández T, Irigaray C, El Hamdouni R, Chacón J (2003) Methodology for landslide susceptibility mapping by means of a GIS: application to the Contraviesa Area (Granada, Spain). Nat Hazards 30(3):297–308. doi:10.1023/B:NHAZ.0000007092.51910.3f .

10 Finley K., 2011. "7 Cloud-Based Database Services". ReadWriteWeb. Retrieved 9 November 2011.

11 Sabatakakis N., Koukis G., Vassiliades E., Lainas S. (2013): _«Landslide susceptibility zonation in Greece»_. Natural Hazards 65(1):523 - 543. doi: 10.1007/s11069-012-0381-4.

12 WP/WLI 1990. A suggested method for reporting a landslide. International Geotechnical Societies' UNESCO Working Party on World Landslide Inventory (Chairman D Cruden) Bull Eng Geol Env 41(1):5–12. doi:10.1007/BF02590201

13 WP/WLI 1991 A suggested method for a landslide summary. International Geotechnical Societies' UNESCO Working Party on World Landslide Inventory (Chairman D Cruden) Bull Eng Geol Env 43:101–110. doi:10.1007/BF02590177

14 WP/WLI 1993. Multilingual landslide glossary. International Geotechnical Societies' UNESCO Working Party on World Landslide Inventory (Chairman D Cruden). BiTech, Richmond, p 59

15 WP/WLI 1994. A suggested method for reporting landslide causes. International Geotechnical Societies' UNESCO Working Party for World Landslide Inventory (Chairman ME Popescu) Bull Eng Geol Env 50(1):71–74. doi:10.1007/BF02594958

16 WP/WLI 1995. A suggested method for describing the rate of movement of a landslide. International Geotechnical Societies' UNESCO Working Party for World Landslide Inventory (Chairman ME Popescu) Bull Eng Geol Env 52(1):75–78. doi:10.1007/BF02602683

INVESTIGATING STRONG MINING-INDUCED GROUND SUBSIDENCE WITH X-BAND SAR INTERFEROMETRY IN UPPER SILESIA IN POLAND

Maria Przylucka[1], Marek Graniczny[2], Gerardo Herrera[3]

1. Polish Geological Institute – National Research Institute, Warsaw, Poland, maria.przylucka@pgi.gov.pl
2. Polish Geological Institute – National Research Institute, Warsaw, Poland, marek.graniczny@pgi.gov.pl
3. Geohazards InSAR laboratory and modeling group – Instituto Geológico y Minero de España, Madrid, Spain, g.herrera@igme.es

ABSTRACT

The Upper Silesian Coal Basin is one of the biggest coal basins in Europe located in southern Poland. Underground exploitation of coal deposits causes changes in the rock mass and terrain surface. The mechanical strength of the rocks is reduced and as a consequence surface deformation occur. Deformation after a single wall excavation forms a basin on the ground that can be 0,75 to 2,0 m deep. Hence, several mining works operated at different depths produce a total ground surface displacement of several meters. For this reason, there are many places in USCB urban areas where damages are important. Bytom city is one of such examples, where coal has been exploited science 1902. The city suffers mining subsidence, producing damages to linear structures like roads, railways, gas and water pipelines, electric power lines and buildings. Different methods are used for evaluating hazards caused by deep hard coal mining. These methods include mostly geodetic surveying and GPS measurements. Satellite Synthetic Aperture Radar Interferometry (InSAR) data can successfully complement geodetic measurements providing displacement measurements of wide areas. In this work 30 TerraSAR-X satellite images acquired during the period 05/07/2011 to 21/06/2012 were used. X-band wavelength proved to be very helpful tool for investigating very fast movements, directly connected with underground mining activity. Ground surface displacement data was retrieved from both conventional (DInSAR) and advanced differential interferometry (A-DInSAR), also called permanent scatterers interferometry (PSI). Differential interferograms helped to detect and measure ground surface displacement of the subsidence basins, reaching up to few decimetres in a few months, equivalent to 1-2 meters/year. Completing these measurements, PSI technique provided measures of 14 cm/year maximum, permitting to define the boundaries of the area affected by mining subsidence. As a result, both methods of displacement measurement permitted to estimate the total mining subsidence affecting Bytom city in period 07.2011-06.2012.

INTRODUCTION

The extraction of underground ore material through mining activities is usually associated with major geological, hydrogeological and geochemical impact on the environment. One particular phenomenon that may cause extensive damage to houses and infrastructure is surface deformation. It is therefore necessary to monitor ground movements, in order to detect and prevent potential damages to urban structures and infrastructures.

In Poland Upper Silesian Coal Basin (USCB) is one of the biggest coal basins in Europe. Hard coal underground exploitation has been conducted since the XIX century [1]. Nowadays, there are thirty active hard coal mines, where longwall mining typically operate at depths ranging from a few meters to more than 1000m [2]. Ground surface deformations triggered by underground mining activities reach several meters in USCB [2]. In this work we focus on Bobrek-Centrum mine due to its impact in Bytom urban area (area outline in red in Fig. 1).

Leveling is the most popular subsidence monitoring method used in USCB. The main limitation of field-based monitoring techniques, such as leveling, is the need of frequent field observations in time and in space, which will increase the monitoring cost. This limitation can be overcome by Synthetic Aperture Radar Interferometry (InSAR) [3]. By systematic large-scale coverage, high spatial and temporal resolution, InSAR provide the ability to detect from decimeter to millimeter scale surface deformation. The technique is based on the phase difference measurement between two SAR images. Differential SAR interferometry (DInSAR) removes the topographic phases with an external digital elevation model, in order to measure ground surface displacement. DInSAR main limitation is the radar signal decorrelation in time that will prevent DInSAR from successfully measure ground surface displacement [8]. Decorrelation can be due to atmospheric artifacts, land cover or even the velocity of ground surface displacement. One of the techniques developed to partially overcome these disadvantages is Persistent Scatterers Interferomery (PSI) [4]. By processing a set of interferograms, slow deformation over a long time span is detected on selected pixels called “persistent scatteres” (PS). SqueeSAR algorithm is an evolution of PSI, where a greater amount of PS, or distributed scatterers (DS) are detected, increasing the number of displacement measurements. The details of the techniqures can be found in the literature, e.g. for DInSAR processing: [3], for PSI [4] and for SqueeSAR [5]. Several authors have studied aplications of InSAR for mining inducted surface subsidence monitoring, e.g. [6], [7], [8] and [9]. USCB was the subject of similar studies [10], [11] and [12]. The objective of this paper is to show the result of combining displacement data derived from DInSAR interferograms and SqueeSAR algorithm over Bytom urban area. For this purpose high resolution radar satellite images acquired by TerraSAR-X SAR images were used. The basic characteristics of TSX satellite can be found in [13]. Maximum detectable deformation is constrained by its 3 cm wavelength that permits to detect, at least from a theoretical point of view, up to 1.5 cm between two neighboring pixels of a differential interferogram, which is generated from two TSX satellite SAR images. Similarly, the SqueeSAR maximum theoretical detectable displacement will be 245 mm/yr. Taking into account that underground longwall mining exploitation may produce centimetric to metric subsidence per day, we will assess throughout this work the limits of TSX radar interferometry to monitor fast mining subsidence.

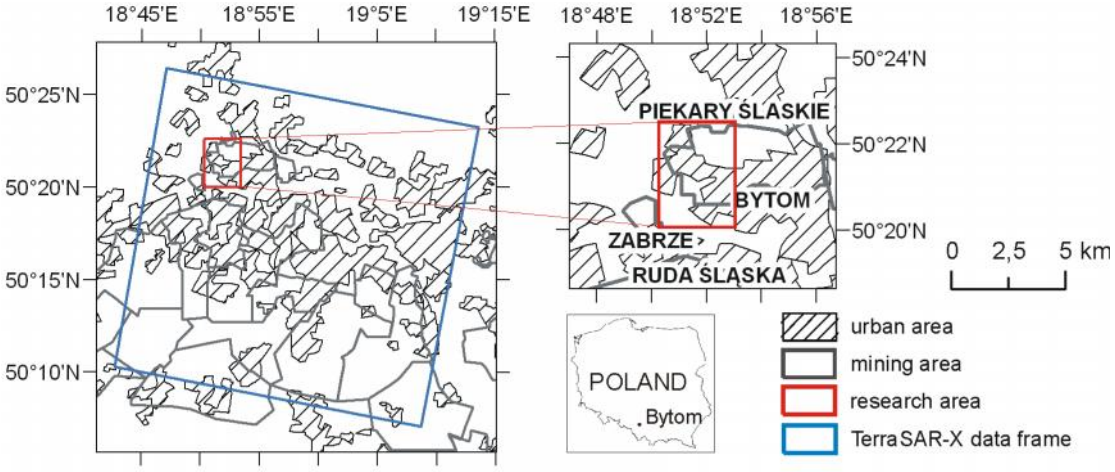

Fig. 1 Geographical location of the study area.

RESULTS

SAR data and DInSAR processing

Conventional DInSAR and SqueeSAR techniques were used to process 30 descending high resolution SAR satellite TerraSAR-X scenes acquired in strip map mode between the 5th July 2012

and the 21st June 2012. The study area, about 500 sq km, includes Tarnowskie Gory (NW), Dabrowa Gornicza (NE), Zabrze (SW) and Sosnowiec (SE) cities. A single master image from 1st October 2011 was selected for corregistration, generating 28 interferograms with perpendicular baseline smaller than 285 m and 11 days temporal baselines. The same dataset was process with SqueeSAR resulting in 1,7 Mln of PS for the whole dataframe, measuring velocities between -338 and 68 mm/yr. A ramp oriented south to north was removed from the PSI dataset through a multiple regression analysis using the least squares method. This work will focus on a subset of the whole dataset on Bytom area consisting of 28297 PS over 18 sq km. Fig. 2 a-d presents four out of twenty eight interferograms over Bytom area, where several deformation signals or subsidence basins are evident (black lines). However, the phase noise effect, most probably due to the very fast movement, is evident in the central part of subsidence basins. According to SqueeSAR results measured total displacement varies between +22 and -131 mm (Fig. 2e). In this figure it is evident that the absence of measurements in the central part of the subsidence troughs is due to the fast mining subsidence.

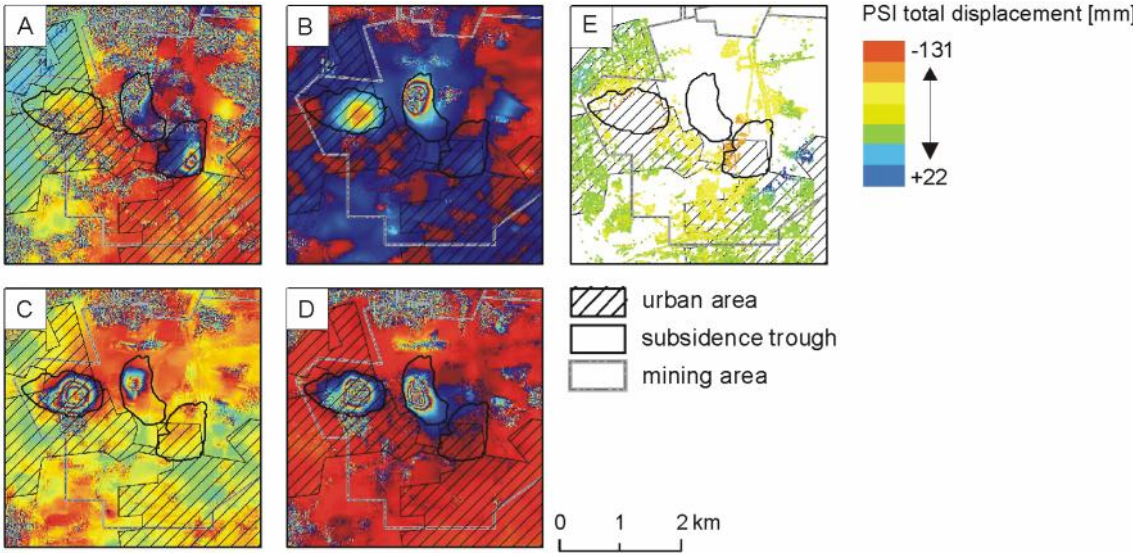

Fig. 2 Dataset used for the analysis. A-D. Examples of four out of twenty eight differential infetrferograms. The start and end dates of the interferograms: A. 18.08.2011-29.08.2011, B. 14.11.2011-25.11.2011, C. 17.12.2011-28.12.2011, D. 05.04.2012-16.04.2012. E. Values of total displacement of PSI points displayed in a colour scale, where red-yellow colours refer to subsidence, green stability and blue uplift. Three black polygons are borders of indentified subsidence troughs.

Subsidence activity maps

Subsidence activity maps were obtained through the integration of differential interferograms and SqueeSAR displacement measurements. Differential interferograms were analysed to compute displacements based on interferometric fringes count (Fig. 3). In some of the interferograms up to 5 fringes were visible, which is equivalent to 6 cm of deformation in 11 days (200 cm/yr). In order to calculate total mining subsidence, estimated displacements on every interferogram were added (Fig. 4b). The results suggest that for the longwall mining activity, surface deformation reached a maximum of 54 cm in the subsidence basin during the period 07.2011-06.2012.

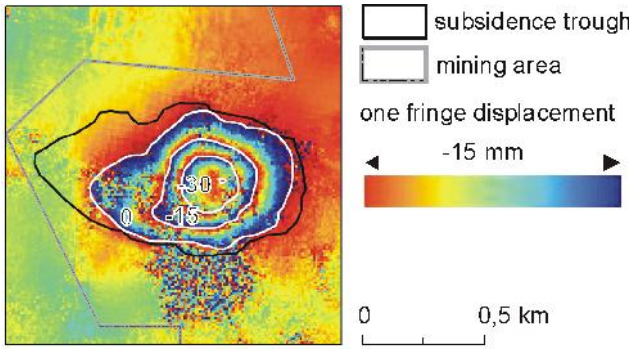

Fig. 3 Miechowice area on the interferogram from 17.12.2011-28.12.2011. An example of manual digitalization of subsequent fringes (white lines).

SqueeSAR displacement results were analysed to define residual mining subsidence influence area, i.e. the boundary between slow motion and stable areas. For this purpose over 28 thousand of PS points were interpolated, resulting on a continuous 50 m raster with cumulated subsidence values below 13 cm during the observation period (Fig. 4a). The combination of both generated results, permitted to map slow and faster movements together (Fig. 4c). In this map green colour depicts stable area, blue depict small uplift and yellow-orange-red colour depict subsidence. A large region around the subsidence troughs is affected by a residual subsidence 5 mm and 5 cm per year (yellow). A greater subsidence up to 13 cm is defined on the boundaries of the subsidence basins, reaching up to 54 cm in the central part. The positive displacement or uplift shown in the south-west could be related to rise of groundwater level after abandonment of underground mining activity. It should be noted that formation of subsidence troughs induced by underground excavation works assumes the largest vertical deformation in the middle of the basin, being gradually reduced towards the borders.

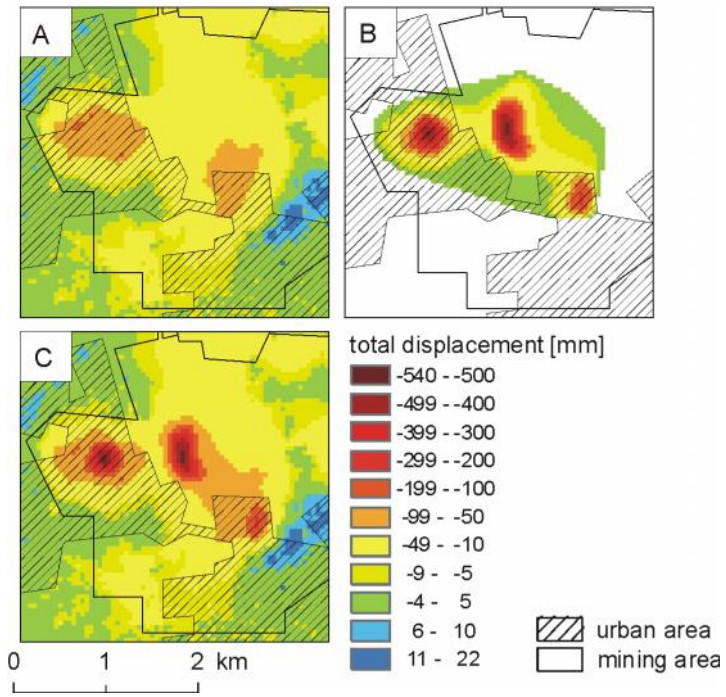

Fig. 4 Resulting total displacement maps with 50m pixel resolution. A. Interpolation of PSI points. B. Summed total dispalcemened indentified on the differential interferograms. C. Interpolation of both kind of information: PSI and interferograms.

CONCLUSIONS

Results obtained in this study show that the combination of DInSAR displacement measurements derived from conventional DInSAR and SqueeSAR exploitation of high resolution TerraSAR-X satellite images, can significantly improve the monitoring of mining subsidence areas affected by fast displacement patterns. The final result benefits from TerraSAR-X short revisit cycle and high resolution, permitting to successfully measure up to 54 cm/yr, as well as residual subsidence and uplift occurring in the surroundings of subsidence basin. Further studies should consider improving geostatistical processing and combination with ground truth data.

ACKNOWLEDGEMENTS

Processing of SAR images was done within Doris project, co-founded by European Commission under FP7/2007-2013 Grant Agreement n. 242212 by Tele-Rilevamento Europa - T.R.E. s.r.l. form Italy.

REFERENCES

1 Konopko W., 2010. Wydobycie węgla i destrukcja górotworu w Górnośląskim Zagłębiu Węglowym (ang. Coal output and rock mass destruction in Upper Silesian Coal Basin), Przegląd Górniczy, Stowarzyszenie Inzynierów i Techników Górnictwa, T. 66 no 11, 1-10.

2 Dobak P., Dragowski A., Frankowski Z., Frolik A., Kaczynski R., Kotyrba A., Pininska J., Rybicki S., Wozniak H., 2009. Zasady dokumentowania warunków geologiczno-inżynierskich dla

celów likwidacji kopalń (eng. Policy document of engineering-geological conditions for mine closure), (only in Polish) 12-14, Polish Ministry of Enviroment, Warsaw, pp. 84.

3 Massonnet, D. and Feigl K. L. 1998. Radar interferometry and its applications to changes in the Earth's surface, Rev. Geophys., 36, 441– 500.

4 Ferreti A., Prati C., Rocca F. 2001. Permanent Scatterers in SAR Interferometry, IEEE Transactions on Geoscience and Remote Sensing, vol. 39: 8-20.

5 Ferretti A., Fumagalli A., Novali F., Prati C., Rocca F., Rucci A., 2009b. The Second Generation PSInSAR Approach: SqueeSAR, Presented at Fringe Conf. 2009 Frascati.

6 Herrera G., Tomas R., Lopez-Sanchez J. M., Delgado J., Mallorqui J.J., Duque S., Mulas J., 2007. Advanced DInSAR analysis on mining area: La Union case study (Murcia, SE Spain), Engineering Geology 90 (2007), pp.148-159.

7 Liu, D., Shao, Y., Liu, Z., Riedel, B., Sowter, A., Niemeier, W., & Bian, Z. 2014. Evaluation of InSAR and TomoSAR for Monitoring Deformations Caused by Mining in a Mountainous Area with High Resolution Satellite-Based SAR. Remote Sensing, *6*(2), 1476-1495.

8 Engelbrecht, J., & Inggs, M., 2013. Differential interferometry techniques on L-band data employed for the monitoring of surface subsidence due to mining. South African Journal of Geomatics, *2*(2), 82-93.

9 Samsonov, S., d'Oreye, N., & Smets, B., 2013. Ground deformation associated with post-mining activity at the French–German border revealed by novel InSAR time series method. International Journal of Applied Earth Observation and Geoinformation, *23*, 142-154.

10 Perski, Z., 1998. Applicability of ERS-1 and ERS-2 InSAR for land subsidence monitoring in the Silesian coal mining region, Poland. International Archives of Photogrammetry and Remote Sensing, *32*, 555-558.

11 Popiołek, E., Hejmanowski, R., Krawczyk, A., & Perski, Z., 2002. Application of Satellite Radar Interferometry to the examination of the areas of mining exploitation. Surface Mining Braunkhole & Other Minerals, *54*(1), 74-82.

12 Graniczny M., Kowalski Z., Leśniak A., Czarnogórska M., Piątkowska A., 2007. Analysis of the PSI data from the Upper Silesia – SW Poland. The International Geohazard Week 5–9 November 2007 ESA-ESRIN Frascati Rome, Italy. The International Forum on Satellite EO and Geohazards: 17

13 Eineder, M., Runge, H., Boerner, E., Bamler, R., Adam, N., Schättler, B. & Suchandt, S., 2003. SAR interferometry with TerraSAR-X. In Proc. Of FRINGE (pp. 45-49).